UNIVERSIDADE FEDERAL DE PERNAMBUCO
DEPARTAMENTO DE FÍSICA – CCEN
PROGRAMA DE PÓS-GRADUAÇÃO EM FÍSICA

MATEUS RATTES LIMA DA MOTTA

TWO SYMMETRIC FOUR-WAVE MIXING SIGNALS INDUCED BY BEAMS WITH NONUNIFORM DISTRIBUTIONS

Recife
2021

MATEUS RATTES LIMA DA MOTTA

TWO SYMMETRIC FOUR-WAVE MIXING SIGNALS INDUCED BY BEAMS WITH NONUNIFORM DISTRIBUTIONS

Dissertação apresentada ao Programa de Pós-Graduação em Física da Universidade Federal de Pernambuco, como requisito parcial para a obtenção do título de Mestre em Física.

Área de Concentração: Óptica

Orientadora: Profa. Sandra Sampaio Vianna

Recife
2021

Catalogação na fonte
Bibliotecária Fernanda Bernardo Ferreira, CRB4-2165

M921t Motta, Mateus Rattes Lima da
Two symmetric four-wave mixing signals induced by beams with nonuniform distributions / Mateus Rattes Lima da Motta. – 2021.
83 f.: il., fig.

Orientadora: Sandra Sampaio Vianna.
Dissertação (Mestrado) – Universidade Federal de Pernambuco. CCEN, Física, Recife, 2021.
Inclui referências.

1. Óptica. 2. Mistura de quatro ondas. 3. Momento angular orbital da luz. 4. Átomos frios. I. Vianna, Sandra Sampaio (orientadora). II. Título.

535.2 CDD (23. ed.) UFPE- CCEN 2021 - 68

MATEUS RATTES LIMA DA MOTTA

TWO SYMMETRIC FOUR-WAVE MIXING SIGNALS INDUCED BY BEAMS WITH NONUNIFORM DISTRIBUTIONS

Dissertação apresentada ao Programa de Pós-Graduação em Física da Universidade Federal de Pernambuco, como requisito parcial para a obtenção do título de Mestre em Física.

Aprovada em: 23/03/2021.

BANCA EXAMINADORA

_____

Profa. Sandra Sampaio Vianna
Orientadora
Universidade Federal de Pernambuco

_____

Prof. José Wellington Rocha Tabosa
Examinador Interno
Universidade Federal de Pernambuco

_____

Prof. Antonio Zelaquett Khoury
Examinador Externo
Universidade Federal Fluminense

AGRADECIMENTOS

Agradeço aos meus pais, Maria da Conceição e Flávio Fernando, pelo carinho e suporte que sempre me deram, por tudo que me ensinaram e por sempre incentivarem o estudo e o trabalho.

À minha irmã, Melina, por compartilhar sentimentos e memórias de irmão e pelo apoio nos momentos em que mais precisei.

Aos meus avós, Irma e Mateus, por estarem sempre presentes na minha vida e por fazerem o possível para ajudar em todos os momentos.

À professora Sandra Vianna, pela dedicação e paciência que comigo teve e pelo primor com que conduziu as atividades durante o meu curso de mestrado e mesmo antes, quando fui seu aluno de iniciação científica.

Aos professores José Tabosa e Antonio Zelaquett, pelas importantes contribuições que trouxeram como membros da banca examinadora.

Aos colegas e amigos do Departamento de Física da UFPE, em especial a Alexandre, Álvaro e Leandro, pela companhia nos últimos anos e pelas boas conversas nos horários do café. A Alexandre, agradeço ainda por estar sempre disposto a ajudar com os problemas do laboratório, e com os de fora também.

Aos professores Fernando Parísio, Leonardo Cabral, Leonardo Menezes e Paulo Campos pelas disciplinas ministradas com nada menos que excelência.

A Daniel Melo, da eletrônica, e Adriel, pela dedicação nas inúmeras situações em que precisei de ajuda com componentes eletrônicos.

A todos os familiares e amigos, de perto e de longe, que me apoiaram e contribuíram das mais diversas formas para que eu pudesse concluir esta importante etapa da minha formação.

À CAPES e ao CNPq pelo suporte financeiro.

ABSTRACT

We present a theoretical analysis of the spatial shape (transverse and longitudinal) of two degenerate four-wave mixing (FWM) signals induced by fields E_a and E_b, with nonuniform transverse profiles, and wave-vectors $\vec{k}_a$ and $\vec{k}_b$. The two signals are generated in a cold sample of two-level atoms, in the forward directions $2\vec{k}_a - \vec{k}_b$ and $2\vec{k}_b - \vec{k}_a$. In all cases, the transverse shapes of the generated signals (both near- and far-field) are dictated by the projection of the nonlinear coherence onto the Laguerre-Gaussian (LG) function space. Our calculations show that the longitudinal profile of each generated beam is affected by the spectral characteristics of the medium, described by the third order nonlinear susceptibility. For Gaussian incident fields with equal detunings from resonance, the FWM beam shapes are completely symmetric, with an asymmetry induced by different detunings of incident fields. By considering incident beams with LG distributions, the topological charge conservation determines the orbital angular momentum of each signal and the longitudinal profiles show similar behaviors to the case with Gaussian beams. The phase discontinuities of LG modes reveal a rotation and distortion of the phase distribution of the FWM beams caused by the detunings. We discuss for selected configurations, the relations between both generated beams and their propagation properties. We also present preliminary experimental results of the power spectra of the two FWM signals generated in our magneto-optical trap of rubidium atoms.

Keywords: Four-wave mixing. Orbital angular momentum of light. Cold atoms. Magneto-optical trap.

RESUMO

Neste trabalho apresentamos uma análise teórica da forma espacial (transversal e longitudinal) de dois sinais de mistura de quatro ondas (MQO), degenerada, induzidos pelos campos E_a e E_b, com perfis transversais não uniformes e vetores de onda $\vec{k}_a$ e $\vec{k}_b$. Os dois sinais são gerados em uma amostra fria de átomos de dois níveis, nas direções $2\vec{k}_a - \vec{k}_b$ e $2\vec{k}_b - \vec{k}_a$. As formas transversais dos sinais gerados, tanto em campo próximo como em campo distante, são determinadas pela projeção da coerência não linear no espaço das funções Laguerre-Gauss (LG). Para o perfil longitudinal, nossos resultados mostram que os dois sinais são afetados pelas características espectrais do meio, descritas pela susceptibilidade não linear de terceira ordem. Quando os campos incidentes são Gaussianos com dessintonias iguais, as formas espaciais dos feixes de MQO são simétricas, com uma assimetria induzida por diferentes dessintonias. Para campos incidentes com distribuições LG, a conservação da carga topológica determina o momento angular orbital de cada sinal, e os perfis longitudinais apresentam comportamentos semelhantes ao caso com feixes Gaussianos. Neste caso, a dessintonia dos feixes incidentes também é responsável pelos efeitos de rotação e distorção da distribuição de fase dos sinais de MQO. Para algumas configurações, nós discutimos as relações entre os dois sinais gerados e as suas propriedades de propagação. Também apresentamos alguns resultados experimentais preliminares da forma espectral dos dois sinais de MQO obtidos em nossa armadilha magneto-ótica de rubídio.

Palavras-chave: Mistura de quatro ondas. Momento angular orbital da luz. Átomos frios. Armadilha magneto-ótica.

LIST OF FIGURES

CONTENTS

1 INTRODUCTION

The angular momentum of light can be divided into two components: a spin angular momentum, related to polarization; and an orbital angular momentum (OAM), related to the spatial distribution of the light field. Allen *et al.* [1] were the first to show that the Laguerre-Gaussian (LG) paraxial beam carries well defined OAM in the propagation direction, defined by integer ℓ, called the topological charge (TC). This seminal work was the starting point of the ever-growing field of light OAM. Today, almost three decades later, the field is an active research area in continuous growth [2].

The interaction of matter with light is accompanied by the transfer of linear and angular momentum. The transfer of linear momentum is associated with the radiation pressure onto atoms and small particles. The radiation pressure is employed in the laser cooling of atoms [3]. The transfer of spin angular momentum (SAM) from circularly polarized light was first demonstrated almost a century ago by Beth [4]. Only after 1992 the transfer of OAM from LG beams to small particles was demonstrated [5, 6]. In both of these works the particles were trapped at the dark focus of an LG beam by the dipole force and set into rotating motion due to the beam's helical phase structure. The quantized nature of the OAM of light has been explored [7] and the transfer of OAM in units of $\ell\hbar$ to atoms was demonstrated in a sodium Bose-Einstein condensate [8].

Also, after the first proposals, new possibilities were opened in communications technology, due to the capability of information multiplexing with an additional degree of freedom of light and the infinite dimensionality of the OAM space [9].

Four-wave mixing (FWM) processes can take place in a variety of systems, such as atomic vapors, cold atom samples, optical fibers, and others. A number of optical phenomena related to FWM has been extensively investigated over the years. Denegerate four-wave mixing (DFWM) in a two-level atomic system and related effects, for instance, the AC Stark shift, phase conjugation and others, have been well known for a long time [10, 11, 12, 13]. Three-level atomic systems have been used to demonstrate effects such as electromagnetically induced transparency (EIT), where the presence of a strong resonant field drives the medium transparent near an optical transition, thus enhancing the nonlinear signal generation [14, 15].

In the nonlinear regime, light beams carrying OAM have been first applied to investigate second harmonic generation (SHG) in crystals [16, 17], where the beam at the fundamental frequency ω carries TC ℓ and, due to the conservation of OAM, the frequency doubled beam emerges with 2ℓ. This is one key idea when employing OAM beams in nonlinear optics: the transfer of topological charge and transverse structure from incident to generated fields. Today, SHG still offers an interesting platform for processes involving the transverse degrees of freedom of light.

FWM processes involving laser beams with OAM have also been widely explored. One commonly used setting is FWM induced by amplified spontaneous emission in a hot atomic vapour, with a 3-level cascade system. In this process, two input photons at 780 nm and 776 nm interact to generate blue light at 420 nm with an emission also at 5.23 μm. The transfer of OAM and complex profiles from inputs to blue light in this system were demonstrated [18, 19]. It has also been used to distinguish nonlinear processes [20], to investigate the spiral bandwidth of the generated signals [21] and the

Gouy phase-matching condition [22].

FWM involving OAM beams was also performed in cold atoms to transfer OAM from incident to generated beams in nondegenerate [23] and degenerate [24] atomic systems, to transfer more complicated phase structures (obtained by superimposing LG modes of different orders) [25] and to store the OAM of light in the ensemble of atoms [26].

When the primary concern is the spatial shape of the FWM beam, the usual approach is based on the overlap integral of four LG modes only. The medium simply allows the nonlinear process to take place, and medium quantities don't affect the output mode superposition. With this approach, the theoretical predictions are remarkably accurate [18, 22, 27]. The role of the spatially dependent nonlinear coherence in the signal generation process is discussed in [28]. In [29], the full spatial dependence of medium quantities is taken into account in calculations and effects of detunings from resonance and phase mismatch on the phase distribution of the FWM beam are evidenced. No connection is established, however, with spatial properties of the beam outside the interaction medium.

This work is mainly a theoretical study of the spatial shape of two symmetric signals of degenerate four-wave mixing in a sample of cold two-level atoms. We focus on the influence of the spatially dependent nonlinear susceptibility, induced as a result of the nonlinear process, on the overall shape of the two FWM signals. We investigate the spatial properties of the generated beams in various configurations. Our calculations present effects already reported, such as the bending of phase discontinuities of the generated FWM beam [29, 30]. We also show that the so called root mean square parameters of the generated beam, that serve as an effective measure of the longitudinal profile, are also affected in an intuitive manner by the frequency degrees of freedom.

Most of our results focus on the thin-medium regime, characterized by $L/z_R \ll 1$, where L is the interaction medium extension and z_R is the Rayleigh range of the beams involved in the process. This regime is in agreement with the experimental conditions in our magneto-optical trap. In the thick-medium regime, where the relation $L/z_R \gg 1$ holds, we discuss possible outcomes due to the requirement of the Gouy phase-matching condition [22] in the configuration where two FWM signals are generated. This regime is more easily achievable in a hot atomic vapor cell, for example. We also describe our experimental apparatus and present preliminary experimental results, namely the FWM spectrum in two configurations of relative polarizations of incident beams, and the intensity profile of the FWM signal induced by Gaussian beams.

The dissertation is divided as follows. In Chapter 2 we discuss fundamental concepts related to the topics of this work. In Chapter 3 we describe the various components of the experimental setup and their operation. Chapter 4 contains the theoretical model developed to describe the generation of the FWM signal and its properties. The model is divided in two main parts: (1) the calculation of the density operator's matrix elements and (2) the solution to the wave equation for the electric field of the FWM beam. With the solution to the FWM field, we calculate and analyze its properties. In Chapter 5, we present and discuss our main results. Concluding remarks are given in Chapter 6.

2 FUNDAMENTALS

In this Chapter, we describe fundamental concepts related to the various topics in this dissertation. Sections 1-5 focus, respectively, on the interaction of two-level atoms with radiation, the structure of rubidium atoms, the magneto-optical trap, orbital angular momentum of light in the paraxial regime and nonlinear optics.

2.1 Interaction of two-level atoms with light

To describe the atomic response due to the interaction with the oscillating electric field of laser light (the response due to the magnetic component of the radiation field is negligible in comparison) we employ the density matrix formalism. In many situations, including the ones we are interested in, the interaction involves only two atomic states. Thus, the atom can be modeled as a two-level system, where the the two states are the ground and excited states, $|1\rangle$ and $|2\rangle$, respectively. This problem is treated in many standard textbooks. We follow more closely the procedure developed in Chapter 8 of Ref. [31]. The Hamiltonian of the system is

$$\hat{H} = \hat{H}_o + \hat{H}_{\rm int}, \tag{2.1}$$

where $\hat{H}_o = \mathbb{E}_1 |1\rangle \langle 1| + \mathbb{E}_2 |2\rangle \langle 2|$ is the non-perturbed Hamiltonian for the internal degrees of freedom of the atom and $\mathbb{E}_j$ is the energy eigenvalue of state $|j\rangle$. The interaction Hamiltonian $\hat{H}_{\rm int}$ is the electric dipole Hamiltonian,

$$\hat{H}_{\rm int}(\vec{r}, t) = -\boldsymbol{\mu} \cdot \vec{E}(\vec{r}, t), \tag{2.2}$$

where $\boldsymbol{\mu} = e\mathbf{r}$ is the electric dipole operator. The electric field $\vec{E}(\vec{r}, t)$ of the monochromatic light beam, with frequency ω and wave-vector $\vec{k}$, is given by

$$\begin{aligned} \vec{E}(\vec{r}, t) &= \hat{\varepsilon}\mathcal{E}(\vec{r}) e^{-i(\vec{k}\cdot\vec{r} - \omega t)} + c.c., \\ &= \hat{\varepsilon} E(\vec{r}, t) + c.c., \end{aligned} \tag{2.3}$$

where $\hat{\varepsilon}$ is the polarization direction and $\mathcal{E}(\vec{r})$ is the slowly varying spatial envelope, that carries the transverse dependence of the field. In the rotating wave and electric dipole approximations, the matrix elements of the interaction Hamiltonian are written as

$$\begin{aligned} H_{{\rm int},jk} &= \langle j | \hat{H}_{\rm int} | k \rangle \\ &= -\mu_{jk} \mathcal{E}(\vec{r}) e^{-i(\vec{k}\cdot\vec{r} - \omega t)}. \end{aligned} \tag{2.4}$$

where $(j, k) \in \{1, 2\}$ and $\mu_{jk} = \langle j | \boldsymbol{\mu} \cdot \hat{\varepsilon} | k \rangle$, is the transition dipole moment. The phases of $|1\rangle$ and $|2\rangle$ can be chosen so that μ_{12} is a real number. We introduce the Rabi frequency

$$\Omega_{jk}(\vec{r}) = \frac{\mu_{jk} \mathcal{E}(\vec{r})}{\hbar}, \tag{2.5}$$

to write

$$H_{{\rm int},jk} = -\hbar \Omega_{jk} e^{-i(\vec{k}\cdot\vec{r} - \omega t)}. \tag{2.6}$$

In matrix form, $\hat{H}$ is

$$\hat{H} = \begin{pmatrix} \mathbb{E}_1 & H_{\text{int},12} \\ H_{\text{int},21} & \mathbb{E}_2 \end{pmatrix}. \tag{2.7}$$

The density operator is used to describe a statistical mixing of quantum states and is ideal to model an ensemble of atoms, due to our lack of knowledge concerning the exact state of the system. It is given by

$$\hat{\rho} = \sum_{jk} \rho_{jk} \left|j\right\rangle \left\langle k\right|. \tag{2.8}$$

The diagonal elements ρ_{jj} are called populations and represent the probability of finding an atom of the ensemble in state $|j\rangle$. The off-diagonal elements ρ_{jk} are the coherences and are related to the response of the medium due to the interaction with light, given by the macroscopic polarization $\vec{P}$. The time evolution of $\hat{\rho}$ is determined by Liouville's Equation,

$$\frac{d\hat{\rho}}{dt} = \frac{i}{\hbar}[\hat{\rho}, \hat{H}], \tag{2.9}$$

where $[\hat{A}, \hat{B}]$ denotes the commutator of operators $\hat{A}$ and $\hat{B}$. Using the matrices representing $\hat{H}$ and $\hat{\rho}$, we can write the equations describing the time evolution of each element of $\hat{\rho}$

$$\dot{\rho}_{11} = \frac{i}{\hbar}\left[\rho_{12}H_{\text{int},21} - \rho_{21}H_{\text{int},12}\right], \tag{2.10}$$

$$\dot{\rho}_{22} = \frac{i}{\hbar}\left[\rho_{21}H_{\text{int},12} - \rho_{12}H_{\text{int},21}\right], \tag{2.11}$$

$$\dot{\rho}_{12} = \frac{i}{\hbar}\left[H_{\text{int},12}\left(\rho_{11} - \rho_{22}\right) + \rho_{12}\left(\mathbb{E}_2 - \mathbb{E}_1\right)\right], \tag{2.12}$$

$$\dot{\rho}_{21} = \frac{i}{\hbar}\left[H_{\text{int},21}\left(\rho_{22} - \rho_{11}\right) + \rho_{21}\left(\mathbb{E}_1 - \mathbb{E}_2\right)\right]. \tag{2.13}$$

We rewrite the above system of coupled equations in the more convenient form

$$(\dot{\rho}_{22} - \dot{\rho}_{11}) = -\frac{2i}{\hbar}[\rho_{12}H_{\text{int},21} - c.c.], \tag{2.14}$$

$$\dot{\rho}_{12} = -\frac{i}{\hbar}\left[H_{\text{int},12}(\rho_{22} - \rho_{11}) - \rho_{12}\left(\mathbb{E}_2 - \mathbb{E}_1\right)\right], \tag{2.15}$$

where $\rho_{11}+\rho_{22} = 1$ and $\rho_{12} = \rho_{21}^*$ must be satisfied. Now we introduce the relaxation terms corresponding to spontaneous decay. In our model, populations and coherences decay at rates Γ and $\Gamma/2$, respectively, where $\Gamma/2\pi$ is the natural decay rate of the excited state. For the D_2 line of ^{87}Rb, we have $\Gamma/2\pi = 6$ MHz [32]. We get

$$\begin{aligned} (\dot{\Delta\rho}) &= -\frac{2i}{\hbar}[\rho_{12}H_{\text{int},21} - c.c.] - \Gamma\left[\Delta\rho - (\Delta\rho)^0\right], \\ \dot{\rho}_{12} &= -\frac{i}{\hbar}\left[H_{\text{int},12}\Delta\rho - \rho_{12}\left(\mathbb{E}_2 - \mathbb{E}_1\right)\right] - \frac{\Gamma}{2}\rho_{12}, \end{aligned} \tag{2.16}$$

where $\Delta\rho = (\rho_{22} - \rho_{11})$ and $(\Delta\rho)^0 = -1$ is the population difference far from the region of interaction. These are the Optical Bloch's Equations (OBEs) for our system. We write the coherence in the slowly varying form

$$\rho_{12} = \sigma_{21}e^{i\omega t}, \tag{2.17}$$

and substitute $H_{\text{int},12}$ from (2.4) to arrive at

$$(\dot{\Delta\rho}) = 2i(\sigma_{12}\Omega_{12}^* - \sigma_{21}\Omega_{12}) - \Gamma\left[\Delta\rho - (\Delta\rho)^0\right], \tag{2.18}$$

$$\dot{\sigma}_{12} = i\Omega_{12}\Delta\rho - \sigma_{12}\left(i\delta + \frac{\Gamma}{2}\right), \tag{2.19}$$

where $\delta = \omega - \omega_o$ is the detuning from resonance and $\omega_o = (\mathbb{E}_2 - \mathbb{E}_1)/\hbar$ is the resonance frequency. In the steady state,

$$\Delta\rho = (\Delta\rho)^0 + \frac{2i}{\Gamma}[\sigma_{12}\Omega_{12}^* - \sigma_{21}\Omega_{12}], \tag{2.20}$$

$$\sigma_{12} = i\frac{\Omega_{12}\Delta\rho}{i\delta + \Gamma/2}. \tag{2.21}$$

Substituting the second equation into the first, we get

$$\Delta\rho = \frac{(\Delta\rho)^0}{1 + \dfrac{2|\Omega_{12}|^2}{\delta^2 + \Gamma^2/4}}. \tag{2.22}$$

The steady state solution to σ_{12} is thus

$$\sigma_{12} = -\frac{\Omega_{12}\,(\delta + i\Gamma/2)}{\delta^2 + \Gamma^2/4 + 2|\Omega_{12}|^2}. \tag{2.23}$$

The presence of $|\Omega_{12}|^2$ in the denominator is related to saturation effects and power broadening. The response of the system is governed by the macroscopic polarization, given by

$$\begin{aligned} \vec{P} &= \mathcal{N}\langle\boldsymbol{\mu}\rangle, \\ &= \mathcal{N}\mathrm{Tr}[\hat{\rho}\boldsymbol{\mu}], \end{aligned} \tag{2.24}$$

where $\mathcal{N}$ is the atomic density. It is also related to the incident field by the electric susceptibility χ via

$$\vec{P} = \varepsilon_o\chi\hat{\varepsilon}E + c.c. \tag{2.25}$$

Projecting equations (2.24) and (2.25) onto $\hat{\varepsilon}^*$,

$$\varepsilon_o\chi E = \mathcal{N}\mathrm{Tr}[\hat{\rho}(\boldsymbol{\mu}\cdot\hat{\varepsilon}^*)]. \tag{2.26}$$

The trace is the dipole moment per atom and can be readily found as $\mathrm{Tr}[\hat{\rho}(\boldsymbol{\mu}\cdot\hat{\varepsilon}^*)] = (\mu_{21}\sigma_{12}e^{i\omega t} + c.c.)$. Substituting (2.23), we find

$$\chi = -\frac{\mathcal{N}|\mu_{12}|^2}{\hbar\varepsilon_o}\frac{\delta + i\Gamma/2}{\delta^2 + \Gamma^2/4 + 2|\Omega_{12}|^2}. \tag{2.27}$$

The complex index of refraction in the medium is $\tilde{n} = (1+\chi)^{1/2}$, which for $\chi \ll 1$,

$$\tilde{n} \simeq 1 + \frac{\chi}{2}. \tag{2.28}$$

We define

$$\tilde{n} \equiv n + i\frac{c}{2\omega}\alpha, \tag{2.29}$$

where n is the index of refraction in the medium and α is the absorption coefficient. Comparing (2.28) and (2.29), we find

$$n = 1 - \frac{\mathcal{N}|\mu_{12}|^2}{2\hbar\varepsilon_o}\frac{\delta}{\delta^2 + \Gamma^2/4 + 2|\Omega_{12}|^2}, \tag{2.30}$$

$$\alpha = -\frac{\Gamma k\mathcal{N}|\mu_{12}|^2}{2\hbar\varepsilon_o}\frac{1}{\delta^2 + \Gamma^2/4 + 2|\Omega_{12}|^2}. \tag{2.31}$$

The intensity of the incident wave propagating inside the medium decays with $e^{-|\alpha|z}$. Figure 1 shows n and α as functions of the detuning from resonance δ.

Figure 1 – Dependence of (a) the index of refraction n and (b) the absorption coefficient α with the detuning from resonance for different field amplitudes $\Omega_{12} = \Omega$. $\Gamma/2\pi = 6$ MHz, corresponding to the D_2 line of ^{87}Rb.

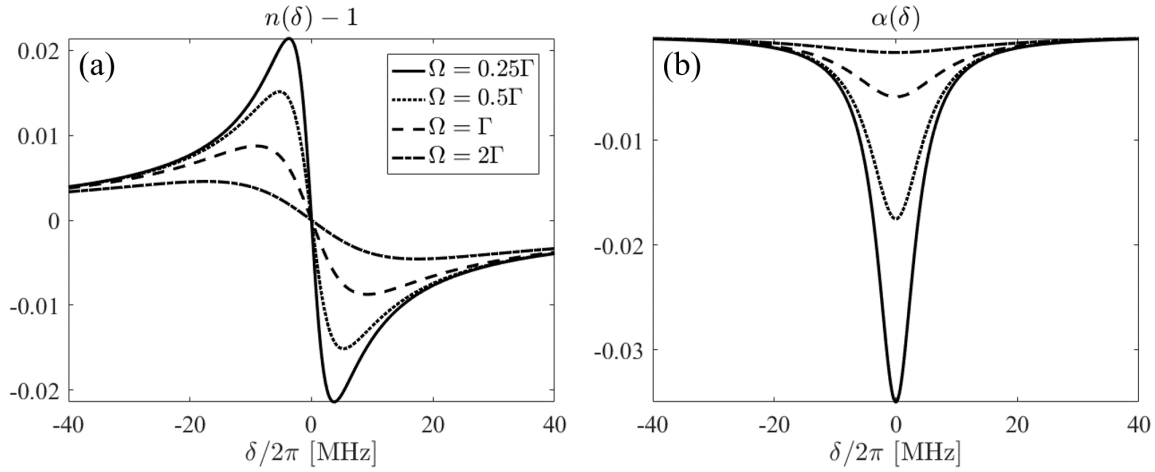

Source: The author (2021).

Due to the Doppler effect and the atomic motion at room temperature, atoms see an incoming light field given by (2.3) with frequency $\omega' = \omega - \vec{k}\cdot\vec{v}$. Considering the movement in 1D, the response of a large number of atoms in the velocity group v is $\chi(\delta - kv)$. To account for all velocity groups, we average the susceptibility over all possible values of v,

$$\langle\chi(\delta)\rangle_D = \int_{-\infty}^{\infty}\chi(\delta - kv)f(v)dv. \tag{2.32}$$

The weighting factor $f(v)$ is the Maxwell-Boltzmann distribution,

$$f(v) = \frac{1}{\sqrt{\pi}u}e^{-v^2/u^2}, \tag{2.33}$$

where $u = \sqrt{2k_bT/m}$ is the most probable velocity at a given temperature T. The absorption coefficient becomes

$$\langle\alpha(\delta)\rangle_D = -\frac{\Gamma k\mathcal{N}|\mu_{12}|^2}{2\hbar\varepsilon_o}g_{\mathrm{V}}(\delta), \tag{2.34}$$

where $g_{\mathrm{V}}(\delta)$ is the lineshape function, with a Voigt profile, which is the convolution between the Lorentzian and Gaussian lineshapes,

$$g_{\mathrm{V}}(\delta) = \frac{1}{\sqrt{\pi}u}\int_{-\infty}^{\infty}\frac{e^{-v^2/u^2}}{(\delta - kv)^2 + \Gamma^2/4 + 2|\Omega_{12}|^2}dv. \tag{2.35}$$

Figure 2 shows a Lorentzian lineshape and the Voigt profile considering an atomic sample at $T \approx 200$ mK. We see that the motion of atoms at this relatively low temperature leads

Figure 2 – Lorentzian profile for $\Omega_{12} = \Gamma/2$ and Voigt profile for the same amplitude considering a sample of atoms at $T \approx 200$ mK ($u \approx 6$ m/s).

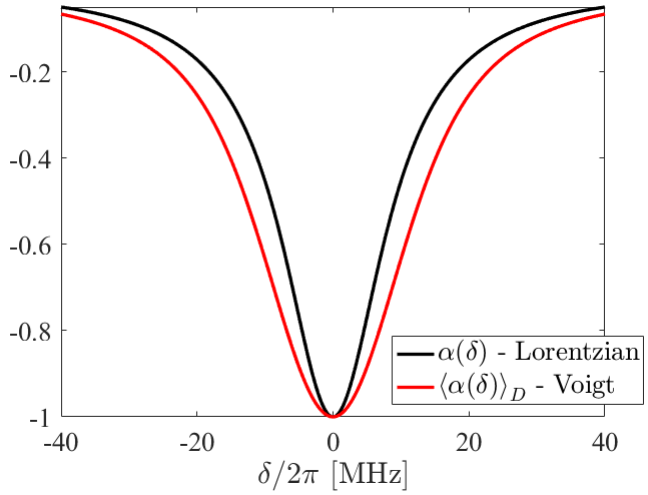

Source: The author (2021).

to a significant broadening of the absorption lines. At room temperature, $T \approx 300$ K, the Doppler broadening is much greater than many natural linewidths.

2.2 Hyperfine structure of rubidium

Alkali atoms possess a single valence electron orbiting a core composed of the nucleus (total charge $+Ze$) and the electrons of the closed subshells (total charge $-[Z-1]e$), which shield the nuclear charge. Due to the shielding effect, an excited outermost electron experiences the potential of a nuclear charge of $+e$. In this case, its energy is essentially hydrogenic, $\mathbb{E}_n^{\text{alkali}} \simeq \mathbb{E}_1^{\text{H}}/n^2$, where $\mathbb{E}_1^{\text{H}}$ is the ground state energy of hydrogen and n is the principal quantum number. For an s valence electron, however, the shielding is not as effective, and it sees a greater nuclear charge. Because of this, s electrons have lower energies than d electrons with the same principal quantum number. The quantum defect δ_L is a quantity subtracted from the principal quantum number n of the alkalis to account for this effect. The subscript L indicates the dependence of the quantum deffect on the orbital angular momentum quantum number. The effective principal quantum number is $n^* = n - \delta_L$, and the energies of alkali atoms are well described by the modified form of Bohr's formula $\mathbb{E}_{n^*}^{\text{alkali}} = \mathbb{E}_1^{\text{H}}/(n^*)^2$.

The fine structure of atoms is a result of the spin-orbit coupling. The total angular momentum of the outer electron is given by $\mathbf{J} = \mathbf{L} + \mathbf{S}$, where $\mathbf{L}$ and $\mathbf{S}$ are the orbital and spin angular momentum operators, respectively. From the quantum mechanical theory of addition of angular momenta, the corresponding quantum number J is such that $|L-S| \leq J \leq L+S$. Further, the associated magnetic quantum number m_J assumes all integer or half-integer values in the range $-J \leq m_J \leq J$. The hyperfine structure is a result of the coupling between $\mathbf{J}$ and the nuclear angular momentum $\mathbf{I}$. The total atomic angular

momentum is given by $\mathbf{F} = \mathbf{J} + \mathbf{I}$ and likewise, the quantum numbers F and m_F must satisfy $|J - I| \leq F \leq J + I$ and $-F \leq m_F \leq F$, respectively. The total energy shift due to these effects can be written as

$$\begin{aligned} \Delta E &= \Delta E_{\mathrm{SO}} + \Delta E_{\mathrm{HFS}}, \\ &= A_{\mathrm{SO}} \langle \mathbf{L} \cdot \mathbf{S} \rangle + B_{\mathrm{HFS}} \langle \mathbf{J} \cdot \mathbf{I} \rangle . \end{aligned} \tag{2.36}$$

The expectation values are

$$\begin{aligned} \langle \mathbf{L} \cdot \mathbf{S} \rangle &= \frac{\hbar^2}{2} \left[J(J+1) - L(L+1) - S(S+1) \right], \\ \langle \mathbf{J} \cdot \mathbf{I} \rangle &= \frac{\hbar^2}{2} \left[F(F+1) - J(J+1) - I(I+1) \right], \end{aligned} \tag{2.37}$$

and the coupling factors A_{SO} and B_{HFS} can be calculated following standard atomic physics text books [33, 34]. The energy shift due to the spin orbit interaction is of the order $\alpha^2 \mathbb{E}_{n^*}$, where $\alpha = e^2/4\pi\varepsilon_0\hbar c \simeq 1/137$ is the fine structure constant. The second term on the right-hand side of (2.36) leads to smaller corrections because the magnetic moment of the nucleus is much smaller than the magnetic moment of the electron [34].

Rubidium has two stable isotopes, ^{85}Rb and ^{87}Rb, that are found with abundances of 72.2% and 27.8%, respectively. For its ground state, $n = 5$, $L = 0$, $S = 1/2$ and $J = 1/2$. In the first excited, $L = 1$, $S = 1/2$ and J can assume the values $J = 1/2, 3/2$. The spin-orbit interaction thus splits the energy levels of p electrons into two. The transitions $|L = 0, J = 1/2\rangle \rightarrow |L = 1, J = 1/2\rangle$ and $|L = 0, J = 1/2\rangle \rightarrow |L = 1, J = 3/2\rangle$ are referred to as the D_1 and D_2 lines, respectively. The D_2 lines of both isotopes contain cycling transitions that are of uttermost importance to the trapping and cooling of these atoms. In this work we use the D_2 line of ^{87}Rb. The nuclear spin of ^{87}Rb is $I = 3/2$. The ground state ($J = 1/2$, $I = 3/2$) is split into two, $F = 1, 2$, while the first excited state ($J = 3/2$, $I = 3/2$) is split into four hyperfine levels, $F = 0, 1, 2, 3$. The cyclic transition of the D_2 line is $|J = 1/2, F = 2\rangle \rightarrow |J = 3/2, F = 3\rangle$. Figure 3 shows the hyperfine energy levels of the D_2 line of ^{87}Rb.

Figure 3 – Hyperfine energy levels of the D_2 line of ^{87}Rb.

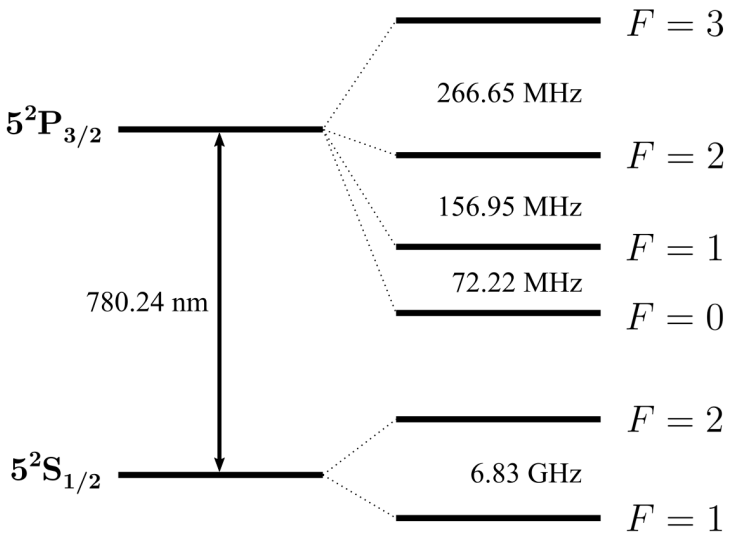

Source: Modified from [32].

2.2.1 Saturated absorption

The motion of atoms at room temperature leads to a significant broadening of the absorption lines due to the Doppler effect. For this reason, the hyperfine transitions of Rb cannot be resolved by ordinary absorption. In order to eliminate the Doppler broadening and reveal the hyperfine structure, one must perform a saturated absorption (SA) experiment. The setup is as follows. Two counter-propagating beams, a strong pump and a weak probe, that originate from a single laser (and thus have the same frequency at all times) are superimposed in a region where the atoms are located. The frequency is made to vary around a hyperfine transition. Off resonance, pump and probe interact with different velocity groups and both beams are absorbed. Precisely at resonance, both beams interact with atoms in the velocity group $v = 0$. The intense pump saturates the medium and thus the probe beam cannot be absorbed, leading to a peak on the probe transmission at resonance. Figure 4 illustrates the process.

Figure 4 – Depiction of the saturated absorption process. (a) Off resonance, pump and probe interact with atoms at different velocity groups. Exactly at resonance, both beams interact with the velocity group $v = 0$ and the probe is not absorbed. This leads to a peak at a hyperfine resonance frequency in the probe transmission (b).

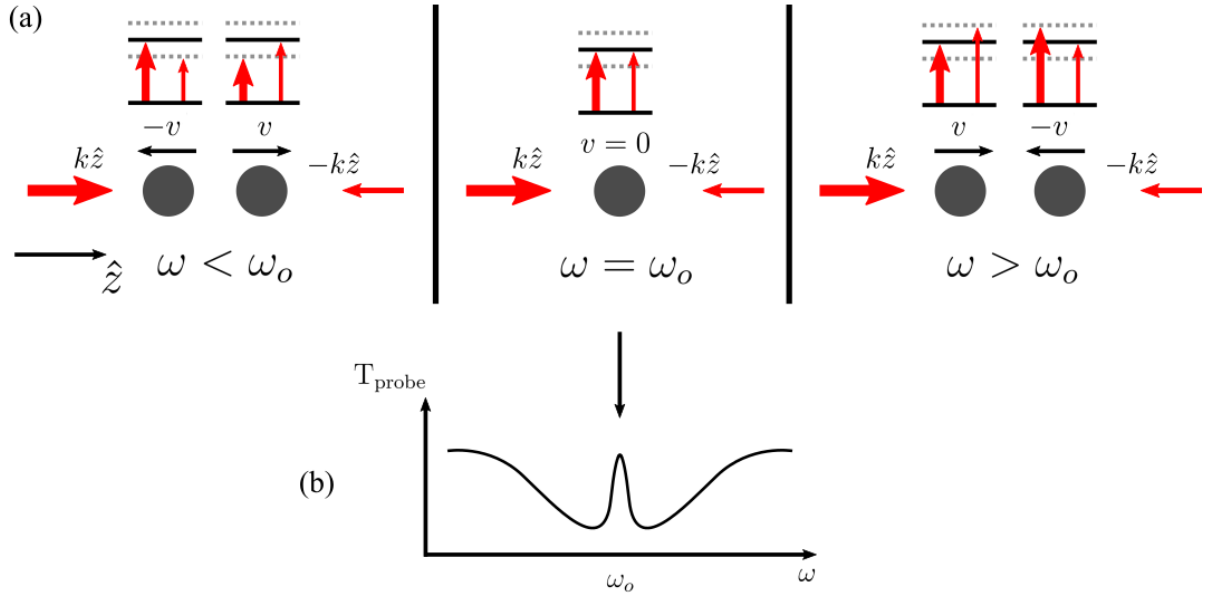

Source: The author (2021).

When we have two hyperfine transitions with common ground states, an additional peak will appear halfway between the two expected peaks in the SA spectrum. These are called cross-over resonances, and arise because when the frequency of the beams is $\omega = \overline{\omega} = (\omega_1 + \omega_2)/2$, where $\omega_1 < \omega_2$ are the frequencies corresponding to the two transitions, pump and probe interact with the same velocity groups $\pm v' = \pm(\omega_2 - \omega_1)/2k$, where k is the wave-number. In the reference frame considered (figure 5b), atoms with positive (negative) velocity will be promoted to states $|1\rangle$ ($|2\rangle$) by the pump, saturating these atoms. At the same time the probe would also interact with these velocity groups, but atoms with positive (negative) velocity would be promoted to $|2\rangle$ ($|1\rangle$) if the medium were not saturated by the pump. This leads to a peak on the probe transmission at $\overline{\omega}$. Figure 5 illustrates the process.

Figure 5 – Cross-over (CO) resonances in the saturated absorption spectrum. (a) Energy levels involved in the process and associated transition frequencies. (b) Exactly when $\omega = \overline{\omega}$ the pump saturates the atoms in the velocity groups $\pm v'$. As a consequence, the probe cannot interact with these atoms and is transmitted through the medium. This leads to a peak halfway between the two expected resonances at ω_1 and ω_2 in the probe transmission (c).

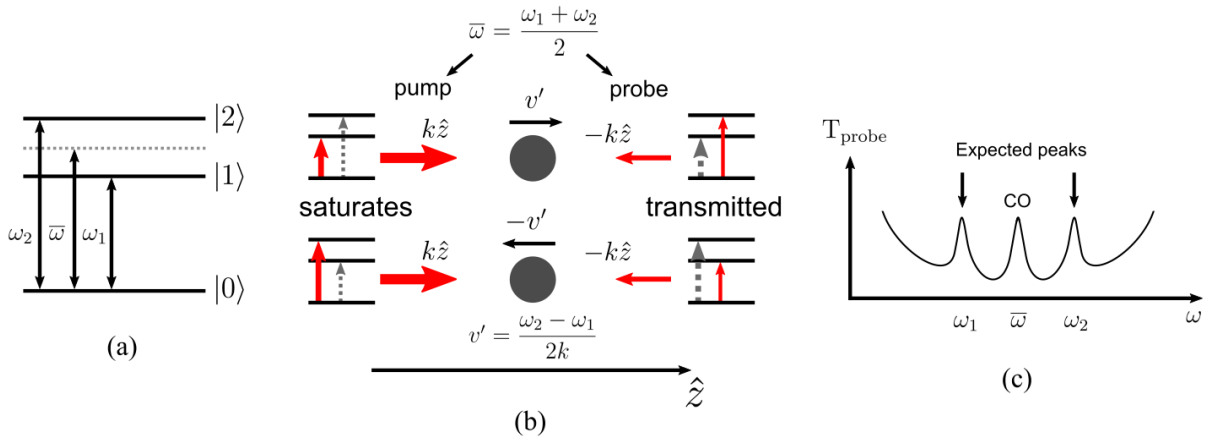

Source: The author (2021).

A saturated absorption spectrum can be used as a reference signal to lock the frequency of a tunable diode laser at desired hyperfine transitions using a control system. This experiment can be implemented using only a fraction of the total output power of conventional diode lasers and a few optical components. Figure 6 shows the saturated absorption spectrum of Rb. In the close up, showing the transitions from $F_g = 2$ of ^{87}Rb, we see three well defined peaks, corresponding to $F_g = 2 \rightarrow F_e = 3$, centered at zero, and two cross-over resonances. There are three other peaks that cannot be seen, corresponding to $F_g = 2 \rightarrow F_e = 1, 2$ and a third cross-over.

Figure 6 – Saturated absorption spectrum of Rb. The peak at $\delta = 0$ represents the $F_g = 2 \rightarrow F_e = 3$ hyperfine transition. Inset shows region inside dashed box. CO(X&Y) denotes the cross-over transition involving excited states with $F =$ X and Y of ^{87}Rb.

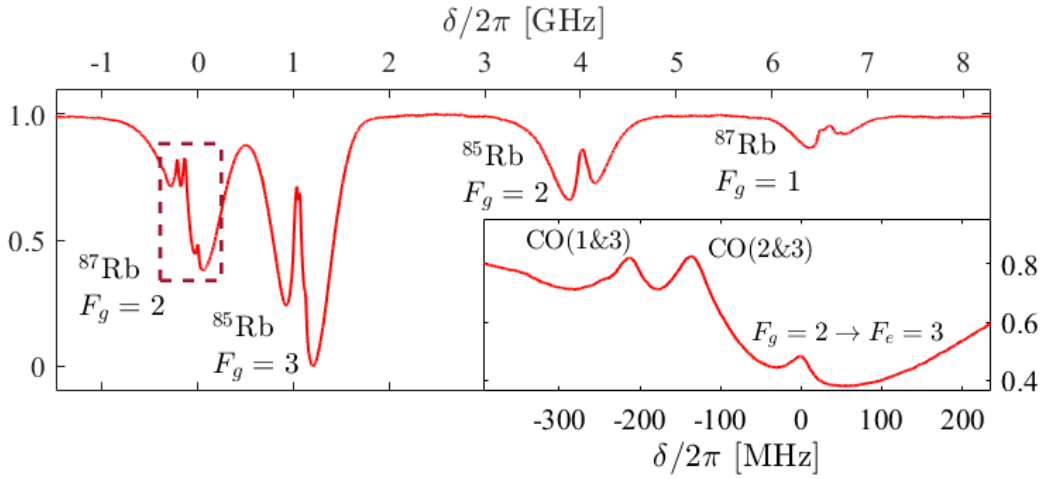

Source: The author (2021).

2.3 Magneto-optical trap

The magneto-optical trap (MOT) is an apparatus used to cool and trap neutral atoms. The temperatures of the cold samples are of the order of hundreds of μK. The MOT is the result of a series of advances in experimental techniques that culminated in the 1997 Nobel Prize in Physics. Without much detail, the working of the MOT depends on two phenomena: radiation pressure and the Zeeman shift. It consists of 3 pairs of counter-propagating lasers beams tuned below the resonance with a cyclic transition, with each beam in a pair possessing opposite circular polarizations $\hat{\sigma}^{\pm}$; and a quadrupole magnetic field that leads to a position dependent Zeeman shift of the atomic energy levels. More detailed descriptions of the fundamentals of a MOT and its historical development can be found in references [33, 35].

2.3.1 Radiation force on atoms

To describe the forces on atoms due to the interaction with light, we use the two-level atom model. From the Ehrenfest Theorem, the force on an atom is

$$\begin{aligned} \vec{\mathcal{F}} &= \frac{d}{dt}\langle \mathbf{p} \rangle , \\ &= \frac{i}{\hbar}\left\langle [\hat{H}, \mathbf{p}] \right\rangle , \\ &= -\left\langle \nabla \hat{H}_{\text{int}} \right\rangle , \end{aligned} \tag{2.38}$$

where $\mathbf{p}$ is the momentum operator. The Hamiltonian is written in the form already used in this text, $\hat{H} = \hat{H}_o + \hat{H}_{\text{int}}$, where $\hat{H}_o$ is the Hamiltonian of the free atom and $\hat{H}_{\text{int}} = -\boldsymbol{\mu} \cdot \vec{E}(\vec{r}, t)$ is the electric dipole interaction Hamiltonian. The electric field is written as in equation (2.3) and we consider that its spatial variation is negligible near the center of mass of the atom $\vec{r} = \vec{r}_c$, thus

$$\vec{\mathcal{F}} = -\langle \boldsymbol{\mu} \cdot \hat{\varepsilon} \rangle \nabla E(\vec{r}, t)|_{\vec{r}_c}. \tag{2.39}$$

Now we use $\langle \boldsymbol{\mu} \cdot \hat{\varepsilon} \rangle = \text{Tr}\left[\hat{\rho}(\boldsymbol{\mu} \cdot \hat{\varepsilon})\right]$ to get

$$\vec{\mathcal{F}} = -(\mu_{21}\sigma_{12}e^{i\omega t} + c.c.)\left[\nabla \mathcal{E}(\vec{r})|_{\vec{r}_c} e^{-i(\vec{k}\cdot\vec{r}_c - \omega t)} - i\vec{k}\mathcal{E}(\vec{r}_c)e^{-i(\vec{k}\cdot\vec{r}_c - \omega t)} + c.c.\right]. \tag{2.40}$$

In the rotating wave approximation, the terms with frequency 2ω average to zero. Also, considering that the sample of atoms is located in a region where the phase of $\mathcal{E}(\vec{r})$ is negligible, we get

$$\vec{\mathcal{F}} = \frac{-\hbar\Omega(\vec{r}_c)}{\delta^2 + \Gamma^2/4 + 2|\Omega(\vec{r}_c)|^2}\left[2\delta\nabla\Omega(\vec{r})|_{\vec{r}_c} - \Gamma\vec{k}\Omega(\vec{r}_c)\right], \tag{2.41}$$

where Ω is the Rabi frequency. We see that $\vec{\mathcal{F}}$ is composed by two types of forces, a dissipative force $\vec{\mathcal{F}}_{\text{diss}}$ and a conservative force $\vec{\mathcal{F}}_{\text{cons}}$, given by

$$\vec{\mathcal{F}}_{\text{diss}} = \frac{\hbar\vec{k}|\Omega|^2\Gamma}{\delta^2 + \Gamma^2/4 + 2|\Omega|^2}, \tag{2.42}$$

$$\vec{\mathcal{F}}_{\text{cons}} = \frac{-2\delta\Omega\nabla\Omega}{\delta^2 + \Gamma^2/4 + 2|\Omega|^2}, \tag{2.43}$$

where it is implicit that the fields are evaluated near $\vec{r}_c$. The conservative force arises due to the spatial distribution of the electric field of light. This term describes the forces in optical tweezers [36] and bottle beams [37], for example. In the simpler case of laser beams given by plane wave fields, $\vec{\mathcal{F}}_{\text{cons}} \approx 0$, and we shall disregard this term for the rest of the section. Using $\rho_{22} = (1 + \Delta\rho)/2$, the relevant force term can be written as

$$\vec{\mathcal{F}}_{\text{diss}} = \Gamma\rho_{22}\hbar\vec{k}, \tag{2.44}$$

and this expression gives a straightforward meaning to this component: it is equal to the scattering rate, $\Gamma\rho_{22}$, multiplied by the momentum of each photon [33]. The scattering rate is the rate at which a photon is absorbed and then re-emitted in a random direction. The kick given by the photon in the spontaneous emission process averages to zero over many cycles.

2.3.2 Optical molasses

When two counter-propagating laser beams interact with a moving atom, the Doppler effect leads to an imbalance between the forces exerted by each beam. The net radiation force is shown to be a damping force. If three pairs of counter-propagating beams are made to intersect, atoms located near the intersection region experience a viscous force in all directions. This is called the optical molasses (OM) technique [3], named in analogy with the movement of a particle in a viscous fluid, and used to cool atoms with laser light. It is also the first step needed to attain a magneto-optical trap. Using (2.44), we write the total force exerted on an atom with velocity vector $\vec{v} = v_x\hat{x} + v_y\hat{y} + v_z\hat{z}$ located in an OM generated using laser beams with wave-number k

$$\vec{\mathcal{F}}_{\text{OM}} = \Gamma\hbar k \sum_i \hat{x}_i \left[\rho_{22}(\delta - kv_i) - \rho_{22}(\delta + kv_i)\right], \tag{2.45}$$

where $i = 1, 2, 3$, referring to the x, y and z directions, respectively. For $|kv_i| \ll \Gamma$ in all directions, we expand

$$\vec{\mathcal{F}}_{\text{OM}} \simeq \Gamma\hbar k \sum_i \hat{x}_i(kv_i) \left[\left.\frac{\partial\rho_{22}(\delta - kv_i)}{\partial(kv_i)}\right|_{kv_i=0} - \left.\frac{\partial\rho_{22}(\delta + kv_i)}{\partial(kv_i)}\right|_{kv_i=0}\right], \tag{2.46}$$

where the derivatives can be found as

$$\left.\frac{\partial\rho_{22}(\delta \pm kv_i)}{\partial(kv_i)}\right|_{kv_i=0} = \frac{\mp 2\delta|\Omega|^2}{(\delta^2 + \Gamma^2/4 + 2|\Omega|^2)^2}. \tag{2.47}$$

The force is thus written as

$$\vec{\mathcal{F}}_{\text{OM}} = -\gamma\vec{v}, \tag{2.48}$$

where

$$\gamma = \frac{-4\Gamma\hbar k^2\delta|\Omega|^2}{(\delta^2 + \Gamma^2/4 + 2|\Omega|^2)^2}. \tag{2.49}$$

Evidently, fluctuations and asymmetries may lead to different damping coefficients in different directions. It is seen that $\delta < 0$ is a necessary condition to obtain a damping force.

2.3.3 Magnetic trapping force

Atoms located near the intersection of the three pairs of beams are cooled, but can diffuse away from this region. To trap these atoms, a restoring force is necessary, just like a classical harmonic oscillator. In order to generate this force, a quadrupole magnetic field is introduced at the OM region [38]. This field is attained with a pair of circular coils with currents of magnitude I_c and opposite directions. At the central region, the magnetic field B is approximately linear.

Atoms that move away from the center will experience a position dependent Zeeman shift of their magnetic sublevels. Considering an atom with ground and excited states $|1\rangle = |J = 0\rangle$ and $|2\rangle = |J = 1\rangle$ moving in the x direction, we write the energy shift as

$$\Delta E_{\mathrm{ZS}}(x) = \mu' m_J \left|\frac{\partial B}{\partial x}\right| x, \tag{2.50}$$

where m_J is the magnetic quantum number of the atomic excited state (ground state is non degenerate) and μ' carries all relevant physical constants. The beams in each pair are made circularly polarized with opposite handedness, $\hat{\sigma}^{\pm}$. Due to selection rules, they will promote transitions that obey $\Delta m_J = \pm 1$, respectively. Since the laser is tuned below resonance, an atom located at positive (negative) x must absorb a photon from the $\hat{\sigma}^-$ ($\hat{\sigma}^+$) beam, so that the force always points towards the origin, as illustrated in figure 7. The net effect can be represented by an additional frequency shift seen by the atom. We

Figure 7 – Magnetic trapping force in 1D. With the magnetic field gradient and beam polarizations arranged as shown, the force at all x positions points towards the origin.

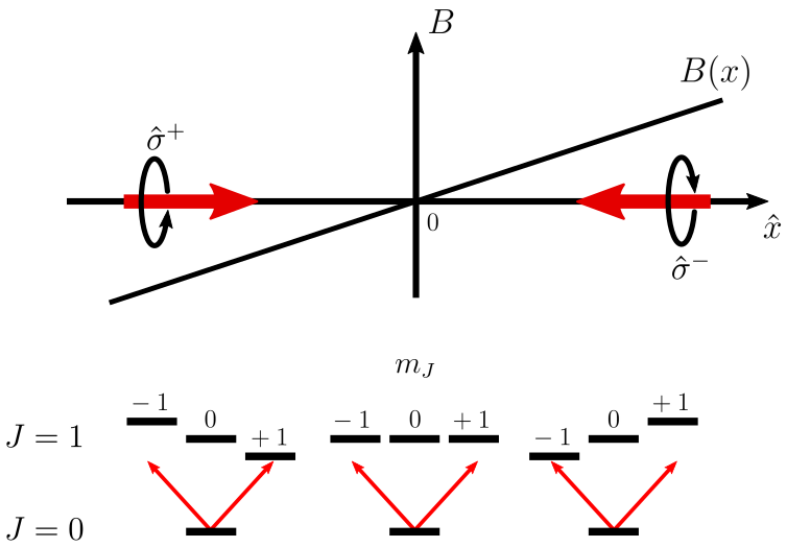

Source: The author (2021).

call it $\omega_{\mathrm{ZS}}(x) = \beta x$, where $\beta = \mu' m_j |\partial B/\partial x|/\hbar$. In three dimensions, considering equal field gradients in all directions, the total force on the atom is thus

$$\vec{\mathcal{F}}_{\mathrm{MOT}} = \Gamma \hbar k \sum_i \hat{x}_i \left[\rho_{22}(\delta - k v_i - \beta x_i) - \rho_{22}(\delta + k v_i + \beta x_i)\right]. \tag{2.51}$$

Following the same procedure as in Section 2.3.2, we take $|\beta x_i| \ll \Gamma$ and expand around $|\beta x_i| = 0$ to arrive at

$$\vec{\mathcal{F}}_{\mathrm{MOT}} = -K\vec{r} - \gamma\vec{v}, \tag{2.52}$$

where the restoring constant is

$$K = \frac{\beta\gamma}{k}. \tag{2.53}$$

2.4 Orbital angular momentum of light

It is known from Maxwell's theory that electromagnetic radiation carries energy, linear momentum and angular momentum. The angular momentum of light possesses a spin part $\vec{S}$, related to polarization, and an orbital part $\vec{L}$, related to the spatial distribution of the radiation field. The total angular momentum of an electromagnetic field in a charge free vacuum is given by

$$\vec{J} = \varepsilon_o \int \vec{r} \times (\vec{E} \times \vec{B}) d^3r, \tag{2.54}$$

and if $\vec{E}$ and $\vec{B}$ are written in terms of the vector potential $\vec{A}$, we can obtain [39]

$$\begin{aligned} \vec{J} &= \varepsilon_o \int \sum_i E_i (\vec{r} \times \nabla) A_i d^3r + \varepsilon_o \int (\vec{E} \times \vec{A}) d^3r, \\ &= \vec{L} + \vec{S}. \end{aligned} \tag{2.55}$$

In the paraxial regime, this intuitive separation is valid and useful to build understanding of multiple phenomena. It becomes troublesome, however, in the more general picture of nonparaxial solutions to Maxwell's equations [40, 41].

2.4.1 Paraxial wave equation

Maxwell's equations in vacuum with no free charge and current densities are [42]

$$\nabla \cdot \vec{E} = 0, \tag{2.56}$$

$$\nabla \cdot \vec{B} = 0, \tag{2.57}$$

$$\nabla \times \vec{E} = -\frac{\partial \vec{B}}{\partial t}, \tag{2.58}$$

$$\nabla \times \vec{B} = \varepsilon_o \mu_o \frac{\partial \vec{E}}{\partial t}. \tag{2.59}$$

By decoupling this set of equations, we obtain the wave equation for the electric field $\vec{E}(\vec{r}, t)$ of electromagnetic (EM) radiation in vacuum

$$\nabla^2 \vec{E} - \frac{1}{c^2} \frac{\partial^2 \vec{E}}{\partial t^2} = 0. \tag{2.60}$$

We assume that $\vec{E}$ can be written as

$$\vec{E}(\vec{r}, t) = \hat{\varepsilon} \mathcal{E} u(\vec{r}_\perp, z) e^{-i(kz - \omega t)} + c.c., \tag{2.61}$$

where $k = \omega/c$ is the wave number and $\mathcal{E}$ is the complex field amplitude. For optical fields, k is large, and thus e^{-ikz} carries the fast longitudinal variation of $\vec{E}$. In this manner, $u(\vec{r}_\perp, z)$ describes the transverse (and slow longitudinal) dependence of the field.

Substituting (2.61) into (2.60), projecting onto the oscillation direction of the field and performing the z derivatives, we get the equation for $u(\vec{r}_\perp, z)$

$$\nabla_\perp^2 u + \frac{\partial^2 u}{\partial z^2} - 2ik\frac{\partial u}{\partial z} = 0, \tag{2.62}$$

where $\nabla_\perp^2$ is the transverse Laplacian. We employ the slowly varying envelope approximation,

$$\left|\frac{\partial^2 u}{\partial z^2}\right| \ll \left|k\frac{\partial u}{\partial z}\right|, \tag{2.63}$$

to neglect the second derivative in z and arrive at the paraxial wave equation (PWE)

$$\nabla_\perp^2 u - 2ik\frac{\partial u}{\partial z} = 0. \tag{2.64}$$

Equation (2.64) describes the evolution of the transverse distribution of the radiation field in vacuum. It is interesting to note that the PWE is mathematically equivalent to the Schrödinger equation for a 2D free particle. Therefore, conclusions concerning physical aspects of u may be drawn in analogy to the free particle wave function. As an example, we note that u satisfies the continuity equation

$$\frac{\partial |u|^2}{\partial z} + \nabla_\perp \cdot \vec{\mathrm{v}} = 0, \tag{2.65}$$

where the current is

$$\vec{\mathrm{v}} = \frac{i}{2k}(u^*\nabla_\perp u - u\nabla_\perp u^*). \tag{2.66}$$

This continuity equation is analogous to the transport-of-intensity equation [43]. We integrate (2.65) over a plane surface $\mathcal{S}$ with normal unit vector $\hat{\mathrm{s}}$ parallel to $\hat{z}$ and contour $\partial\mathcal{S}$. With 2D Gauss' theorem (or the 3D version in the volume $\mathcal{S} \times \Delta z$, where Δz is a small longitudinal length), we get

$$\iint_{\mathcal{S}} \frac{\partial |u|^2}{\partial z} dS + \int_{\partial\mathcal{S}} (\vec{\mathrm{v}} \cdot \hat{\mathrm{n}}) dt = 0, \tag{2.67}$$

where $\hat{\mathrm{n}}$ is a unit vector normal to the contour $\partial\mathcal{S}$ pointing outward and dt is an element of the contour. We can write

$$\frac{dP_{\mathcal{S}}}{dz} + \Phi_{\partial\mathcal{S}} = 0, \tag{2.68}$$

where $P_{\mathcal{S}} = \iint_{\mathcal{S}} |u|^2 dS$ is the power of u contained in $\mathcal{S}$ and $\Phi_{\partial\mathcal{S}} = \int_{\partial\mathcal{S}} (\vec{\mathrm{v}} \cdot \hat{\mathrm{n}}) dt$ is the flux of the current $\vec{\mathrm{v}}$ through $\partial\mathcal{S}$[1]. If $\mathcal{S}$ is taken as the infinite transverse plane, $P_{\mathcal{S}}$ becomes the total power and the flux term goes to zero, leading to

$$\frac{dP_{\mathrm{total}}}{dz} = 0, \tag{2.69}$$

and we conclude that the total power in a paraxial beam propagating in vacuum is conserved.

[1] In the following subsection, it will become evident that $\vec{\mathrm{v}}$ is related to the time averaged linear momentum density $\langle \vec{p} \rangle$ of an electromagnetic wave described by the amplitude function u, and thus the flux of $\vec{\mathrm{v}}$ is related to the flux of linear momentum.

2.4.2 Angular momentum in the paraxial regime

In the Lorenz gauge, the vector potential $\vec{A}$ satisfies the wave equation. We describe it as a linearly polarized traveling wave of the form [1]

$$\vec{A}(\vec{r},t) = \hat{x}\mathcal{A}_o u(\vec{r}_\perp, z)e^{-i(kz-\omega t)}, \tag{2.70}$$

where $u(\vec{r}_\perp, z)$ satisfies the PWE. The electric and magnetic fields in this case are written as [39, 44]

$$\begin{aligned}\vec{E} &= -\frac{\omega\mathcal{A}_o}{k}\left[\hat{x}iku + \hat{z}\frac{\partial u}{\partial x}\right]e^{-i(kz-\omega t)},\\ \vec{B} &= -\mathcal{A}_o\left[\hat{y}iku + \hat{z}\frac{\partial u}{\partial y}\right]e^{-(ikz-\omega t)}.\end{aligned} \tag{2.71}$$

To obtain these forms, we neglected $\partial^2 u/\partial y\partial x$ and considered $|\partial u/\partial z| \ll |ku|, |\partial^2 u/\partial x^2| \ll |k^2 u|$. We see that the electromagnetic wave described by (2.71) is not transverse. The longitudinal components of $\vec{E}$ and $\vec{B}$, however, are small compared to ku, and for calculations it is sufficient to consider only the transverse components of the electric and magnetic fields. The time average of the linear momentum density is [1]

$$\begin{aligned}\langle\vec{p}\rangle &= \varepsilon_o\left\langle\vec{E}\times\vec{B}\right\rangle,\\ &= \frac{\varepsilon_o}{2}\,\mathrm{Re}[\vec{E}\times\vec{B}^*].\end{aligned} \tag{2.72}$$

Taking $\mathcal{A}_o = 1$ for simplicity, we find

$$\langle\vec{p}\rangle = i\omega\frac{\varepsilon_o}{2}\left(u^*\nabla_\perp u - u\nabla_\perp u^*\right) + \omega k\varepsilon_o|u|^2\hat{z}. \tag{2.73}$$

Specializing to cylindrical coordinates, the azimuthal component of $\langle\vec{p}\rangle$ can be found

$$p_\phi = -\omega\varepsilon_o\,\mathrm{Im}\left[\frac{u^*}{r}\frac{\partial u}{\partial\phi}\right]. \tag{2.74}$$

The time average angular momentum density is $\langle\vec{j}\rangle = \vec{r}\times\langle\vec{p}\rangle$, and its longitudinal component is

$$j_z = -\omega\varepsilon_o\,\mathrm{Im}\left[u^*\frac{\partial u}{\partial\phi}\right], \tag{2.75}$$

and the total angular momentum in the z direction per unit length is thus

$$J_z = \iint j_z dS. \tag{2.76}$$

Moreover, the total energy per unit length of the radiation field is

$$\begin{aligned}W &= \frac{1}{2}\iint\left(\varepsilon_o|\vec{E}|^2 + \frac{1}{\mu_o}|\vec{B}|^2\right)dS,\\ &\simeq \varepsilon_o\omega^2,\end{aligned} \tag{2.77}$$

where we neglected the axial components of $\vec{E}$ and $\vec{B}$.

2.4.3 The Laguerre-Gaussian mode

A solution to the PWE of special interest in this work is the well known Laguerre-Gaussian (LG) mode, denoted as

$$u_{\ell p}(r,\phi,z) = \frac{C_{\ell p}}{w(z)}\left(\frac{\sqrt{2}r}{w(z)}\right)^{|\ell|} L_p^{|\ell|}\left[\frac{2r^2}{w^2(z)}\right] e^{-\frac{r^2}{w^2(z)}} \exp\left\{-i\ell\phi + i\zeta(z) - i\frac{kr^2}{2R(z)}\right\}, \quad (2.78)$$

where $C_{\ell p} = \sqrt{2p!/\pi(p+|\ell|)!}$ is the normalization constant, $L_p^{|\ell|}(\cdot)$ is the associated Laguerre polynomial, $w(z) = w_o\sqrt{1+(z/z_R)^2}$ is the beam waist, $R(z) = z\left[1+(z_R/z)^2\right]$ is the curvature radius, $\zeta(z) = (2p+|\ell|+1)\tan^{-1}(z/z_R)$ is the Gouy phase, $z_R = kw_o^2/2$ is the Rayleigh range and w_o is the minimum beam waist. The transverse and longitudinal characteristic lengths of an LG mode are w_o and z_R, respectively. To fully define an LG mode, one of the pairs (w_o, z_R), $(w_o, k$ or $\lambda)$, $(z_R, k$ or $\lambda)$, must be known.

A linearly polarized light beam described by (2.78) carries well defined OAM in the z direction, which is closely related to the azimuthal phase factor $\exp(-i\ell\phi)$. This term introduces a phase singularity, an optical vortex, at the beam center, where the intensity is zero. The integer $\ell \in (-\infty, \infty)$ is called the topological charge and defines the OAM in the beam [1]. The phase fronts of LG beams are twisted around the propagation axis as shown in Figure 8, with the number and handedness of the helices defined by the magnitude and sign of ℓ, respectively. The Poynting vector $\vec{S} = \vec{E} \times \vec{B}/\mu_o$, which is normal to the phase-fronts at all positions, spirals around the beam axis [1]. The momentum density thus possesses an off axis azimuthal component, that gives rise to the angular momentum of the beam [41].

Figure 8 – Phase fronts of (a) plane wave beams, $\ell = 0$, and of LG beams with (b) $\ell = 1$, (c) $\ell = 2$ and (d) $\ell = 3$.

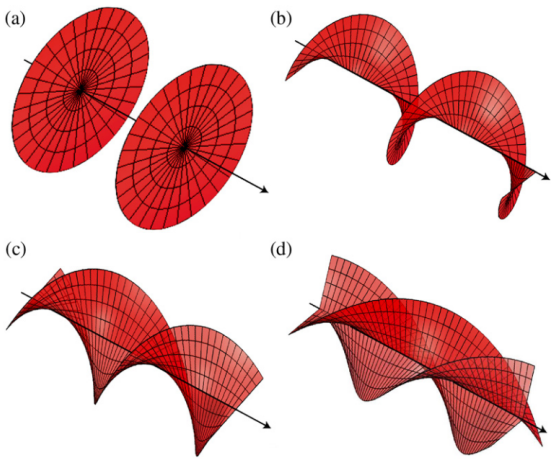

Source: Taken from reference [41].

Using equation (2.75) with $u = u_{\ell p}$, the density of angular momentum in the z direction is

$$j_z = \omega\varepsilon_o\ell|u_{\ell p}|^2. \quad (2.79)$$

With the fact that $u_{\ell p}$ is normalized, the total angular momentum in the z direction per unit length (2.76) can be found

$$J_z = \omega\varepsilon_o\ell. \quad (2.80)$$

The ratio of the angular momentum along the beam axis to the field energy W, given by equation (2.77), is found

$$\frac{J_z}{W} = \frac{\ell}{\omega}. \tag{2.81}$$

This can be generalized to the case of a field with circular polarization [1],

$$\frac{J_z}{W} = \frac{\ell + \sigma_z}{\omega}, \tag{2.82}$$

where $\sigma_z = \pm 1$ for left- or right-circular polarizations. It is known that a photon from a circularly polarized light beam possesses an angular momentum given by

$$S_z = \sigma_z \hbar, \tag{2.83}$$

which is regarded as the spin of the photon. Thus, (2.82) suggests that the orbital angular momentum in the z direction per photon in a Laguerre-Gaussian beam is

$$L_{z,\text{photon}} = \ell\hbar. \tag{2.84}$$

Contrary to the spin component of the angular momentum of a photon, its OAM can assume an infinite number of values, and this high dimensionality represents a useful tool for information multiplexing. The other index characterizing the mode, $p \in [0, \infty)$, is called the radial index. It is related to the number of dark rings in the intensity profile of $u_{\ell p}$, but doesn't have a straightforward connection with a physical quantity as is the case for ℓ. In recent years, however, the radial index has been the subject of theoretical works [45, 46] that have enlightened its significance. The intensity and phase distributions of LG modes with different orders ℓ and p are shown in Figure 9.

Figure 9 – Intensity and phase distributions of $u_{\ell p}$ at $z = 0$ for multiple ℓ and p.

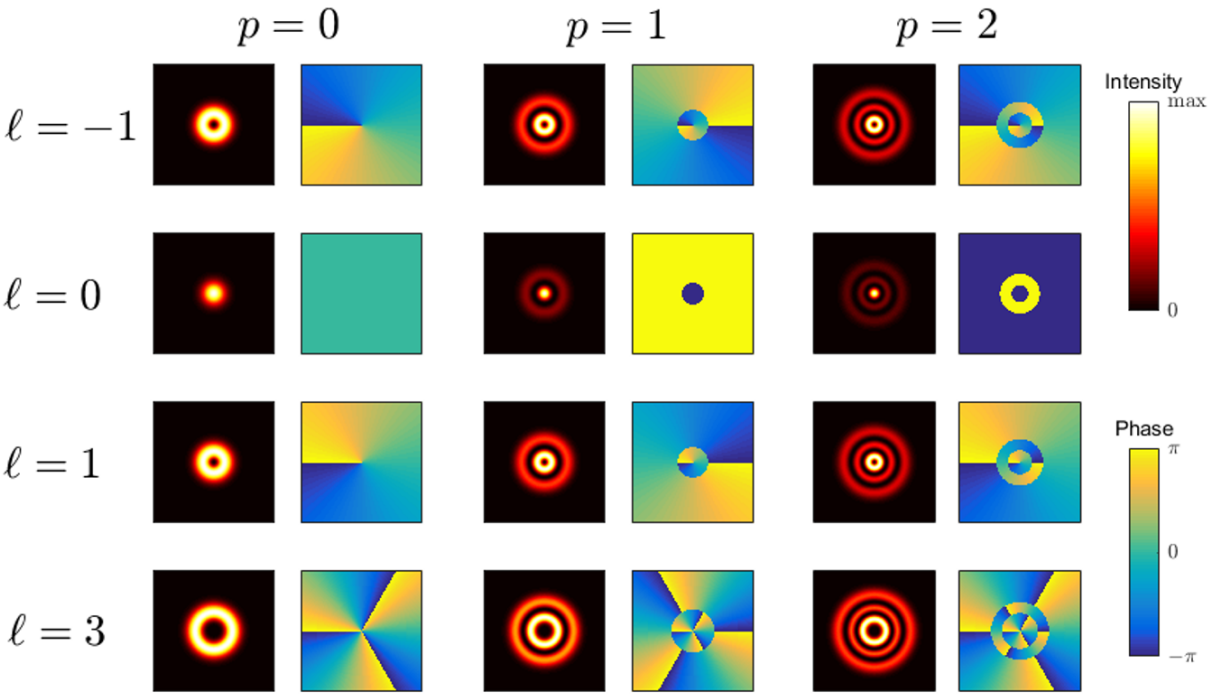

Source: The author (2021).

LG modes form a complete orthonormal set of functions on the transverse plane, satisfying

$$\iint u_{\ell p} u^*_{\ell' p'} r dr d\phi = \delta_{\ell,\ell'} \delta_{p,p'}, \tag{2.85}$$

$$\sum_{\ell,p} u_{\ell p}(\vec{r}_\perp, z) u^*_{\ell p}(\vec{r}'_\perp, z) = \delta(\vec{r}_\perp - \vec{r}'_\perp). \tag{2.86}$$

This makes the set $\{u_{\ell p}\}$ a basis suitable for problems involving cylindrical symmetry. Furthermore, LG modes are one out of three families of orthonormal solutions to the PWE that are closely related. The other two are the Hermite-Gaussian (HG) and Ince-Gaussian (IG), that possess rectangular and elliptical symmetries, respectively. LG and HG solutions are limiting cases of the IG solution.

2.4.4 Generation of beams with OAM

Allen *et al.* also discussed the conversion of Hermite-Gaussian beams to LG beams, which is accomplished by using mode converters composed of astigmatic optical components [47]. LG modes can also be generated from fundamental Gaussian beams using a spiral phase plate [48] or a computer generated hologram mask [49]. This mask is a diffraction grating with a forked structure at the center that has as many dislocations as the order of the desired singularity, ℓ. The first order diffracted beam is shown to possess the approximate intensity distribution of an LG beam with topological charge ℓ and radial index $p = 0$. Figure 10 shows one of these forked gratings and the first order diffracted beam. Both spiral phase plates and computer generated holograms can also be used to efficiently generate LG beams with higher radial orders $p \neq 0$ [50, 51]. The combination of computer generated holograms and spatial light modulators (SLM) offers a versatile method for the generation of structured light modes and is vastly employed in the field of light OAM. An SLM is a device used to introduce a spatially dependent phase-modulation to a light beam. Modern SLMs are controlled with easy to use computer programs that allow to quickly select the desired hologram and the device response is practically immediate. In the next chapter we describe the basic structure of an SLM.

Figure 10 – (a) Forked grating used to generate an LG mode with $\ell = 1$. Red box shows a close up of the central dislocation. (b) Diffraction of a fundamental Gaussian beam by the $\ell = 1$ forked grating into zeroth and first orders.

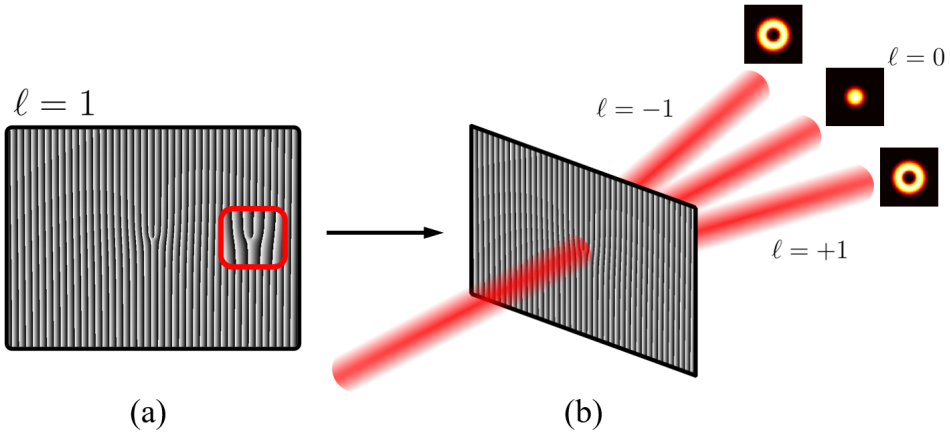

Source: The author (2021).

2.5 Nonlinear optics

Nonlinear optics studies the interaction of strong light fields with matter, such that the medium response depends nonlinearly on the electric field of light. Second harmonic generation (SHG), where two photons with frequency ω interact nonlinearly inside a crystal to create a photon with frequency 2ω, was the first nonlinear optical process to be experimentally demonstrated [52]. It was achieved using a ruby laser and a quartz crystal, only one year after the construction of the first laser by Maiman, in 1960.

Inside matter, Maxwell's macroscopic equations [42] lead to the wave equation for the electric field $\vec{E}$ of light

$$\nabla^2\vec{E} - \frac{1}{c^2}\frac{\partial^2\vec{E}}{\partial t^2} = \mu_o\frac{\partial\vec{P}}{\partial t^2}, \tag{2.87}$$

where $\vec{P}$ is the macroscopic polarization vector and describes the medium response to the incident field. It can be separated in a linear part and a nonlinear one, $\vec{P} = \vec{P}_{\rm L} + \vec{P}_{\rm NL}$, where

$$\begin{aligned} \vec{P}_{\rm L} &= \varepsilon_o\chi^{(1)}\cdot\vec{E}, \\ \vec{P}_{\rm NL} &= \varepsilon_o\left(\chi^{(2)} : \vec{E}\vec{E} + \chi^{(3)} \vdots \vec{E}\vec{E}\vec{E} + \cdots\right). \end{aligned} \tag{2.88}$$

The linear susceptibility, $\chi^{(1)}$, is related to absorption and the index of refraction, while the multiple nonlinear susceptibilities in the expansion of $\vec{P}_{\rm NL}$, $\chi^{(n)}$, are responsible for all nonlinear optical phenomena that occur in the medium. The $\chi^{(n)}$ are tensors of rank $(n+1)$ and the products of fields that accompany these quantities are tensorial products. Symmetries in the medium reduce the number of independent elements of $\chi^{(n)}$. For instance, in centrosymmetric media, all even order susceptibilities are null, $\chi^{(2n)} = 0$, and the nonlinearity of lowest order is given by $\chi^{(3)}$.

The nonhomogenous wave equation (2.87) together with the source term given by the medium response (2.88) is an essential part of the mathematical description of nonlinear optical phenomena in various configurations and regimes. In the specific case of four-wave mixing, a third order nonlinear process, we consider in this work, incident fields $\vec{E}_a$ and $\vec{E}_b$ with frequencies ω_a and ω_b and propagation directions $\vec{k}_a$ and $\vec{k}_b$ (figure 11), interact with an isotropic and centrosymmetric nonlinear medium to generate field $\vec{E}_s$ with frequency $\omega_s = 2\omega_a - \omega_b$ and propagation direction $\vec{k_s} = 2\vec{k}_a - \vec{k}_b$. It can be shown that the scalar wave equation for the generated field complex amplitude $E_s = \mathcal{E}_s e^{-i\vec{k}_s\cdot\vec{r}}$ takes the form

$$\nabla^2 E_s + k_s^2 E_s + = -\frac{\omega_s^2}{c^2}\left\{i\mathrm{Im}[\chi^{(1)}(\omega_s)]E_s + \chi^{(3)}(\omega_s = 2\omega_a - \omega_b)E_a^2 E_b^*\right\}, \tag{2.89}$$

where $k_s = \omega_s n_s/c$,

$$n_s^2 = 1 + \mathrm{Re}[\chi^{(1)}(\omega_s)] \tag{2.90}$$

is the index of refraction in the medium at frequency ω_s. Here $\chi^{(1)}(\omega_s)$ and $\chi^{(3)}(\omega_s = 2\omega_a - \omega_b)$ are both scalars and their detailed forms, related to the characteristics of the medium, are deduced in Chapter 4. The wave equations that describe the evolution of fields E_a and E_b can be found in a similar form. In ref. [10], where field E_a is strong, a solution is given for the coupled evolution of the weak and generated fields, E_b and E_s. In the configuration we consider, however, both incident fields are strong, and we expect them to undergo little variation due to linear or nonlinear effects in the interaction region, which is considered small in comparison with the characteristic length of the beams.

Figure 11 – Spatial orientation of the wave-vectors of the incident and generated beams involved in the FWM process and the phase mismatch $\Delta\vec{k}$.

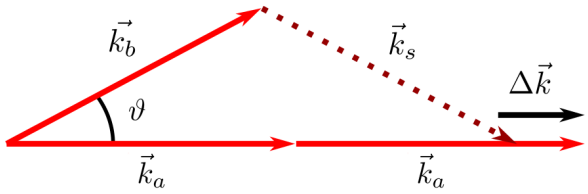

Source: The author (2021).

In Chapter 4 we'll derive a solution to (2.89) considering the full spatial dependence of the incident fields, that will be given by Gaussian or Laguerre-Gaussian distributions. For the moment, we'll consider beams with plane wave-fronts only. The solution in this configuration is well known and we analyze two limiting cases that will be recovered in Chapter 4. We thus neglect the transverse derivatives of E_s and employ the slowly varying envelope approximation to arrive at

$$\frac{\partial \mathcal{E}_s}{\partial z} = -\alpha_{\text{lin}}\mathcal{E}_s + \kappa\mathcal{E}_a^2\mathcal{E}_b^* e^{-i\Delta\vec{k}\cdot\vec{r}}, \tag{2.91}$$

where

$$\alpha_{\text{lin}} = -\frac{\omega_s}{2cn_s}\text{Im}[\chi^{(1)}(\omega_s)] \tag{2.92}$$

is the absorption coefficient,

$$\kappa = -i\frac{\omega_s}{2cn_s}\chi^{(3)}(\omega_s = 2\omega_a - \omega_b) \tag{2.93}$$

is the nonlinear coupling and $\Delta\vec{k} = 2\vec{k}_a - \vec{k}_b - \vec{k}_s \simeq (2k_a - k_b - k_s)\hat{z}$ is the phase mismatch (figure 11),

$$\Delta k = \frac{1}{c}[2\omega_a n_a - (\omega_b n_b + \omega_s n_s)\cos\vartheta]. \tag{2.94}$$

Making the substitution $\tilde{\mathcal{E}}_s = \mathcal{E}_s e^{\alpha_{\text{lin}} z}$, we get

$$\frac{\partial \tilde{\mathcal{E}}_s}{\partial z} = \kappa\mathcal{E}_a^2\mathcal{E}_b^* e^{\alpha_{\text{lin}} z - i\Delta k z}. \tag{2.95}$$

With the initial condition $\tilde{\mathcal{E}}_s(0) = \mathcal{E}_s(0) = 0$, the solution to the FWM field $\mathcal{E}_s(z)$ is

$$\mathcal{E}_s(z) = \kappa\mathcal{E}_a^2\mathcal{E}_b^*\left[\frac{e^{-i\Delta k z} - e^{-\alpha_{\text{lin}} z}}{\alpha_{\text{lin}} - i\Delta k}\right]. \tag{2.96}$$

In a medium with extension L, in a case where the linear absorption can be neglected, the generated signal power is given by

$$P_s \propto |\chi^{(3)}\mathcal{E}_a^2\mathcal{E}_b^*|^2 \times \text{sinc}^2\left(\frac{\Delta k L}{2}\right). \tag{2.97}$$

Also, in a phase-matched setting, we have

$$P_s \propto |\chi^{(3)}\mathcal{E}_a^2\mathcal{E}_b^*|^2 \times \left|\frac{T(L)}{\alpha_{\text{lin}}}\right|^2, \tag{2.98}$$

where $T(L) = 1 - e^{-\alpha_{\text{lin}} L}$ is the Beer-Lambert transmission factor through the medium of size L. In Chapter 4 we show that, under the approximations therein considered, we obtain a term similar to that in square brackets of equation (2.96). Consequently, the terms that multiply $|\chi^{(3)} \mathcal{E}_a^2 \mathcal{E}_b^*|^2$ in equations (2.97) and (2.98) will be recovered.

3 THE EXPERIMENT

All experiments were performed on samples of cold ^{87}Rb atoms obtained with a magneto-optical-trap (MOT), the main apparatus in this project. In this chapter we discuss various details regarding the operation of the MOT and the detection of the four-wave mixing signals. We use three lasers, namely the cooling, repump and FWM lasers. They are all tunable diode lasers from Sanyo, model DL7140-201S, and we use a homemade electronic box for temperature and current control. Figure 12 shows a representation of the hyperfine transitions excited by each laser in the experiment.

Figure 12 – Hyperfine energy levels of the D_2 line of ^{87}Rb and the transitions excited by the cooling, repump and FWM lasers.

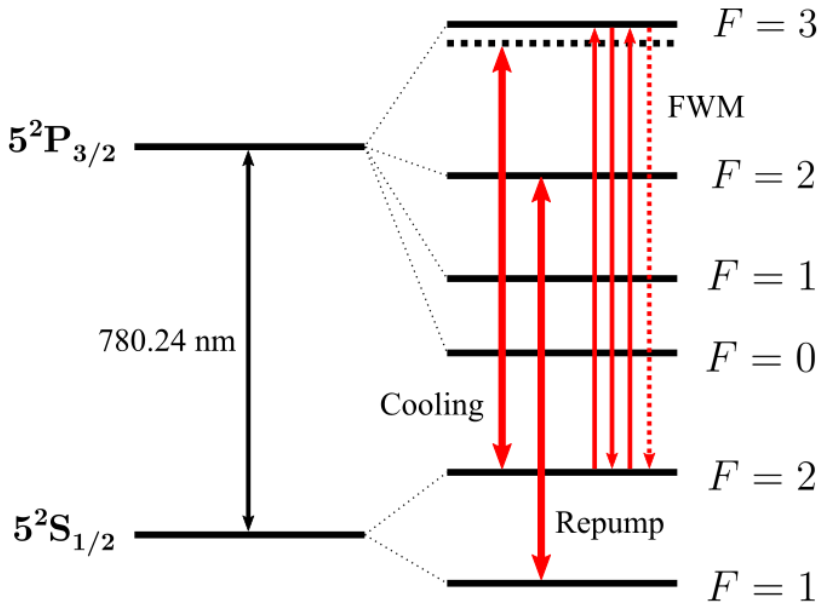

Source: The author (2021).

All lasers go through a saturated absorption (SA) experiment, that allows to control their frequencies and also provides a frequency reference. The saturated absorption experiment setup used is shown in figure 13. A small portion of the total power of the laser output is reflected by a piece of glass and passes through the Rb cell. This is the pump beam. The reflected beam, which is attenuated by filter F, is the probe. Pump and probe are superimposed inside the cell containing Rb vapour and the probe is detected by a photodetector (PD). By sweeping the frequency of the laser, one gets the saturated absorption spectrum (SAS).

Figure 13 – Basic setup of a saturation absorption experiment. OI is an optical isolator.

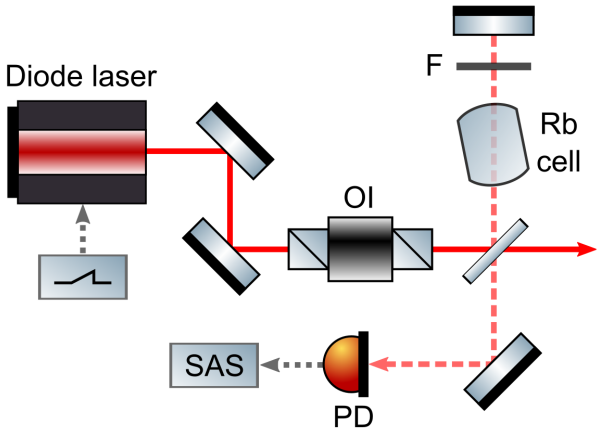

Source: The author (2021).

3.1 Magneto-optical trap setup

The cooling laser is setup to excite the $|5S_{1/2}; F_g = 2\rangle \rightarrow |5P_{3/2}; F_e = 3\rangle$ hyperfine cyclic transition of ^{87}Rb. It is tuned to the cross-over transition between $|F_e = 1\rangle$ and $|F_e = 3\rangle$, 212 MHz below resonance, using a homemade locking system and the saturated absorption spectrum as a reference signal. An acousto-optic modulator (AOM) then introduces a frequency shift of 200 MHz, leaving it approximately 12 MHz below the desired resonance frequency. The zeroth order diffracted from the AOM is used as a guide beam for the alignment of the FWM laser beams. The first order is sent into a Toptica Photonics Boosta amplifier, which converts an input of 12 mW to about 350 mW. The AOM is also used in the temporal control of the experiment, which will be commented in the next section.

The amplified beam is then coupled to an optical fiber via a Fiber Dock, also from Toptica Photonics, that helps eliminating the cross-talk between the mechanical degrees of freedom during alignment of the fiber and maintains the fiber coupling for longer periods of time. It is, however, a component that presents a reasonable power loss. The coupling efficiency of this and all other fibers used during the experiments was around 65%. The beam is then divided in two using a series of optical components. One of the beams goes direcly to the main Rb cell via an optical fiber and becomes the z arm (vertical) of the MOT. The other beam is mixed with the repump beam via a fused fiber coupler (FFC). The fiber coupler has two outputs, containing light from cooling and repump lasers, that are sent to the MOT and become the x and y arms. The power provided by the cooling laser to each arm is very sensible to the overall alignment and it varied around $5 - 7$ mW during the experiments. Figure 14 shows the setup of the cooling laser.

Due to the motion of the atoms and the high intensity of the beams, the cooling laser may promote atoms to $|5P_{3/2}; F_e = 2\rangle$, instead of $F_e = 3$, and these atoms can decay to $|5S_{1/2}; F_g = 1\rangle$. At this point, they can no longer interact with the cooling laser. For this reason, the repump laser is tuned to the $|5S_{1/2}; F_g = 1\rangle \rightarrow |5P_{3/2}; F_e = 2\rangle$ transition and is responsible for emptying the population of state $|5S_{1/2}; F_g = 1\rangle$ so that atoms can interact with the cooling laser again. The repump laser provides about $1 - 1.3$ mW to both x and y arms and is not as sensible as the cooling laser. It was not frequency locked during experiments, and thus its frequency usually drifts away and constant manual adjustments

Figure 14 – Preparation of the cooling laser. The SA spectrum is used as a reference signal for the frequency locking system (homemade). The first diffracted order from the acousto-optic modulator (AOM) is sent into the amplifier (AMP). The zeroth order is used as a guide beam for the FWM laser beams.

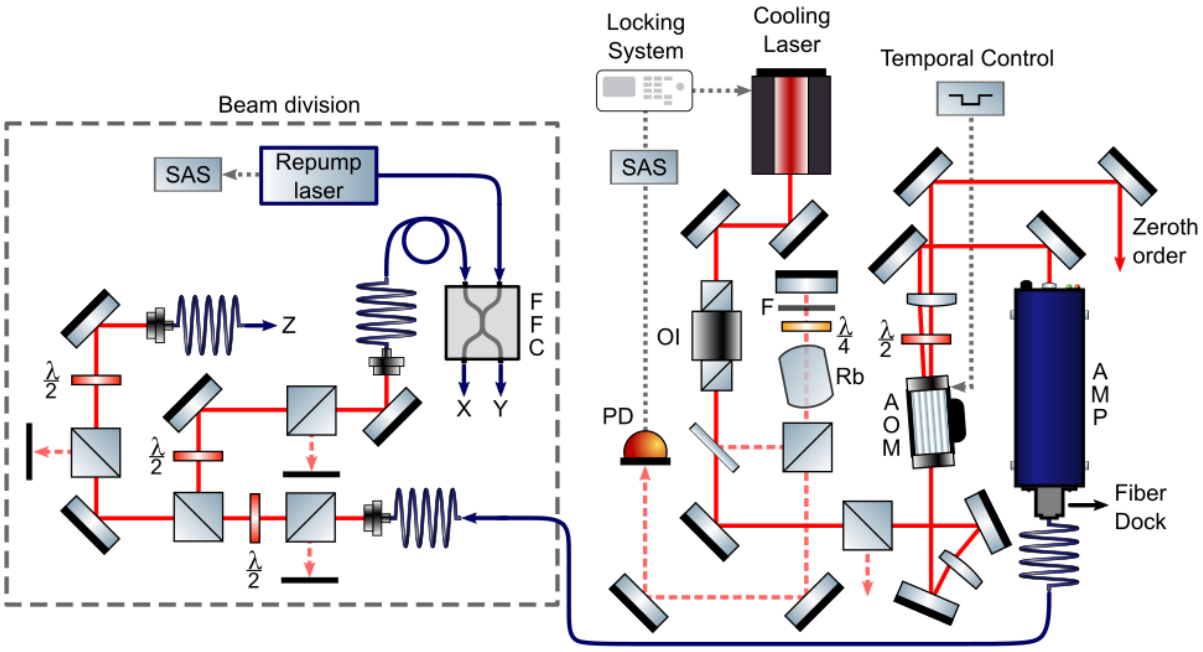

Source: The author (2021).

must be made during experiments.

The quadrupole magnetic field is attained with a pair of circular coils in an anti-Helmholtz setting. In order to shield the experiment from Earth's spurious magnetic field and possibly other fields, we use a Faraday cage. The atoms are provided by a rubidium alkali metal dispenser (AMD), through which a high electric current is imposed to release atoms. The released atoms are contained inside the main Rb cell, which is connected to an ionic vacuum pump (VP) from Varian. The pump maintains an extremely low pressure inside the cell, $P_{\text{cell}} \approx 10^{-9}$ Torr (with no current through the Rb getter), which is necessary to reduce collisions and increase the lifetime of the cooled atom cloud. At the output end of all fibers of the MOT arms, a telescope is used to increase the beam size and a quarter-wave plate makes them circularly polarized. Inside the cell, the beams intersect far from the glass walls. They are then reflected by a mirror and another $\lambda/4$ plate switches the handedness of their circular polarizations, $\hat{\sigma}^{\pm} \rightarrow \hat{\sigma}^{\mp}$, thus creating the configuration needed for the trapping of atoms near the intersection. In figure 15 we show a scheme of the MOT arrangement.

With the system setup as described so far, we obtain cold atom clouds with approximately 10^9 atoms and diameters of $D \approx 3-4$ mm. Figure 16 shows a picture of the main Rb cell with the cloud of cold Rb atoms inside.

Figure 15 – Top and side views of the MOT arrangement. Beams a and b passing through the Rb cell are the FWM laser beams. VP, AMD and FFC refer to vacuum pump, alkali metal dispenser and fused fiber coupler, respectively.

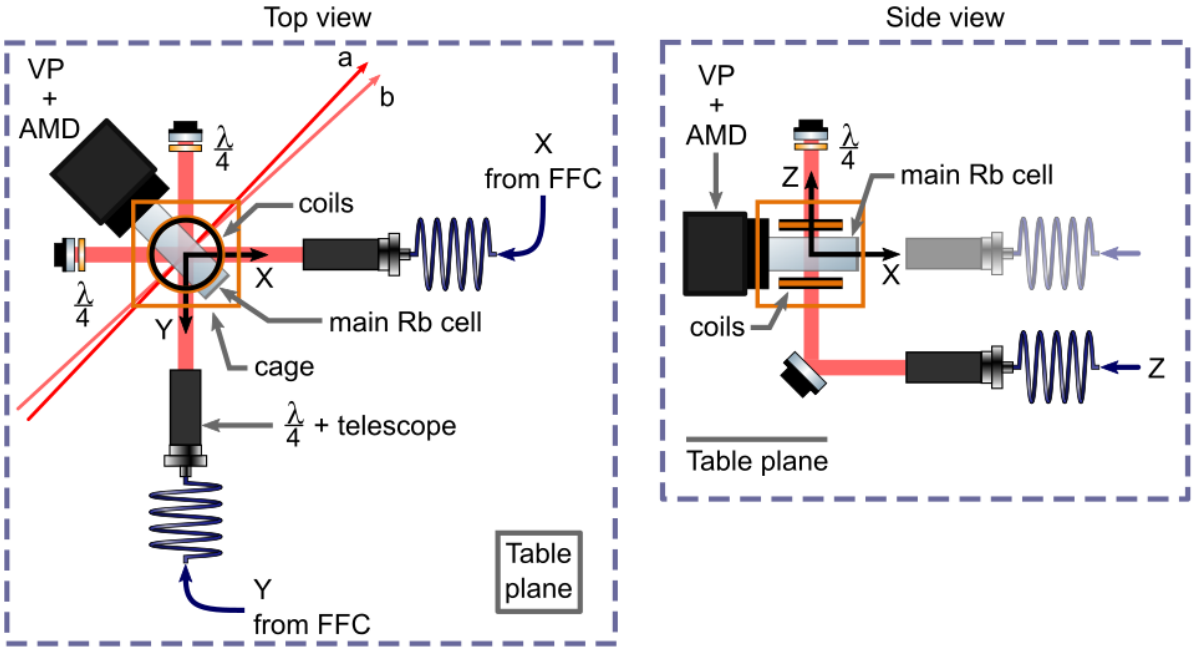

Source: The author (2021).

Figure 16 – Cold atom cloud obtained with our magneto-optical trap.

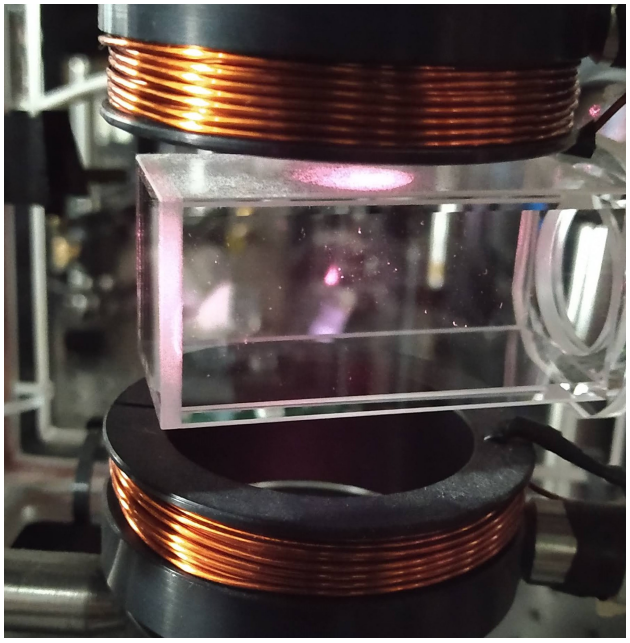

Source: The author (2021).

3.2 Four-wave mixing setup

The FWM laser is also setup to excite the $|5S_{1/2}, F_g = 2\rangle \rightarrow |5P_{3/2}, F_e = 3\rangle$ transition. Since this is the same transition that the cooling laser excites, we use a temporal control to turn the cooling laser off before the FWM process. The quadrupole magnetic field generated by the circular coils is also turned off. After a small delay, so that the atoms can decay from the $|F_e = 3\rangle$ state, the FWM time window begins. The FWM laser is not frequency locked in the current configuration. We modulate the current that goes to the laser diode with a ramp signal that varies its frequency around the desired transition during the FWM window. The whole FWM spectra is obtained in a single window.

The FWM beam arrives at the main table via an optical fiber. It passes through an AOM in a double-pass configuration and then gets divided into two, to produce the two beams E_a and E_b used to drive the FWM process (see Fig. 17). Both beams must intersect inside the main Rb cell, at the location of the cloud of cold atoms. This alignment is performed with the aid of a pair of masks with guiding holes. The two masks are separated by a distance of about 1 m with the MOT region located halfway between them. The separation between the holes is approximately 6 mm. This gives an angle $\vartheta \approx 8$ mrad between $\vec{k}_a$ and $\vec{k}_b$. These masks are also used for the alignment of the FWM signal detectors using the zeroth diffracted order of the cooling laser.

The minimum beam waist (that occurs at the intersection) throughout most of the measurements was $w_o \approx 1$ mm, and this is the value that will be considered in the present work, unless otherwise stated. The Rayleigh range for $w_o = 1$ mm and wavelength $\lambda = 780$ nm is $z_R = \pi w_o^2/\lambda \approx 4$ m. The FWM beams must popagate considerable distances, compared to z_R, before reaching the interaction region and the detection positions, and thus the incident beams must be well collimated.

Figure 17 – Preparation of the FWM laser. Acousto-optic modulator is setup in a double-pass configuration.

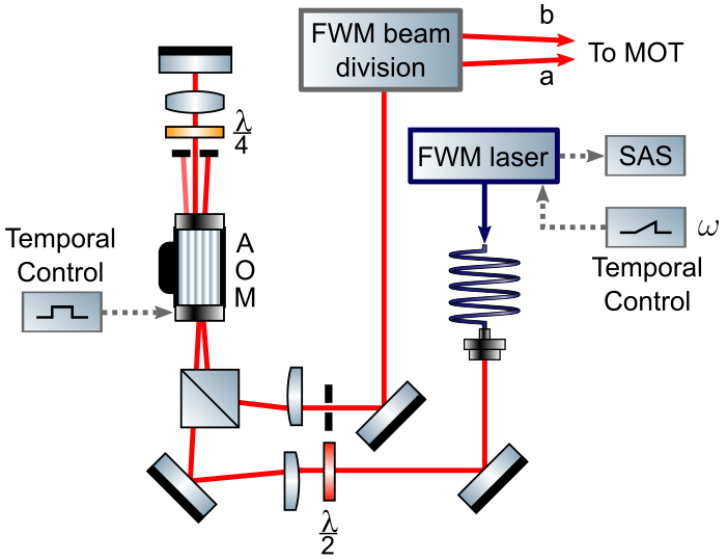

Source: The author (2021).

3.3 Spatial light modulator

In this work we use the LCOS-SLM (liquid crystal on silicon spatial light modulator) model X10468-02 from Hamamatsu Photonics, shown in figure 18.

Figure 18 – LCOS-SLM model X10468-02 from Hamamatsu Photonics. Main parts are indicated.

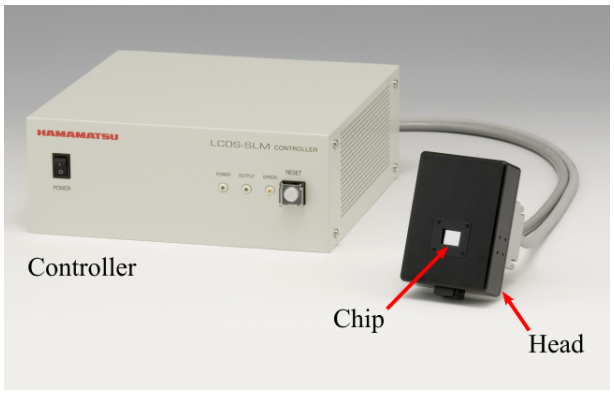

Source: Modified from the SLM datasheet [53].

In the LCOS-SLM chip, a nematic liquid crystal (LC) is layered on top of an array of pixels and enclosed by a glass plate (figure 19a). The LC molecules are uniaxial, i.e., possess an ordinary and an extraordinary index of refraction, n_o and n_e, respectively, in orthogonal directions (figure 19b). Their orientation is locally controlled by applying a specific voltage to each pixel. This results in a local change of the index of refraction, that leads to the phase modulation of the incoming light, which is then reflected by a dielectric mirror for the desired wavelengths. Note that due to the geometry of the LC molecules,

Figure 19 – (a) Elements of the LCOS-SLM chip from Hamamatsu Photonics and (b) depiction of the uniaxial liquid crystal molecule with the indices of refraction n_o and n_e along the y and x directions, respectively.

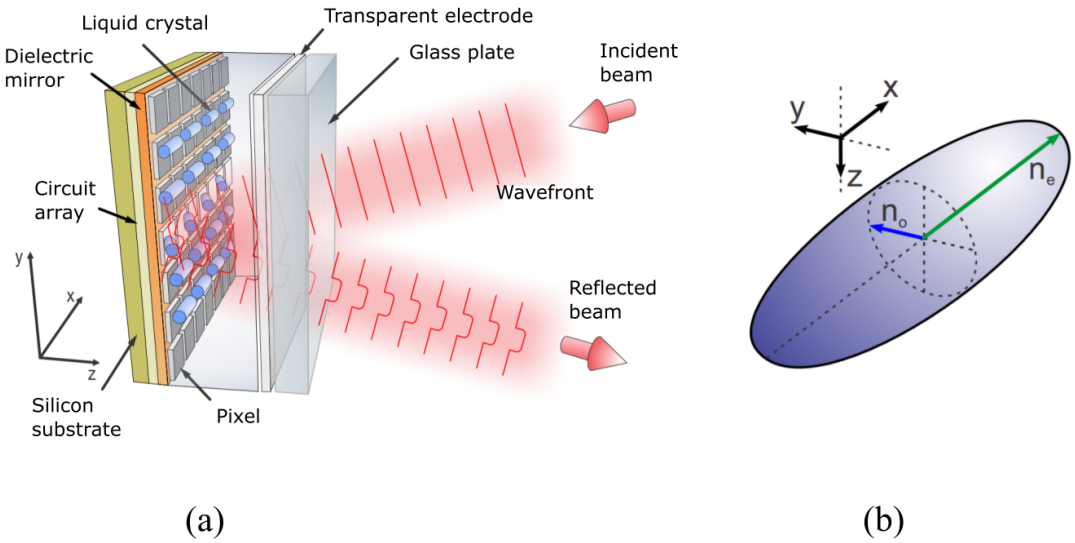

Source: Adapted from [54].

the phase modulation will only occur if the direction of oscillation of the incoming electric field is parallel to the plane that contains both the ordinary and extraordinary axes, the x-y plane [54].

The modulator is operated using a computer connected to the SLM controller via standard video connectors, which is connected to the SLM head via a pair of robust cables. The desired phase modulation is defined by an arbitrary gray-scale image file with the appropriate size. The intensity of each pixel in the image is translated into voltage in the corresponding pixel of the array, that changes the LC orientation in that region. The image is "printed" onto the chip and, subsequently, onto the phase distribution of the incident beam [54]. To generate LG beams of various ℓ orders we use forked diffraction patterns, like the one shown in Chapter 2.

For the experiments involving OAM, the LCOS-SLM was introduced in the path of beam E_b, as shown in figure 20. A telescope is used to increase the beam size so that it covers a larger portion of the SLM chip. The output beam is reflected at a small angle and a second telescope reduces the beam waist back to its original size, approximately. The resultant diffraction pattern with the zeroth and first diffracted orders is also shown. The positive ℓ order is selected and both beams E_a and E_b are sent to the MOT. In figure 21 we present in detail the intensity profile of the zeroth and first order diffracted beams from the SLM using the $\ell = 1$ forked grating. We see that the first order beam shows a sensible asymmetry, which is a result of slight off centering of the fundamental Gaussian beam on the SLM chip.

Figure 20 – Defining the two beams, E_a and E_b, responsible for the FWM process. The phase front of E_b is modulated by the SLM before being sent to the MOT. CCD image shows the the diffracted orders from the SLM for $\ell = 1$.

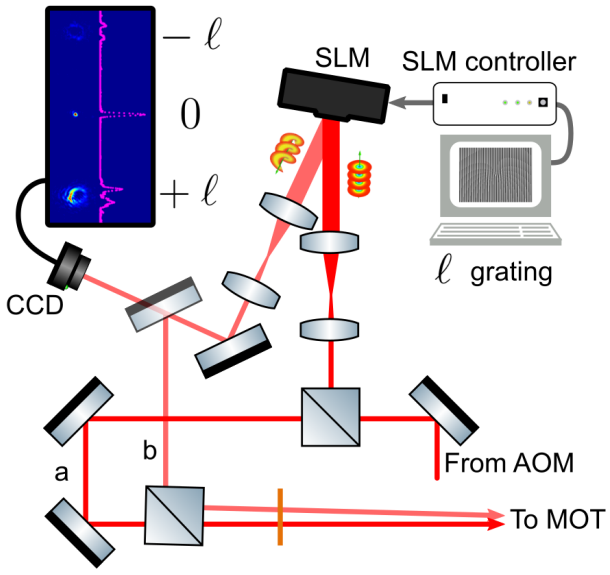

Source: The author (2021).

Figure 21 – Intensity profile of zeroth and first order beams diffracted from the SLM using a forked grating with $\ell = 1$. Inset shows a close up of the first order beam and the x and y radial profiles.

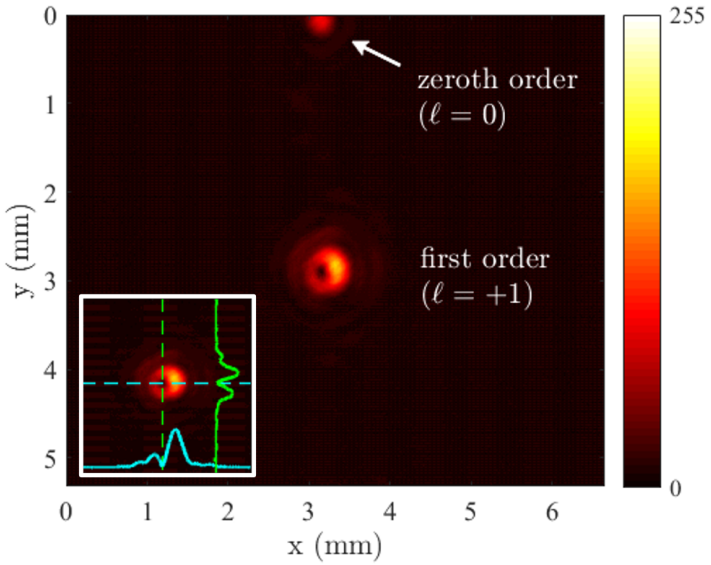

Source: The author (2021).

3.4 Signal detection and preliminary results

The FWM experiments were performed in the MOT described in this chapter, for two configurations: parallel and orthogonal polarizations of incident beams. For parallel polarizations, $\hat{\varepsilon}_a \parallel \hat{\varepsilon}_b$, the atom-light interaction can be described considering a two-level atomic system. With orthogonal beam polarizations, $\hat{\varepsilon}_a \perp \hat{\varepsilon}_b$, the nonlinear interaction can be described in terms of a 3- or a 4-level system, depending on the chosen quantization axis.

Regardless of the relative orientation of incident beam polarizations, after the signal generation inside the cold atom sample, all four beams, E_a, E_b (transmitted), S_1 and S_2 (generated), are sent to the detection part of the experiment, which is illustrated in figure 22. There is a small separation between the four beams due to the angle ϑ between the wave-vectors $\vec{k}_a$ and $\vec{k}_b$, that allows to send each beam to an individual detector. The efficiency of power conversion from incident to generated signals in our configuration is quite low. For this reason, we use avalanche photo detectors (APD) to detect the symmetric FWM signals. To capture images of the intensity profile of one of the two generated beams, we replace the APD with a CCD camera. The transmitted beams E_a and E_b are strong and can be detected with photodetectors.

For $\hat{\varepsilon}_a \parallel \hat{\varepsilon}_b$, both generated signals will possess the same polarization direction as the incident beams. On the other hand, for orthogonal polarizations of incident beams, the generated signals will also have orthogonal polarizations, $\hat{\varepsilon}_1 \perp \hat{\varepsilon}_2$. Also, they will satisfy $\hat{\varepsilon}_a \perp \hat{\varepsilon}_1$ and $\hat{\varepsilon}_b \perp \hat{\varepsilon}_2$. For this reason, it becomes easier to clean the signal going to each detector.

We show the lineshapes obtained for the two symmetric FWM signals in both incident beam polarization settings. For orthogonal linear polarizations, we also show the lineshapes when E_b carries topological charge. In this configuration we also show images of the transverse profile of the generated FWM signal S_1 when pumps have Gaussian

Figure 22 – Scheme for the detection of transmitted and generated signals in the FMW experiment.

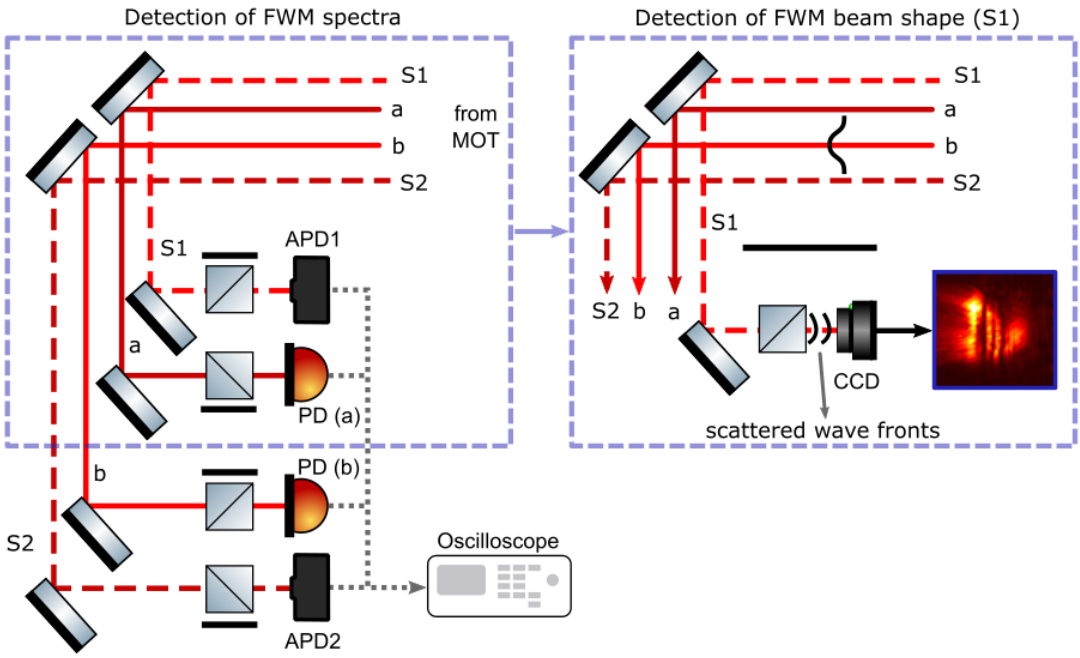

Source: The author (2021).

distributions.

3.4.1 FWM spectra

We show in figure 23 the intensities of both generated signals, S_1 and S_2, as a function of the detuning from resonance of incident beams in the $\hat{\varepsilon}_a \parallel \hat{\varepsilon}_b$ setting. It is seen that the spectra of both signals present power broadening and that their amplitudes do not saturate up to the higher beam intensity used in the measurements. The amplitudes of S_2 are smaller than the amplitudes of S_1 for all intensities because, as depicted in figure 22, S_2 is detected further in the optical table.

In figure 24 the intensities of the two symmetric signals, S_1 and S_2, as a function of the frequency detuning of incident beams are presented for $\hat{\varepsilon}_a \perp \hat{\varepsilon}_b$. We selected two powers of incident beams and varied the topological charge of beam E_b, which assumed the values $\ell_b = 0, 1, 2$. The signal with orthogonal polarizations was studied in a previous project [55] using only Gaussian beams. We can't precisely describe all of its characteristics, specially the central valley. It is seen that the features of the lineshape with $\ell_a = \ell_b = 0$ are maintained when $\ell_b \neq 0$. Also, we note that for increasing topological charge ℓ_b, the linewidths become narrower. This has already been addressed in other works, and occurs because of the intensity distribution of the LG beams [56]. In the following chapter we discuss this effect in a little more detail. Furthermore, this signal possesses greater linewidths for a similar range of incident beam power, in comparison with the signal obtained for parallel incident beam polarizations. We recall that in our setup, the FWM laser is not locked in frequency, instead, its frequency is swept continuously in the FWM time window. For a fixed sweep rate of the incident laser frequency, the nonlinear signal with a greater width in frequency also has a greater width in time. Since we estimate the generated signal intensities to be very low, the emission over a longer interval of time

Figure 23 – Measured FWM spectra of (a) S_1 $(2\vec{k}_a - \vec{k}_b)$ and (b) S_2 $(2\vec{k}_b - \vec{k}_a)$ obtained with Gaussian beams in the $(\hat{\varepsilon}_a \parallel \hat{\varepsilon}_b)$ configuration for different input intensities.

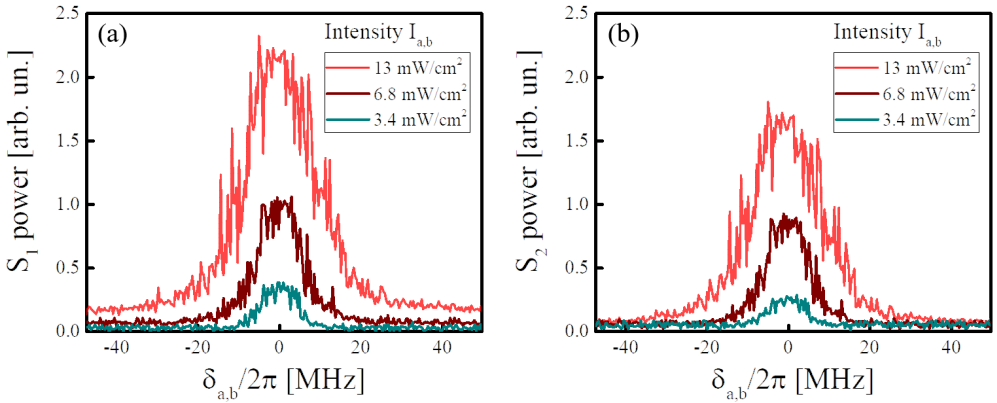

Source: The author (2021).

Figure 24 – Normalized FWM spectra of S_1 $(2\vec{k}_a - \vec{k}_b)$ and S_2 $(2\vec{k}_b - \vec{k}_a)$ for $\ell_a = 0$ and $\ell_b = 0, 1, 2$ in the $(\hat{\varepsilon}_a \perp \hat{\varepsilon}_b)$ configuration. Beam power is (a),(b) $P_{a,b} \approx 315$ μW and (c),(d) $P_{a,b} \approx 160$ μW. In (b) and (d) the curves corresponding to $\ell_b = 1, 2$ have been smoothed.

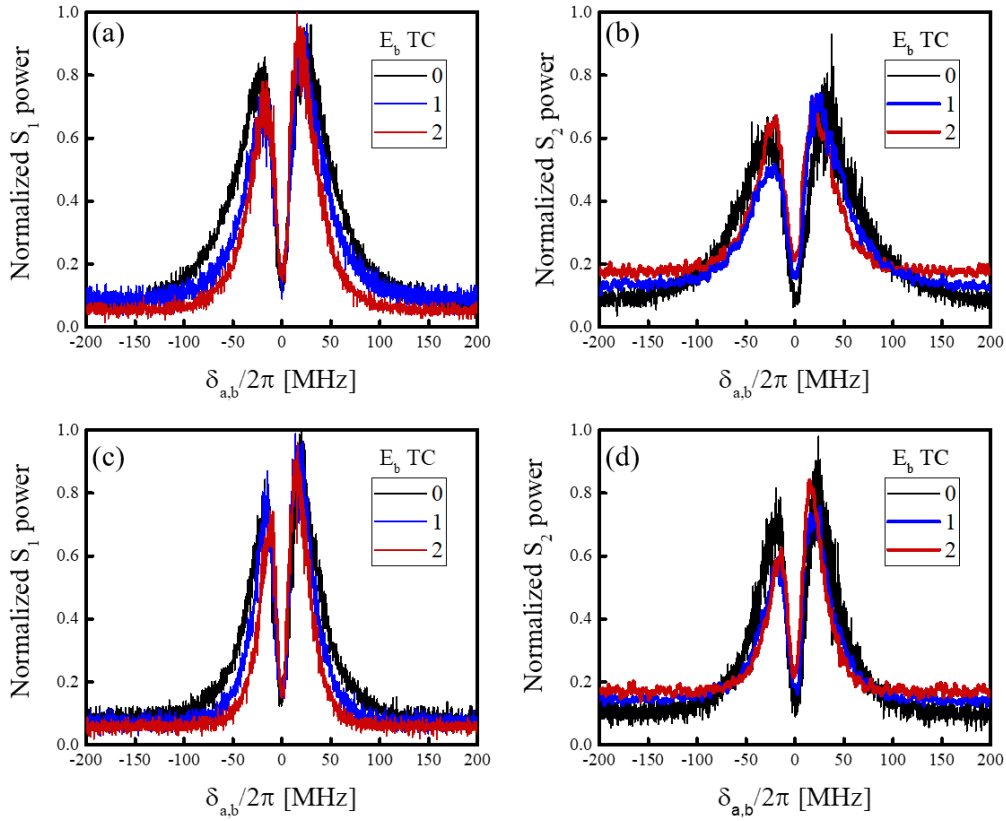

Source: The author (2021).

during the FWM time window may be easier do detect with a camera. This led us to choose the $\hat{\varepsilon}_a \perp \hat{\varepsilon}_b$ setting in the first attempts to detect the FWM beam profile. The following discussion considers this configuration.

3.4.2 FWM beam profile

Because of their high power, we expect the incident beams transmitted through the atomic medium to undergo little spatial variation as a result of the nonlinear interaction. Thus, we are mainly interest in the spatial profile of the weak FWM beams. One issue that posed some difficulty to capture clear images is that, even with $\hat{\varepsilon}_a \perp \hat{\varepsilon}_b$, and the possibility to clean each signal with polarizing beam splitters, scattered light was present with much more intensity than the FWM beam we were trying to see. In figure 22 we illustrate the wave fronts from beam E_b that arrive at the detection position of signal S_1. The obtained image contains a bright diffracted pattern that is almost completely from beam E_b. To have a better image of the generated beam, the following procedure was employed. With the camera aligned to capture S_1 fixed in position, we capture images in three conditions: (i) E_a not incident on the MOT, (ii) E_b not incident on the MOT, and (iii) E_a and E_b incident on the MOT, generating S_1. In this manner, image (iii) will show all possible scattered light from E_a and E_b in addition to the FWM signal. Images (i) and (ii) will show the scattered light from E_b and E_a, respectively. Each image can be represented by a $N_y \times N_x$ matrix, where N_x (N_y) is the number of pixels in the x (y) directions. The matrices $\mathbf{M}_1$, $\mathbf{M}_2$ and $\mathbf{M}_3$ contain the images corresponding to (i), (ii) and (iii), respectively. A clean image of the FWM beam profile is obtained with the matrix $|\mathbf{M}_3 - \mathbf{M}_1 - \mathbf{M}_2|$. Figure 25 illustrates the arrangement to capture these images and figure 26 we shows the sequence of images, respectively. We see that the clean

Figure 25 – Arrangement for the detection of images that correspond to matrices (a) $\mathbf{M}_1$, (b) $\mathbf{M}_2$ and (c) $\mathbf{M}_3$.

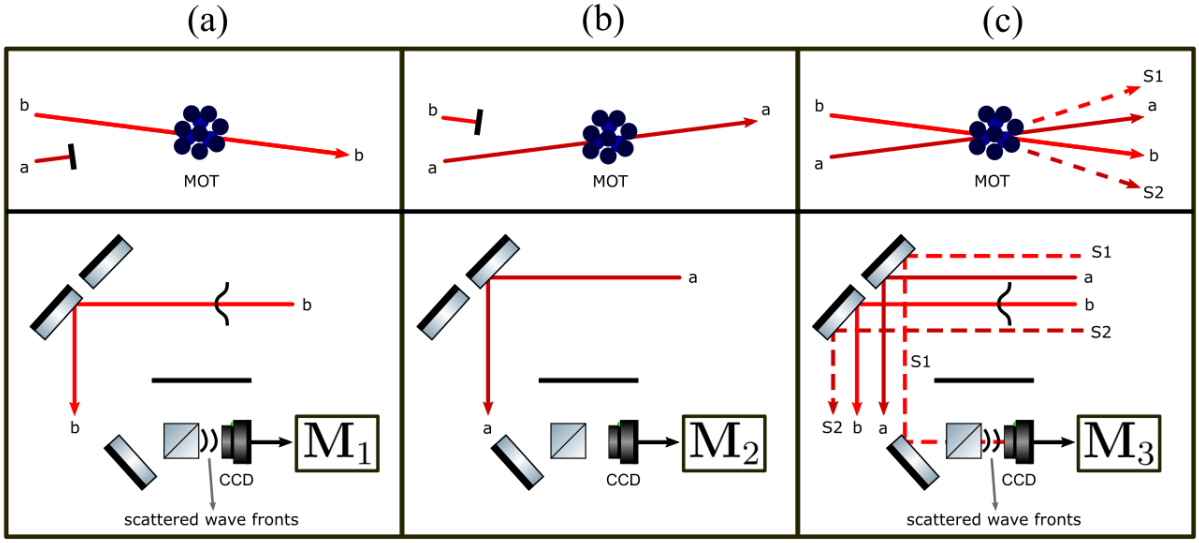

Source: The author (2021).

FWM beam profile image also presents a fringed pattern. This can be originated by the diffraction of the FWM beam or can be some residue from the scattered light from field E_b. Nonetheless, the profile appears to be Gaussian, with little ellipticity.

Figure 26 – Captured images showing (a) light scattered from E_b, (b) light scattered from E_a, (c) light scattered from both pumps and the FWM beam and (d) FWM beam profile. Inset shows zoomed FWM beam.

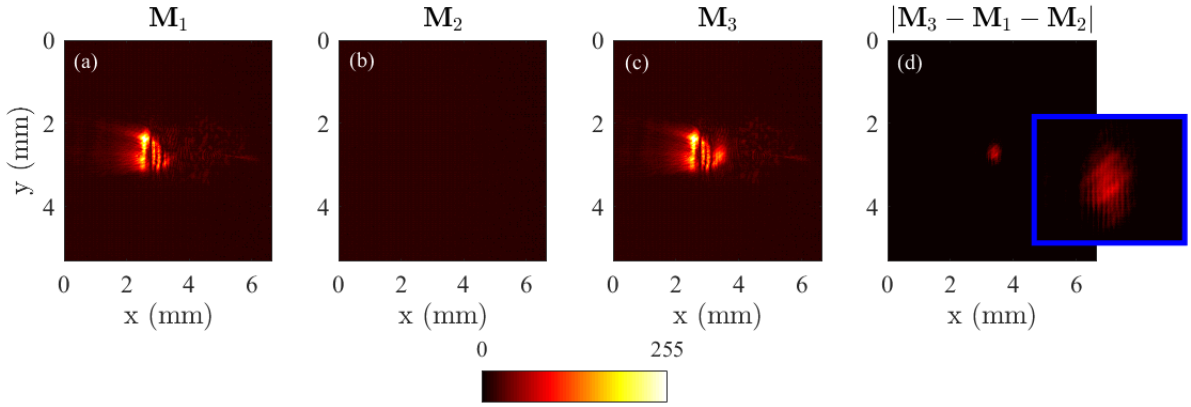

Source: The author (2021).

4 THE THEORETICAL MODEL

The theoretical model used to describe the generated FWM beam is divided in two main parts. The first one is the semi-classical description of the interaction between the atomic medium and the radiation field of the laser beam via optical Bloch's equations. In the second part, we solve the wave equation for the FWM field Ω_s with the source term given by the nonlinear polarization P_{NL}, related to the nonlinear coherence obtained in the first part.

4.1 Four-wave mixing in two-level atoms

We consider two input beams $\vec{E}_a$ and $\vec{E}_b$, with propagation directions $\vec{k}_a$ and $\vec{k}_b$, respectively. Two FWM signals are generated simultaneously in directions $(2\vec{k}_a - \vec{k}_b)$ and $(2\vec{k}_b - \vec{k}_a)$. We name these signals $(2\omega_a - \omega_b)$ or S_1 and $(2\omega_b - \omega_a)$ or S_2, respectively. We consider a quasi co-propagating configuration, where the angle ϑ between $\vec{k}_a$ and $\vec{k}_b$ is very small (figure 27a), making $\vec{k}_{a,b} \cdot \vec{r} \simeq k_{a,b} z$, where $k_\alpha = |\vec{k}_\alpha| = \omega_\alpha n_\alpha / c$ and n_α is the index of refraction at frequency ω_α, $\alpha \in \{a, b\}$.

The polarization directions $\hat{\varepsilon}_a$ and $\hat{\varepsilon}_b$ of input beams $\vec{E}_a$ and $\vec{E}_b$ determine the transitions that can be driven in the atomic system during the nonlinear process. We are interested in the case where $\hat{\varepsilon}_a$ and $\hat{\varepsilon}_b$ are parallel circular polarizations. In this case, we can model the atom as a two-level system. The nonlinear interaction leads to the generation of S_1 with the absorption of two photons from the E_a beam and the stimulated emission of one photon in the direction of E_b; and S_2 with the absorption of two photons from the E_b beam and the stimulated emission of one photon in the direction of E_a. These processes are schematically represented in figures 27b and 27c. In what follows we use the density matrix formalism detailed in Chapter 2. The starting point is the set of equations (2.16), that describe the time evolution of the density operator for a two-level system in the electric dipole approximation

$$\begin{aligned} (\dot{\Delta\rho}) &= -\frac{2i}{\hbar}\left[\rho_{12} H_{\mathrm{int},21} - \rho_{21} H_{\mathrm{int},12}\right] - \Gamma\left[(\Delta\rho) - (\Delta\rho)^0\right], \\ \dot{\rho}_{12} &= -\frac{i}{\hbar}\left[H_{\mathrm{int},12}(\Delta\rho) - \rho_{12}\left(\mathbb{E}_2 - \mathbb{E}_1\right)\right] - \frac{\Gamma}{2}\rho_{12}. \end{aligned} \tag{4.1}$$

Now, the total incident field is given by

$$\vec{E}(\vec{r}, t) = \sum_\alpha \vec{E}_\alpha(\vec{r}, t), \tag{4.2}$$

with $\alpha \in \{a, b\}$, and

$$\begin{aligned} \vec{E}_\alpha(\vec{r}, t) &= \hat{\varepsilon}_\alpha \mathcal{E}_\alpha(\vec{r})\, e^{-i\left(\vec{k}_\alpha \cdot \vec{r} - \omega_\alpha t\right)} + c.c., \\ &= \hat{\varepsilon}_\alpha E_\alpha(\vec{r}, t) + c.c. \end{aligned} \tag{4.3}$$

We define the Rabi frequency

$$\begin{aligned} \Omega_\alpha(\vec{r}) &= \frac{\mu_{12}^\alpha \mathcal{E}_\alpha(\vec{r})}{\hbar}, \\ &= \Omega_\alpha^0 u_\alpha(\vec{r}), \end{aligned} \tag{4.4}$$

Figure 27 – (a) Spatial distribution of the wave-vectors of the incident and generated beams and scheme of the transitions in a two-level system to generate (b) S_1 and (c) S_2.

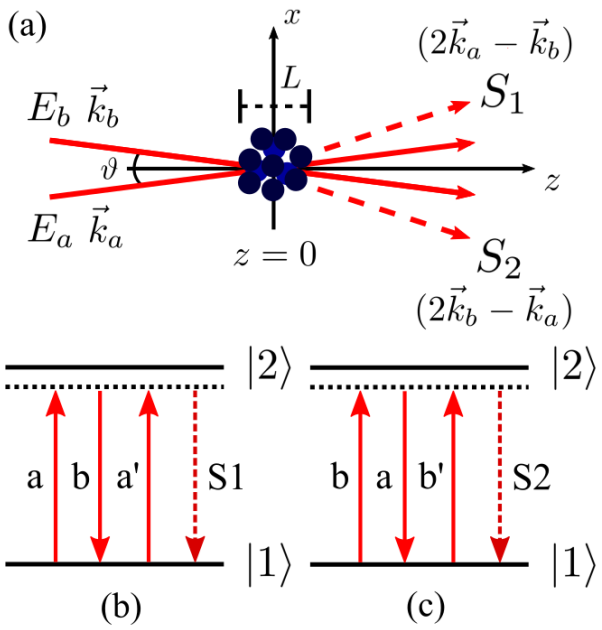

Source: The author (2021).

where $u_\alpha(\vec{r})$ is normalized to unity and $\mu_{12}^\alpha = \langle 1|\,(\boldsymbol{\mu}\cdot\hat{\varepsilon}_\alpha)\,|2\rangle$ ($\mu_{12}^a = \mu_{12}^b = \mu_{12}$). In the rotating wave approximation, the matrix elements of $\hat{H}_{\rm int}(t)$ are written

$$H_{{\rm int},12}(t) = -\hbar\Omega_a(\vec{r})e^{-i(k_a z-\omega_a t)} - \hbar\Omega_b(\vec{r})e^{-i(k_b z-\omega_b t)}. \tag{4.5}$$

We assume that the coherence ρ_{12} oscillates with frequencies ω_a, ω_b and $2\omega_a-\omega_b$ [10] and write

$$\rho_{12} = \sigma_{12}^a e^{i\omega_a t} + \sigma_{12}^b e^{i\omega_b t} + \sigma_{12}^{2a-b} e^{i(2\omega_a-\omega_b)t}. \tag{4.6}$$

The $2\omega_a-\omega_b$ component is responsible for the nonlinear mixing process that generates S_1. The population difference ($\Delta\rho$) has a stationary component and one oscillating at $|\omega_a-\omega_b|$, and is written as

$$(\Delta\rho) = (\Delta\rho)^{\rm dc} + \left[(\Delta\rho)^{a-b}e^{i(\omega_a-\omega_b)t} + c.c.\right]. \tag{4.7}$$

Substituting (4.5), (4.6) and (4.7) into equations (4.1), and collecting terms that oscillate

with the same frequency, in the steady state we arrive at the set of algebraic equations

$$(\Delta\rho)^{a-b} = \frac{2i\tilde{\Omega}_a^*\sigma_{12}^{2a-b} + 2i\tilde{\Omega}_b^*\sigma_{12}^{a} - 2i\tilde{\Omega}_a\sigma_{12}^{b*}}{(i\delta_a - i\delta_b + \Gamma)}, \tag{4.8}$$

$$(\Delta\rho)^{\mathrm{dc}} = (\Delta\rho)^0 + \frac{2i\Omega_a^*\sigma_{12}^{a} + 2i\Omega_b^*\sigma_{12}^{b} - 2i\Omega_a\sigma_{12}^{a*} - 2i\Omega_b\sigma_{12}^{b*}}{\Gamma}, \tag{4.9}$$

$$\sigma_{12}^{a} = \frac{i\tilde{\Omega}_a(\Delta\rho)^{\mathrm{dc}} + i\tilde{\Omega}_b(\Delta\rho)^{a-b}}{(i\delta_a + \Gamma/2)}, \tag{4.10}$$

$$\sigma_{12}^{b} = \frac{i\tilde{\Omega}_b(\Delta\rho)^{\mathrm{dc}} + i\tilde{\Omega}_a\left[(\Delta\rho)^{a-b}\right]^*}{(i\delta_b + \Gamma/2)}, \tag{4.11}$$

$$\sigma_{12}^{2a-b} = \frac{i\tilde{\Omega}_a(\Delta\rho)^{a-b}}{(2i\delta_a - i\delta_b + \Gamma/2)}, \tag{4.12}$$

where $\tilde{\Omega}_\alpha \equiv \Omega_\alpha e^{-ik_\alpha z}$, $\delta_\alpha \equiv \omega_\alpha - \omega_o$ is the detuning from resonance of field Ω_α and $\omega_o \equiv (\mathbb{E}_2 - \mathbb{E}_1)/\hbar$ is the resonance frequency. In the strong pump and weak probe regime, $\Omega_a \gg \Omega_b$, the full solution for all terms in (4.6) is given in Ref. [10]. We are interested, however, in a situation where both fields have similar intensities, $|\Omega_a| \sim |\Omega_b|$, and thus seek an expression to the nonlinear coherence that is affected somewhat similarly by Ω_a and Ω_b. With a direct substitution method, we solve for σ_{12}^{2a-b} to find

$$\sigma_{12}^{2a-b} = \frac{-2i\tilde{\Omega}_a^2\tilde{\Omega}_b^*(\Delta\rho)^{\mathrm{dc}}(1/\Delta_a + 1/\Delta_b)}{D(\delta_a,\delta_b)\,(2i\delta_a - i\delta_b + \Gamma/2) + 2|\Omega_a|^2}, \tag{4.13}$$

where $D(\delta_a,\delta_b) = i\delta_a - i\delta_b + \Gamma$, $\Delta_a = i\delta_a + \Gamma/2$, $\Delta_b = -i\delta_b + \Gamma/2$ and $(\Delta\rho)^{\mathrm{dc}}$ can be found as

$$(\Delta\rho)^{\mathrm{dc}} \simeq \frac{(\Delta\rho)^0}{1 + \dfrac{2|\Omega_a|^2}{\delta_a^2 + \Gamma^2/4} + \dfrac{2|\Omega_b|^2}{\delta_b^2 + \Gamma^2/4}}. \tag{4.14}$$

Figure 28a shows the lineshapes of σ_{12}^{2a-b} for $\Omega_a = \Omega_b$ with varying $\delta_a = \delta_b$, that represents the situation we are interested in. The spectra of the FWM signal contain a single peak at resonance, which is in agreement with our experimental results for this configuration. Figure 28b shows the amplitude of output signal at resonance as a function of $\Omega_{a,b}$. The linear coherences σ_{12}^{a} and σ_{12}^{b} are found as

$$\sigma_{12}^{a} = \frac{-i\tilde{\Omega}_a\rho_{11}^0}{i\delta_a + \Gamma/2 + 2|\Omega_a|^2/\Gamma + 2|\Omega_b|^2/\Delta_{a,b}}, \tag{4.15}$$

$$\sigma_{12}^{b} = \frac{-i\tilde{\Omega}_b\rho_{11}^0}{i\delta_b + \Gamma/2 + 2|\Omega_b|^2/\Gamma + 2|\Omega_a|^2/\Delta_{a,b}^*}, \tag{4.16}$$

where $\Delta_{a,b} = i\delta_a - i\delta_b + \Gamma/2$. Note that $\sigma_{12}^{a,b} = \sigma_{12}^{b,a}(a \leftrightarrow b)$. The nonlinear coherence given by equation (4.13) is related to the nonlinear susceptibility via [10]

$$\chi^{(3)} = \frac{\mathcal{N}|\mu_{12}|^4}{\varepsilon_o\hbar^3}\frac{\sigma_{12}^{2a-b}}{\tilde{\Omega}_a^2\tilde{\Omega}_b^*}, \tag{4.17}$$

where $\mathcal{N}$ is the atomic density. We write

$$\chi_{\mathrm{eff}}^{(3)} = \frac{-2i\mathcal{N}|\mu_{12}|^4(\Delta\rho)^{\mathrm{dc}}(1/\Delta_a + 1/\Delta_b)/\varepsilon_o\hbar^3}{D(\delta_a,\delta_b)\,(2i\delta_a - i\delta_b + \Gamma/2) + 2|\Omega_a|^2}, \tag{4.18}$$

Figure 28 – (a) Nonlinear signal power as a function of $\delta_a = \delta_b$ for some values of $\Omega_{a,b}$. (b) Amplitude of generated nonlinear signal at resonance as a function of input Rabi frequency. Maximum output is obtained for $\Omega_{a,b} = 0.64\Gamma$ (red dashed line). Inset shows the full width at half maximum (FWHM).

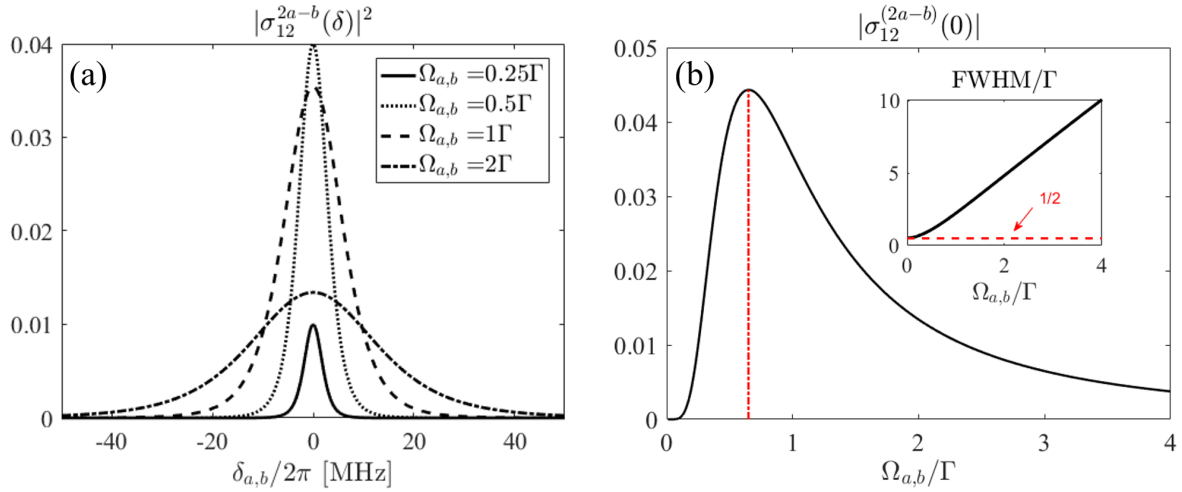

Source: The author (2021).

where the subscript indicates that this an effective susceptibility, that contains terms related to processes in the direction $(2\vec{k}_a - \vec{k}_b)$, but with higher orders of the fields. The coherence and susceptibility related to signal $(2\omega_b - \omega_a)$, with direction $(2\vec{k}_b - \vec{k}_a)$, have the same form as (4.13) and (4.18), respectively, with the exchange of labels $a \leftrightarrow b$. The total linear susceptibility is obtained by the sum of the contributions from the coherences oscillating at ω_a and ω_b,

$$\begin{aligned}\chi_{\text{eff}}^{(1)} &= \chi_{\text{eff},a}^{(1)} + \chi_{\text{eff},b}^{(1)}, \\ &= \frac{\mathcal{N}|\mu_{12}|^2}{\varepsilon_o \hbar}\left(\frac{\sigma_{12}^a}{\tilde{\Omega}_a} + \frac{\sigma_{12}^b}{\tilde{\Omega}_b}\right).\end{aligned} \tag{4.19}$$

Since our interest is primarily on FWM processes in a sample of cold (stationary) atoms, we need not to include the effect of Doppler broadening. The absorptive and dispersive responses, given by equation (4.19), are shown in figure 29. The information given by these results can aid the selection of an optimal value for $\Omega_{a,b}$.

4.2 Wave equation

We are interested in the intensity profile of the generated fields, and thus seek a solution to the wave equation for field $\vec{E}_s$. We focus only on S_1, since the equations for S_2 are obtained and solved in the same way. The wave equation for the FWM electric field is

$$\nabla^2 \vec{E}_s - \frac{1}{c^2}\frac{\partial^2 \vec{E}_s}{\partial t^2} = \mu_o \frac{\partial^2 \vec{P}}{\partial t^2}. \tag{4.20}$$

We project (4.20) onto $\hat{\varepsilon}_s^*$ to get the scalar equation

$$\nabla^2 E_s + \frac{\omega_s^2}{c^2} E_s = \mu_o \frac{\partial^2}{\partial t^2}(\vec{P} \cdot \hat{\varepsilon}_s^*). \tag{4.21}$$

Figure 29 – (a) Dispersive and (b) absorptive responses of the medium for the same values of Rabi frequency amplitudes as in figure 28.

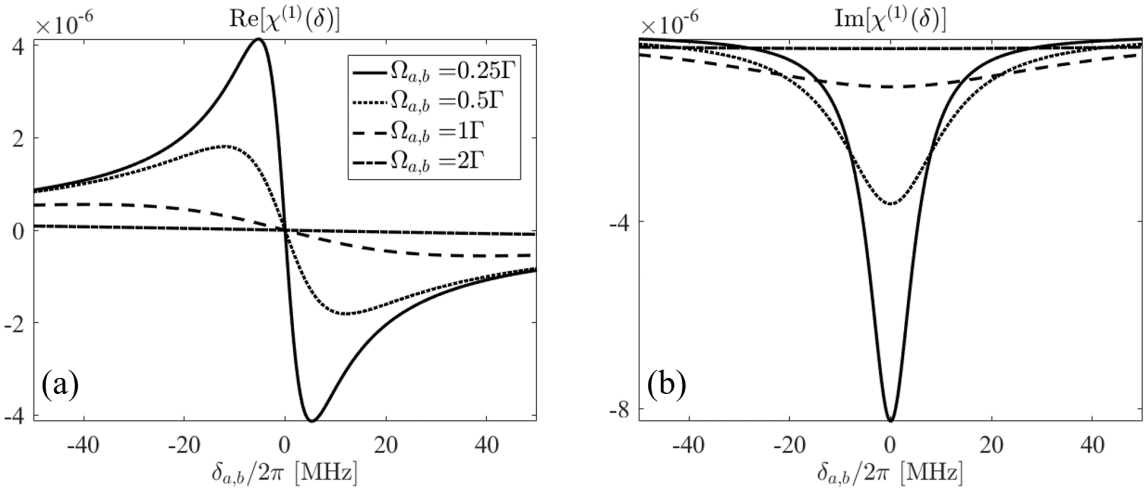

Source: The author (2021).

The total medium polarization is $\vec{P} = \vec{P}_{\rm L} + \vec{P}_{\rm NL}$ and its projection onto $\hat{\varepsilon}_s^*$ is

$$\begin{aligned}(\vec{P}\cdot\hat{\varepsilon}_s^*) &= P_{\rm L}(\omega_s) + P_{\rm NL}(\omega_s = 2\omega_a - \omega_b),\\ &= \varepsilon_o\chi_{\rm eff}^{(1)}E_s + \varepsilon_o\chi_{\rm eff}^{(3)}E_a^2E_b^*.\end{aligned} \tag{4.22}$$

Under the paraxial approximation we obtain the equation for the Rabi frequency Ω_s

$$\frac{i}{2k_s}\nabla_\perp^2\Omega_s + \frac{\partial\Omega_s}{\partial z} = -\alpha_{\rm lin}\Omega_s + \kappa\Omega_a^2\Omega_b^*e^{-i\Delta kz}, \tag{4.23}$$

where

$$\alpha_{\rm lin}(\vec{r};\delta) = -\frac{\omega_s}{2cn_s}{\rm Im}[\chi_{\rm eff}^{(1)}(\vec{r};\delta)], \tag{4.24}$$

$$\kappa(\vec{r};\delta) = -i\frac{\omega_s}{2cn_s}\frac{\hbar^2}{|\mu_{12}|^2}\chi_{\rm eff}^{(3)}(\vec{r};\delta) \tag{4.25}$$

are the linear absorption coefficient and the nonlinear coupling, and $\Delta k = |2\vec{k}_a - \vec{k}_b - \vec{k}_s|$ is the phase mismatch. Here, $n_s = (1 + {\rm Re}[\chi_{\rm eff}^{(1)}])^{1/2}$ is also spatially dependent. We use δ to represent both δ_a and δ_b. Note that the problem we are investigating has $(2+1)$ spatial dimensions and also the frequency degree of freedom. We highlight that, rigorously, both $\alpha_{\rm lin}$ and κ carry the spatial dependence of Ω_a and Ω_b.

The solution to (4.23) for incident plane waves was given in Chapter 2. For arbitrary nonuniform fields, this wave equation can be propagated numerically inside the nonlinear medium using a split-step Fourier method (SSFM), as in ref. [28]. In the following section we present a general solution method by expanding Ω_s in terms of LG modes. This will be done under the following considerations. Since the medium has a very small longitudinal extension L, we expect input fields, which are strong, to undergo little extinction and transverse structure variation along the interaction region. Thus, we treat (4.23) uncoupled from the wave equations for Ω_a and Ω_b. This simplifies the mathematical work of our problem and is shown to bring results with good agreement with experimental

measurements [27]. Also, to solve the wave equation, we'll set the frequencies of the fields at fixed values not far from resonance, and we'll assume $n_s \approx 1$ ($\mathrm{Re}\chi^{(1)}_{\mathrm{eff}} \approx 0$) at all positions.

4.3 FWM field in terms of LG modes

The orthogonality and completeness of the LG modes allow to write Ω_s as the superposition[1]

$$\Omega_s(\vec{r}) = \sum_{\ell,p} A_{\ell p}(z) u_{\ell p}(\vec{r}). \tag{4.26}$$

The problem becomes that of finding the coefficients. Substituting (4.26) into (4.23) we obtain

$$\sum_{\ell,p} \left(\frac{i\nabla_\perp^2}{2k_s} + \frac{\partial}{\partial z} \right) A_{\ell p}(z) u_{\ell p}(\vec{r}) = -\sum_{\ell,p} \alpha_{\mathrm{lin}} A_{\ell p}(z) u_{\ell p}(\vec{r}) + \kappa \Omega_a^2 \Omega_b^* e^{-i\Delta k z}. \tag{4.27}$$

Using the fact that $u_{\ell p}$ satisfies the homogeneous wave equation, and that the coefficients $A_{\ell p}$ have no dependence on the transverse coordinates,

$$\left(\frac{i\nabla_\perp^2}{2k_s} + \frac{\partial}{\partial z} \right) \begin{Bmatrix} u_{\ell p}(\vec{r}) \\ A_{\ell p}(z) \end{Bmatrix} = \begin{Bmatrix} 0 \\ \frac{\partial A_{\ell p}(z)}{\partial z} \end{Bmatrix}, \tag{4.28}$$

we arrive at

$$\sum_{\ell,p} u_{\ell p}(\vec{r}) \frac{\partial}{\partial z} A_{\ell p}(z) = -\sum_{\ell,p} \alpha_{\mathrm{lin}} A_{\ell p}(z) u_{\ell p}(\vec{r}) + \kappa \Omega_a^2 \Omega_b^* e^{-i\Delta k z}. \tag{4.29}$$

Multiplying both sides by $u^*_{\ell p}$ and integrating on the transverse plane, the orthogonality relation of the LG modes, given by equation (2.85), leads to the equation for $A_{\ell p}(z)$

$$\frac{\partial A_{\ell p}(z)}{\partial z} = -\alpha_p^\ell(z) A_{\ell p}(z) + \Lambda_p^\ell(z) e^{-i\Delta k z}. \tag{4.30}$$

In the above equation,

$$\alpha_p^\ell(z) = \iint \alpha_{\mathrm{lin}} |u_{\ell p}|^2 r dr d\phi \tag{4.31}$$

is the mode dependent absorption coefficient, a measure of how much each generated mode is affected by linear absorption; and

$$\Lambda_p^\ell(z) = \iint \kappa \Omega_a^2 \Omega_b^* u^*_{\ell p} r dr d\phi, \tag{4.32}$$

is the projection of the spatially dependent nonlinear source term onto the LG function space, called the transverse overlap integral. Consider $\Omega_a \propto u_{\ell_a p_a}$ and $\Omega_b \propto u_{\ell_b p_b}$. Since κ has no phase information from the incident fields, the azimuthal integral in (4.32),

$$\int_0^{2\pi} e^{-i(2\ell_a - \ell_b - \ell)\phi} d\phi = 2\pi \delta_{\ell, 2\ell_a - \ell_b}, \tag{4.33}$$

[1]The modes $u_{\ell p}$ used to expand Ω_s have the same (w_o, z_R) as the incident beams.

leads to the topological charge selection rule for S_1

$$\ell = 2\ell_a - \ell_b. \tag{4.34}$$

Thus, the generated beam will be composed only of modes with topological charge $\ell_1 = 2\ell_a - \ell_b$. Similarly, S_2 will only contain modes with $\ell_2 = 2\ell_b - \ell_a$. This is a statement of the conservation of OAM in the FWM process considered in this work.

Effects caused by the linear response are not our primary interest, and so we consider that the absorption coefficient α_{lin} can be taken as a spatially uniform quantity, α_0. In this case, we have $\alpha_p^\ell(z;\delta) = \alpha_0(\delta)$, which is independent of indices ℓ and p, and of the coordinate z. With this, equation (4.30) can be more easily solved. With the substitution $\tilde{A}_{\ell p}(z) = A_{\ell p}(z)e^{\alpha_0 z}$, we find

$$\frac{\partial \tilde{A}_{\ell p}(z)}{\partial z} = \Lambda_p^\ell(z)e^{-(i\Delta k - \alpha_0)z}. \tag{4.35}$$

We consider an interaction medium with extension L centered at the origin, such that the entry is located at $z = -L/2$ and the exit at $z = L/2$. In our problem, the generated field is not existent at the medium entry, and so the boundary condition is $\tilde{A}_{\ell p}(-L/2) = A_{\ell p}(-L/2) = 0$ for all (ℓ, p). We integrate on the longitudinal coordinate to find the full overlap integral

$$A_{\ell p}(z) = e^{-\alpha_0 z_<}\int_{-L/2}^{z_<} \Lambda_p^\ell(z')e^{-(i\Delta k - \alpha_0)z'}dz', \tag{4.36}$$

with $z_< = \min[z, L/2]$ because for $z > L/2$ there are no atoms to interact with the light fields, and $\Lambda_p^\ell(z) = \alpha_0 = 0$ in this region. The source term given by the nonlinear polarization P_{NL} drives the generation of the mixing signal until the position $z = L/2$, where the beam reaches the exit of the atomic medium and begins free propagation. We are interested in the FWM beam outside the medium, where it can be detected, and thus we seek to evaluate $A_{\ell p}(L/2)$. Note that, although not explicit, $A_{\ell p}(z)$ is also a function of $\delta_{a,b}$.

In the thick-medium regime, where we have $L \gg z_R$, the $u_{\ell p}$ modes that are generated with greater efficiency in the FWM process are those that satisfy the Gouy phase-matching (GPM) condition [18, 22], i.e., $(N_{\ell p})_s + (N_{\ell p})_b = 2(N_{\ell p})_a$ for the signal with direction $2\vec{k}_a - \vec{k}_b$, where $(N_{\ell p})_\alpha = 2p_\alpha + |\ell_\alpha|$ is defined as the mode number. We'll see how this requirement arises in Section 4.7. However, in the thin-medium regime, modes with good transverse overlap with the nonlinear source term, that posses high values of (4.32), can be generated, and the superposition (4.26) may contain modes that do not satisfy the GPM condition. Most of our calculations are performed considering a thin-medium, characterized by $L \ll z_R$. The variation of $\Lambda_p^\ell(z)$ in the interaction region is thus negligible, and we can approximate

$$\begin{aligned} A_{\ell p}(L/2) &\simeq \Lambda_p^\ell(0)e^{-\alpha_0 L/2}\int_{-L/2}^{L/2} e^{-(i\Delta k - \alpha_0)z'}dz', \\ &= \Lambda_p^\ell(0)\mathcal{T}(L;\Delta k, \alpha_0), \end{aligned} \tag{4.37}$$

where $\mathcal{T}$ can be regarded as an efficiency measure of the signal generation process inside the medium and is a common factor to all $A_{\ell p}$.

We see a very close resemblance between the solution (4.26), with the coefficients given by (4.37), and that given at the end of Chapter 2. When the phase mismatch is dominant, we get $|\mathcal{T}|^2 = \text{sinc}^2(\Delta k L/2)$. On the other hand, in a phase-matched condition,

we get $|\mathcal{T}|^2 = |(1 - e^{\alpha_0 L})/\alpha_0|^2$. Until this point, we have treated the solution to the wave equation in a fairly general manner. Throughout the rest of this work, we'll not concern ourselves with effects caused by the linear absorption and the phase-mismatch, and we'll take $\mathcal{T}(L; \Delta k, \alpha_0) = 1$.

The total power of Ω_s, P_s, as a function of the detuning from resonance, or the lineshape of Ω_s, is

$$P_s(\delta) = \iint |I_s(\vec{r}_\perp, z_d; \delta)|^2 r dr d\phi, \tag{4.38}$$

where $I_s = Z|\Omega_s|^2$ is the intensity distribution of the generated field, $Z = 2c\varepsilon_o\hbar^2/|\mu_{12}|^2$ and $z_d > L/2$ is the detection position. The constant Z factors out in all calculations involving the intensity distribution and the power of the beam, and thus we make $Z = 1$. The orthogonality of LG modes leads to

$$P_s(\delta) = \sum_{\ell,p} |A_{\ell p}(\delta)|^2, \tag{4.39}$$

which gives the normalization factor of Ω_s at fixed δ.

Using the intensity normalized FWM beam, $U_s \equiv \Omega_s/\sqrt{P_s}$, we define the mode fidelity or mode weight

$$\begin{aligned} \eta_{\ell p} &\equiv \left| \iint U_s u^*_{\ell p} r dr d\phi \right|^2, \\ &= \frac{|A_{\ell p}|^2}{P_s}, \end{aligned} \tag{4.40}$$

as a measure of the relative contribution of the mode $u_{\ell p}$ to Ω_s. The phase angle of $A_{\ell p}$ is $\Phi_{\ell p}$, such that

$$A_{\ell p} = \sqrt{P_s \eta_{\ell p}} e^{i\Phi_{\ell p}}, \tag{4.41}$$

and the relative phases between the various expansion coefficients can also be responsible for changes on the output beam superposition.

The coupling $\kappa(r, z; \delta) \propto \chi^{(3)}_{\text{eff}}(r, z; \delta)$ has a complicated dependence on the input fields, and, rigorously, on the position $\vec{r}$, but doesn't contribute substantially to the transverse shape of the far-field FWM beam, which is determined mainly by the product $\Omega_a^2 \Omega_b^*$. This suggests that the FWM beam profile is dictated by the overlap of input beams. Indeed, this is usually assumed in the description of nonlinear processes involving beams with OAM or arbitrary transverse structure.

In references [57, 58, 59], that focus on second order nonlinearities, the relevant susceptibility $\chi^{(2)}$ has no spatial dependence, and the quantity analogous to (4.32) that determines the SHG beam components is an overlap integral of three LG modes. In refs. [18, 22], that treat FWM processes in atomic vapours, the intensity profile of the generated blue light beam is successfully predicted by calculating overlap integrals of four LG modes, where $\chi^{(3)}$ is also regarded as a uniform quantity. In this manner, the medium quantities do not affect the expansion coefficients. With the present study, we seek to understand the influence of the atomic medium on the FWM process, more specifically, the role of the full spatial and spectral dependencies of $\chi^{(3)}_{\text{eff}}(\vec{r}; \delta)$ on the features of signals S_1 and S_2 in the particular FWM configuration considered.

In general, the FWM field expansion (4.26) contains multiple p orders, and the presence of modes with different $N_{\ell p} = (2p + |\ell|)$ can lead to the interference of the various Gouy phase factors $\exp\{i(1 + N_{\ell p}) \tan^{-1}(z/z_R)\}$ that affects the radial structure of $|\Omega_s|^2$ upon

propagation [60, 61]. We show that the combined spatial and spectral degrees of freedom of the nonlinear susceptibility can produce changes on the distributions of mode weights $\eta_{\ell_s p}$ and phases $\Phi_{\ell_s p}$, which in turn generate modifications of the free space propagation parameters of the FWM beams.

4.4 FWM lineshapes

Here we discuss the origin of the effect of the narrowing of FWM spectra that occurs when incident beams possess OAM. We first give a qualitative explanation only in terms of the intensity distributions of incident fields. Next, to evidence the narrowing, instead of the lineshape $P_s(\delta)$, that can be problematic in some cases, we calculate an averaged lineshape function that takes into account the spatial distributions of the incident fields.

We highlight that, as pointed in other works [56, 62], the vorticity of LG beams plays no role in this narrowing effect. Instead, the ring shaped intensity distribution, characteristic of LG beams, is responsible for this feature. This seems reasonable since $\chi^{(3)}_{\text{eff}}$, that carries the frequency response of the medium, has no dependence on the phases of the incident beams, only on their intensity distributions, as seen from equation (4.18). Now we picture the FWM process in two situations: both incident beams E_a and E_b with Gaussian distributions; and E_a with Gaussian and E_b with Laguerre-Gaussian distributions. In both cases, we consider beams with equal power. Figure 30 shows the beam radial profiles in both configurations, with $\ell_b = 1$ and 2. Due to the central valley of the LG beam,

Figure 30 – Representation of the spatial overlap of the incident beams involved in the FWM process when E_a is Gaussian and E_b has Gaussian and LG distributions with $\ell_b = 1$ and 2.

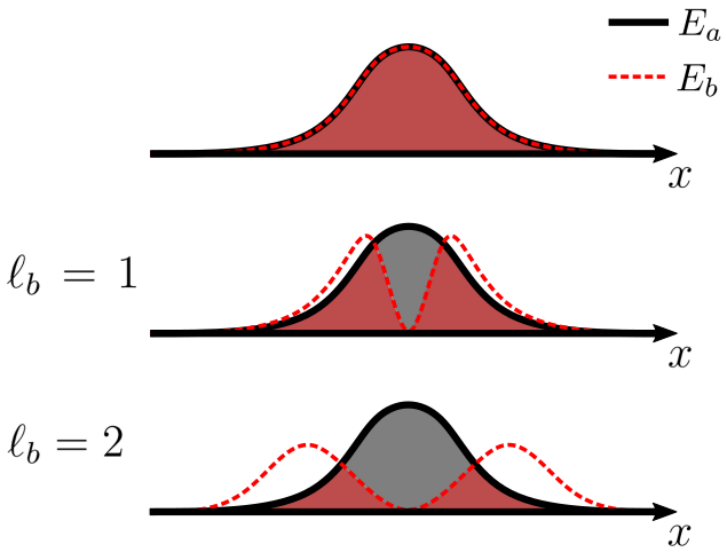

Source: The author (2021).

the red shaded area, that represents the spatial overlap of the beams, is greater when E_b is Gaussian and decreases for increasing ℓ_b. Thus, the region where the incident fields effectively interact to generate the nonlinear signal becomes smaller when beam E_b carries greater ℓ_b values. This can be seen as a loss of efficiency in the conversion of power from incident to generated beams, as ℓ_b increases. When measuring the power spectra of the FWM process with E_b given by an LG beam, the output power at all detuning values

Figure 31 – Normalized nonlinear signal power, calculated by averaging $\sigma_{12}^{2a-b}(\vec{r};\delta)$ over the interaction region $\mathcal{V}$, as a function of $\delta_{a,b}$ (equation 4.42) for three values of the topological charge of field E_b, $\ell_b = 0, 1$ and 2, and two incident Rabi frequency amplitudes $\Omega_{a,b}^0 = \Gamma$ and 2Γ.

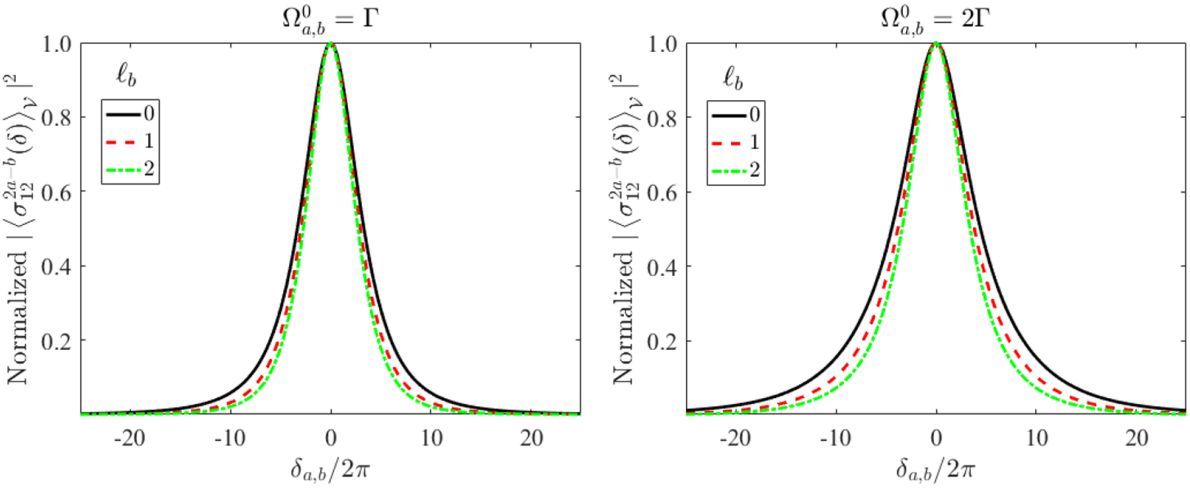

Source: The author (2021).

will be lower than when both beams are Gaussian. As a result, the lineshapes become narrower, compared to those obtained with incident Gaussian beams.

This intuitive explanation in terms of the incident fields alone is useful, but now we attempt to quantify the lineshapes by taking into account the full spatial dependence of the nonlinear susceptibility generated in the medium as a result of the interaction. With this objective, we define the averaged nonlinear coherence over the interaction volume $\mathcal{V}$,

$$\langle\sigma_{12}^{2a-b}(\delta)\rangle_{\mathcal{V}} = \frac{1}{\mathcal{V}}\iiint_{\mathcal{V}}\sigma_{12}^{2a-b}(\vec{r};\delta)dV. \tag{4.42}$$

The spatially uniform susceptibility associated with this quantity is defined as

$$\overline{\chi}_{\text{eff}}^{(3)}(\delta) = \frac{\mathcal{N}|\mu_{12}|^4}{\varepsilon_o\hbar^3}\frac{\langle\sigma_{12}^{2a-b}(\delta)\rangle_{\mathcal{V}}}{(\Omega_a^0)^2(\Omega_b^0)^*}. \tag{4.43}$$

The lineshapes obtained by calculating (4.42) considering E_a Gaussian and E_b Laguerre-Gaussian are shown in figure 31. We see that they become narrower for increasing topological charges ℓ_b. Also, note that the lineshapes considering only Gaussian beams of Fig. 31 (black curves) are narrower than those obtained considering plane waves (figure 28a) with the same Rabi frequency amplitudes. This suggests that Gaussian shaped beams promote a less efficient FWM process than beams with uniform spatial distributions.

4.5 Longitudinal parameters of the FWM beam

The spot size of an arbitrary beam with cylindrical symmetry is well described by $r_{\text{rms}}(z) = [\frac{1}{P}\iint r^2 I(\vec{r})rdrd\phi]^{\frac{1}{2}}$, where $I(\vec{r})$ is the intensity distribution and P is the total power in the beam. For a single LG mode $u_{\ell p}$, an exact result is found [63]

$$r_{\text{rms},\ell p}(z) = w(z)\sqrt{\frac{2p+|\ell|+1}{2}}, \tag{4.44}$$

where $w(z) = w_o\sqrt{1+(z/z_R)^2}$. For a Gaussian beam, we get $r_{\mathrm{rms},00}(z) = w(z)/\sqrt{2}$. For Ω_s, a superposition of LG modes, at $z > L/2$, we obtain

$$r_{\mathrm{rms}}(z) = \left[\iint r^2 |U_s(\vec{r}_\perp, z)|^2 r dr d\phi\right]^{\frac{1}{2}}. \tag{4.45}$$

Using (4.26), it's possible to arrive at [64]

$$r_{\mathrm{rms}}(z) = \frac{w(z)}{\sqrt{2}}\left[1 + \langle N\rangle - \xi(z)\right]^{\frac{1}{2}}, \tag{4.46}$$

where

$$\langle N\rangle = \sum_{\ell,p} \eta_{\ell p} N_{\ell p} \tag{4.47}$$

is the mean value of the mode number $N_{\ell p} = 2p + |\ell|$ in the superposition and

$$\begin{aligned} \xi(z) &= \mathrm{Re}\{\varphi e^{2i\tan^{-1}(z/z_R)}\}, \\ \varphi &= \frac{1}{P_s}\sum_{\ell,p>0} 2A_{\ell p}A^*_{\ell,p-1}\sqrt{p(p+|\ell|)} \end{aligned} \tag{4.48}$$

carries the contribution of the various Gouy phase factors. The divergence angle is another important beam parameter and in the paraxial regime can be defined as $\theta_{\mathrm{rms}} \equiv \lim_{z\to\infty} r_{\mathrm{rms}}(z)/z$. From (4.46), we find

$$\theta_{\mathrm{rms}} = \frac{w_o}{\sqrt{2}z_R}\left[1 + \langle N\rangle + \mathrm{Re}\{\varphi\}\right]^{\frac{1}{2}}. \tag{4.49}$$

It is useful to cast (4.46) in the form [64]

$$r_{\mathrm{rms}}(z) = \sqrt{r_m^2 + \theta^2_{\mathrm{rms}}(z-z_m)^2}, \tag{4.50}$$

where, with $a = 1 + \langle N\rangle$,

$$r_m^2 = \frac{w_o^2}{2}\frac{a^2 - |\varphi|^2}{a + \mathrm{Re}\{\varphi\}}, \tag{4.51}$$

$$z_m = -z_R\frac{\mathrm{Im}\{\varphi\}}{a + \mathrm{Re}\{\varphi\}}, \tag{4.52}$$

are the minimum spot size (squared) and the z position where it occurs, respectively. Figure 32 shows the geometrical representation of these quantities. We use these quantities to obtain the beam quality factor, given by

$$M^2 = \frac{2\pi\theta_{\mathrm{rms}} r_m}{\lambda}, \tag{4.53}$$

that describes how close to "pure Gaussian" a beam is. For a pure Gaussian beam, M^2 is equal to 1. For beams that deviate from a pure Gaussian beam, M^2 is greater than 1. Note that $\langle N\rangle$, φ, and consequently, θ_{rms}, r_m, z_m and M^2 depend on $\delta_{a,b}$ and on the field amplitudes $\Omega^0_{a,b}$. In order to highlight that this dependence arises in the theory due to the spatial distribution of $\chi^{(3)}_{\mathrm{eff}}(r,z;\delta)$, we consider the averaged nonlinear coupling $\overline{\kappa}(\delta) \propto \overline{\chi}^{(3)}_{\mathrm{eff}}(\delta)$. In this case it is straightforward to show that (4.45) does not vary with $\delta_{a,b}$ nor with $\Omega^0_{a,b}$.

Figure 32 – Longitudinal profile and parameters of the superposition of LG modes Ω_s.

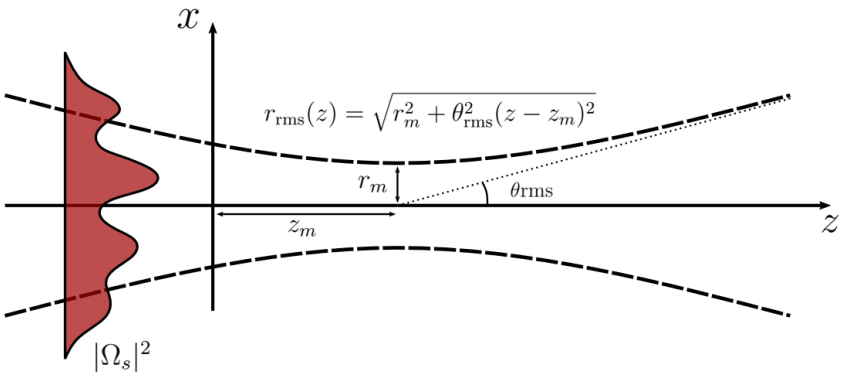

Source: Based on [64].

4.6 Arbitrary incident beams

We have discussed general aspects of the FWM beam solution when the incident fields are given by pure LG modes. An interesting situation is when the incident beams are described by general superpositions of LG modes. The modifications are straightforward. Consider

$$\begin{aligned} \Omega_a &= \Omega_a^0 \sum_{l,q} c_{lq} u_{lq}, \\ \Omega_b &= \Omega_b^0 \sum_{m,n} d_{mn} u_{mn}, \end{aligned} \tag{4.54}$$

where the coefficients satisfy $\sum_{l,q} |c_{lq}|^2 = 1$ and $\sum_{m,n} |d_{mn}|^2 = 1$. For the case that we are studying, the FWM process that generates a signal in direction $2\vec{k}_a - \vec{k}_b$, the generated field expansion coefficients become

$$\begin{aligned} A_{\ell p} &= \Omega^0 \sum_{lq} \sum_{l'q'} \sum_{mn} K_{qq'n}^{ll'm} \left[\int_{-L/2}^{L/2} \Lambda_{qq'np}^{ll'm\ell}(z) dz \right], \\ &= \Omega^0 \sum_{lq} \sum_{l'q'} \sum_{mn} K_{qq'n}^{ll'm} A_{qq'np}^{ll'm\ell}, \end{aligned} \tag{4.55}$$

where $\Omega^0 = (\Omega_a^0)^2 (\Omega_b^0)^*$, $K_{qq'n}^{ll'm} = c_{lq} c_{l'q'} d_{mn}^*$, the summations are performed over all indices contained in superpositions (4.54) and the transverse integral with extra indices is

$$\Lambda_{qq'np}^{ll'm\ell}(z) = \iint \kappa u_{lq} u_{l'q'} u_{mn}^* u_{\ell p}^* r dr d\phi. \tag{4.56}$$

As before, the azimuthal integral leads to the topological charge selection rule. We see that all modes that compose the output field must possess ℓ orders that satisfy

$$\ell = l + l' - m. \tag{4.57}$$

4.7 Analytical overlap integral and Gouy phase-matching

In general, it is not possible to find an analytical expression to the full overlap integral. It is, however, possible to do so when the spatial distribution of $\chi_{\rm eff}^{(3)}$ is neglected. Although we are mainly interested in the effects caused by the full spatial dependence of the

nonlinear susceptibility, it is important to understand the conditions imposed in the case where the nonlinear medium simply allows the FWM process to take place. Considering the spatially uniform susceptibility $\overline{\chi}^{(3)}_{\text{eff}}$, the coupling $\overline{\kappa}(\delta) \propto \overline{\chi}^{(3)}_{\text{eff}}(\delta)$ factors out of (4.32), which then becomes the overlap integral of four LG modes, as in references [18, 22]. The FWM field can be written as $\Omega_s = \overline{\kappa}(\delta)\mathcal{U}(\vec{r})$, the spatial and spectral degrees of freedom are thus completely separated and the result from Chapter 2, that the FWM signal power is proportional to the square of the nonlinear susceptibility, $P_s(\delta) \propto |\overline{\chi}^{(3)}_{\text{eff}}(\delta)|^2$, is recovered. Also, in this case, the spectral degrees of freedom do not affect the distribution of normalized coefficients $\eta_{\ell p} = |A_{\ell p}|/\sqrt{P_s}$ and phases $\Phi_{\ell p}$. Using the full expression of the LG modes, we can separate the z dependence of the transverse integral as[2]

$$\begin{aligned}\Lambda^{ll'm\ell}_{qq'np}(z) &= \Lambda^{ll'm\ell}_{qq'np}(0)\frac{e^{-i2Q\tan^{-1}(z/z_R)}}{1+(z/z_R)^2},\\ &= \Lambda^{ll'm\ell}_{qq'np}(0) f_Q(z),\end{aligned} \tag{4.58}$$

with

$$\begin{aligned}Q &= p+n-q-q'+\frac{1}{2}(|\ell|+|m|-|l|-|l'|),\\ &= \frac{1}{2}(N_{\ell p}+N_{mn}-N_{lq}-N_{l'q'}),\end{aligned} \tag{4.59}$$

and

$$\begin{aligned}\Lambda^{ll'm\ell}_{qq'np}(0) =& \frac{\overline{\kappa}}{2w_o^2}\mathcal{C}^{ll'm\ell}_{qq'np}\left[\int_0^\infty \rho^{|l|+|l'|+|m|+|\ell|} L_q^{|l|}(\rho^2)L_{q'}^{|l'|}(\rho^2)L_n^{|m|}(\rho^2)L_p^{|\ell|}(\rho^2)e^{-2\rho^2}\rho d\rho\right]\\ &\times\int_0^{2\pi} e^{-i(l+l'-m-\ell)\phi}d\phi,\\ =& \frac{\overline{\kappa}\pi}{w_o^2}\mathcal{C}^{ll'm\ell}_{qq'np}\mathcal{R}^{ll'm\ell}_{qq'np}\delta_{\ell,l+l'-m},\end{aligned} \tag{4.60}$$

where $\rho = \sqrt{2}r/w(z)$ and $\mathcal{C}^{ll'm\ell}_{qq'np} = C_{lq}C_{l'q'}C_{mn}C_{\ell p}$ is the product of LG normalization constants. The azimuthal integral ensures the topological charge selection rule, $\ell = l+l'-m$. Note that this makes Q an integer. The radial integral $\mathcal{R}^{ll'm\ell}_{qq'np}$ can be calculated using the series expansion of the associated Laguerre polynomials $L_p^{|\ell|}(x) = \sum_{k=0}^{p} c_k^{p|\ell|}x^k$, where $c_k^{p|\ell|} = \frac{(-1)^k}{k!}\frac{(p+|\ell|)!}{(|\ell|+k)!\,(p-k)!}$. It is possible to arrive at the general expression

$$\mathcal{R}^{ll'm\ell}_{qq'np} = \frac{1}{2}\sum_{k_1k_2}^{qq'}\sum_{k_3k_4}^{np} c_{k_1}^{q|l|}c_{k_2}^{q'|l'|}c_{k_3}^{n|m|}c_{k_4}^{p|\ell|}\Gamma(G+1)2^{-G-1}, \tag{4.61}$$

where $\Gamma(\cdot)$ is the Gamma function and $G = (|l|+|l'|+|m|+|\ell|)/2+k_1+k_2+k_3+k_4$. The full overlap integral over the medium extension L is

$$\begin{aligned}A^{ll'm\ell}_{qq'np}(L/2) &= \Lambda^{ll'm\ell}_{qq'np}(0)\int_{-L/2}^{L/2} f_Q(z)dz,\\ &= \Lambda^{ll'm\ell}_{qq'np}(0) I_Q(L).\end{aligned} \tag{4.62}$$

[2]Since k and z_R are the same for all modes inside the integral, the phases $\exp[-ikr^2/2R(z)]$, related to the curvature radius, cancel out.

The z integral over the extension of the interaction region,

$$I_Q(L) = \int_{-L/2}^{L/2} \frac{1}{1+(z/z_R)^2} \left(\frac{1 - iz/z_R}{1 + iz/z_R} \right)^Q dz, \tag{4.63}$$

is not relevant in a thin medium, where $I_Q(L) \approx L$ for all Q values. On the other hand, when the medium length L is comparable to z_R, it may lead to significant differences. Note that Q can be null, and in this case

$$\begin{aligned} I_0(L) &= \int_{-L/2}^{L/2} \frac{dz}{1+(z/z_R)^2}, \\ &= 2z_R \tan^{-1}\left(\frac{L}{2z_R}\right). \end{aligned} \tag{4.64}$$

On the other hand, if $Q \neq 0$, it is possible to find

$$I_Q(L) = \frac{iz_R}{2Q}\left(w_L^Q - w_L^{-Q}\right), \tag{4.65}$$

where

$$w_L = \frac{i + L/2z_R}{i - L/2z_R}. \tag{4.66}$$

In the thick medium limit, $L/z_R \to \infty$ and

$$I_Q \to \begin{cases} \pi z_R & , \ Q = 0, \\ 0 & , \ Q \neq 0. \end{cases} \tag{4.67}$$

We conclude that the only modes that survive the mixing process in a thick medium are those that satisfy $Q = 0$, or equivalently,

$$N_{\ell p} + N_{mn} = N_{lq} + N_{l'q'}, \tag{4.68}$$

which is the Gouy phase-matching condition [22]. Figure 33 shows the behaviour of $f_Q(z)$ and $I_Q(L)$ for different Q values. The imaginary part of f_Q is an odd function of z for integer Q.

Figure 34 shows the values of $\eta_{\ell p}$, for $\Omega_a = u_{01}$ and $\Omega_b = u_{00}$, calculated using the analytical overlap integral (4.62), and numerically integrating the product of four LG modes over the interaction volume for different ratios L/z_R. We see good agreement between the numerical and analytical values obtained for the mode fidelity. Furthermore, the radial mode selection due to the Gouy phase-matching becomes evident as L/z_R increases. The only mode that is generated for higher L/z_R values is u_{02}.

4.8 Suppression in a thick medium

We now use the results of the previous section to discuss the possibility of the supression of either of S_1 or S_2 in a thick medium due to the Gouy phase matching requirement. Considering that one of the beams is Gaussian, $\Omega_b = u_{00}$, and the other beam is a superposition of two LG modes with null radial indices and topological charges 1 and m, $\Omega_a = \Phi_m$, where

$$\Phi_m = \frac{u_{10} - u_{m0}}{\sqrt{2}}. \tag{4.69}$$

Figure 33 – Longitudinal function $f_Q(z)$ and its integral $I_Q(L)$ over the medium extension L for different values of Q. For a thick medium, only $I_0(L)$ has a significant value.

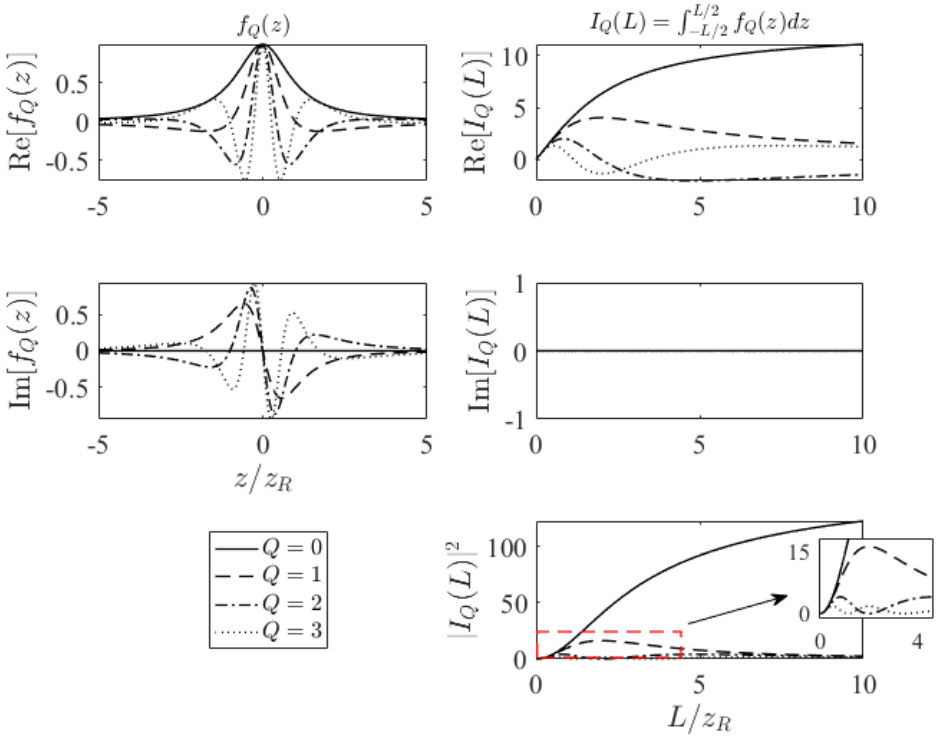

Source: The author (2021).

Figure 34 – Analytical and numerical values of the FWM field mode fidelity $\eta_{\ell p}$ for incident fields $\Omega_a = u_{01}$, $\Omega_b = u_{00}$ and different ratios L/z_R. Mode selection due to the Gouy phase-matching occurs for increasing L/z_R.

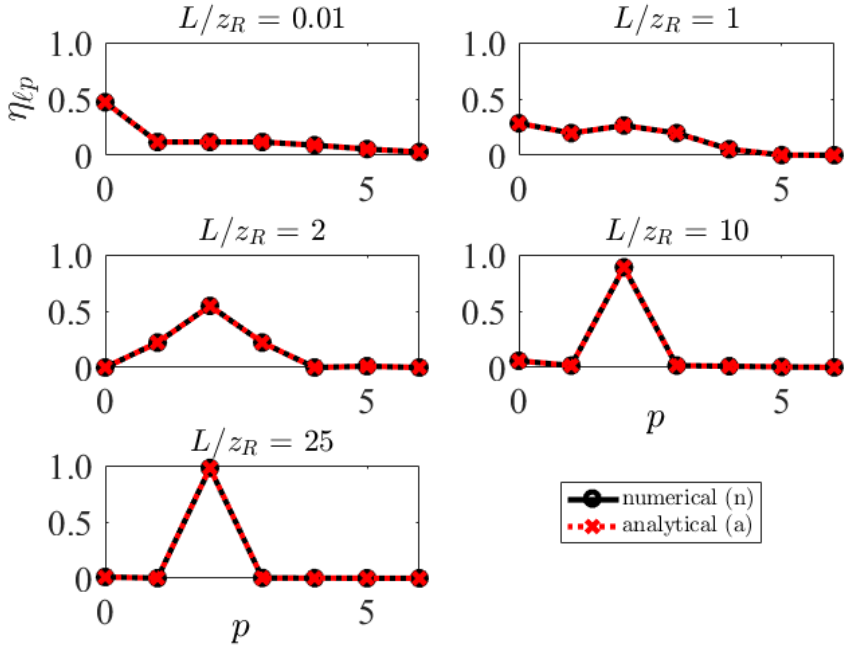

Source: The author (2021).

Figure 35 shows the transverse profile of Φ_m at $z = 0$ for different integers m. In this case, the transverse integral for field S_1, $(2\omega_a - \omega_b)$, becomes

$$\Lambda_p^{\ell}(0) = \frac{1}{2}\Lambda_{000p}^{110\ell}(0) - \Lambda_{000p}^{1m0\ell}(0) + \frac{1}{2}\Lambda_{000p}^{mm0\ell}(0) \tag{4.70}$$

and we see that the topological charges in the output superposition are $\ell = 2, 2m, 1+m$. Taking into account the z dependence and integrating over the medium extension, we get

$$A_{\ell p}^{(1)} = \frac{1}{2}\left[\delta_{\ell,2}\Lambda_{000p}^{110\ell}(0) + \delta_{\ell,2m}\Lambda_{000p}^{mm0\ell}(0)\right] I_p(L) - \delta_{\ell,(1+m)}\Lambda_{000p}^{1m0\ell}(0) I_{p+(|1+m|-|m|-1)/2}(L), \tag{4.71}$$

Here we consider the limiting case $L/z_R \to \infty$, and thus the generated signal will be composed only of modes with $p = 0$ or S, where $S = (1 + |m| - |1+m|)/2 \geq 0$. We write

$$A_{\ell p}^{(1)} = \frac{1}{2}\left[\delta_{\ell,2}\Lambda_{000p}^{110\ell}(0) + \delta_{\ell,2m}\Lambda_{000p}^{mm0\ell}(0)\right] \delta_{p,0} I_p(L) - \delta_{\ell,(1+m)}\Lambda_{000p}^{1m0\ell}(0)\delta_{p,S} I_{p-S}(L). \tag{4.72}$$

Similarly, for S_2, $(2\omega_b - \omega_a)$, we can find

$$A_{\ell p}^{(2)} = \frac{1}{\sqrt{2}}\delta_{\ell,-1}\Lambda_{000p}^{001\ell}(0)\delta_{p,-1} I_{p+1}(L) - \frac{1}{\sqrt{2}}\delta_{\ell,-m}\Lambda_{000p}^{00m\ell}(0)\delta_{p,-|m|} I_{p+|m|}(L). \tag{4.73}$$

However, since $p \geq 0$ is required, in the thick medium limit the generation of signal S_2 is suppressed. The above steps can be readily modified for the case where Ω_a is given by a more general composition of two LG modes.

Figure 35 – Intensity and phase distributions of Φ_m at $z = 0$ for $m = -2, -1, 0, 3$ and 4.

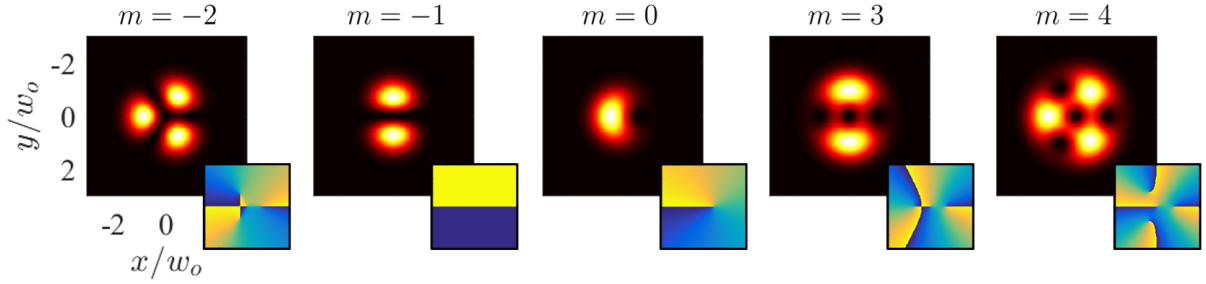

Source: The author (2021).

5 RESULTS

In this chapter we present and discuss our main results. Together, they comprise a theoretical investigation of various aspects of the FWM signal generation and free space propagation after leaving the nonlinear medium.

Our calculations consist of evaluating the expansion coefficient $A_{\ell p}$ for the two symmetric signals S_1 and S_2. With the set $\{A_{\ell p}\}$, all of the quantities we are interested in can be obtained, such as the intensity distribution $|\Omega_s|^2$ and its propagation outside the medium, the mode components $\eta_{\ell_s p}$, and others. We do this for a number of configurations. Here, one configuration is defined by the superpositions of LG modes that determine the shapes of $\Omega_a(\vec{r})$ and $\Omega_b(\vec{r})$, the amplitudes Ω_a^0 and Ω_b^0 that determine the total power of the incident beams, and the detunings from resonance δ_a and δ_b,

In our calculations, all beams possess the same wavelength λ and minimum waist w_o, giving the same Rayleigh range z_R. Also, a field with amplitude $\mathcal{E}_0$ described by $u_{\ell p}$, equation (2.78), will be taken as proportional to $\varpi \mathcal{E}_0 u_{\ell p}$, where factor ϖ ensures that this field will possess the same power as a plane wave with the same amplitude. For this condition to hold, we must have $\varpi = \sqrt{A_t}$, where A_t is the transverse area of the spatially uniform beam. For a circular beam of radius $w_{\rm pw}$, $A_t = \pi w_{\rm pw}^2$. It is reasonable to take $w_{\rm pw} = w_o$, and thus $\varpi = \sqrt{\pi} w_o$ is used in this work.

Recalling Chapter 3, all beams in our setup possess $w_o \approx 1$ mm near the MOT region. For the wavelength $\lambda = 780$ nm, the Rayleigh range is $z_R = \pi w_o^2/\lambda \approx 4$ m. The size of the cold atom cloud we usually obtain with our MOT is $L \approx 3 - 4$ mm. The condition $L/z_R \ll 1$ is satisfied and, for the most part, we focus on the thin medium regime. For this reason, we mainly use equation (4.37) to calculate the expansion coefficients. In the thick medium regime, $L \gg z_R$, a situation more easily achievable in a Rb vapor cell, we discuss the suppression of one of the symmetric signals due to the Gouy phase-matching condition.

For Gaussian inputs, the transverse shapes of the FWM beams are mainly Gaussian, and we show how free space propagation is affected by the detunings δ_a and δ_b. In the case of input beams with OAM, we show that the generated beams comply with the OAM conservation condition and obtain differences in the free space propagation between S_1 and S_2 that arise due to the spatial distributions of fields E_a and E_b. The phase discontinuities of LG beams reveal that by setting the detunings of incident beams off resonance, the phase distribution of the nonlinear coherence is rotated and distorted, similar to what is reported in other works.

5.1 Gaussian beams

For Gaussian input beams ($\ell_a = \ell_b = 0$) with equal intensities and detunings $\delta_a = \delta_b = \delta$, S_1 and S_2 carry $\ell_1 = \ell_2 = 0$ and possess completely symmetric transverse shape and free space propagation characteristics. This is because the nonlinear coherence, given by eq. (4.13), remains the same with an exchange of labels $a \leftrightarrow b$. For resonant input fields with $\Omega_{a,b}^0 = 0.64\Gamma$ – which maximizes nonlinear power output for incident plane wave fields –, we show in Fig. 36 the spatial characteristics of the generated beams. It is

Figure 36 – (a) Intensity distribution at the medium exit $|\Omega_s(z = L/2)|^2$, (b) free space propagation of the generated beam, (c) mode components $\eta_{\ell_s p}$, and (d) normalized radial distribution of the FWM beam at $z/z_R = 0, 1/2, 1$. $\Omega^0_{a,b} = 0.64\Gamma$ and $\delta_a = \delta_b = 0$.

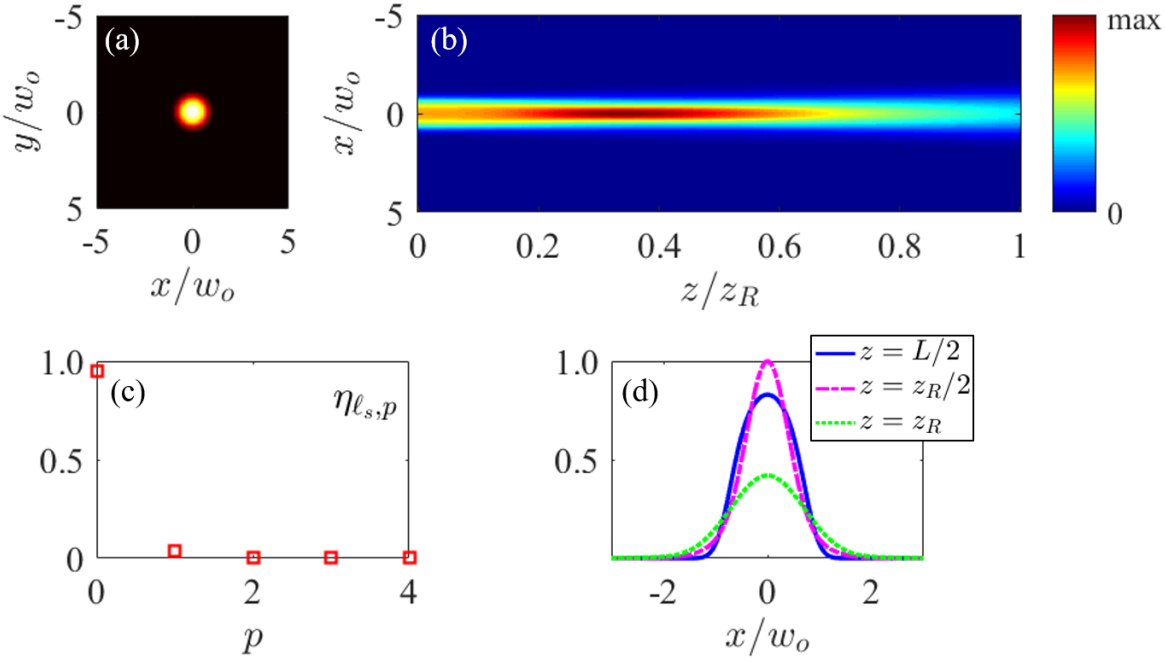

Source: The author (2021).

seen that the output beams possess almost no contribution from modes with $p \neq 0$, i.e., they are essentially purely Gaussian.

5.1.1 *Effect of pump intensity*

Now, we investigate the effect of incident beam amplitudes on the generated beam shape. Figure 37 shows the FWM beam propagation for different values of $\Omega^0_a = \Omega^0_b = \Omega$. We note that as the amplitudes increase, the overall shape of the generated beam changes significantly. Near the medium exit, $z/z_R \approx 0$, the beam becomes ring shaped. We attribute this effect to a spatial saturation effect, which can be understood by inspecting equation (4.13). In all cases, the near field intensity profile will be determined by the nonlinear coherence, $|\sigma_{\rm NL}|^2$, and due to the Gaussian distribution of the fields, for greater amplitudes, the denominator in (4.13) is larger at the center, making $|\sigma_{12}^{2a-b}(\vec{r})|$ smaller in this region. Nonetheless, after propagating distances of the order of z_R, the beams become mainly Gaussian in all cases, as we can see in the radial profile at $z = z_R$ (green line) in the last column of Fig. 37. In Figure 38 we show the dependence of rms quantities with Ω. Since we are dealing with the thin medium regime, we consider the medium exit located at $z/z_R = L/2z_R = 0$.

Sensible change of the longitudinal profile is achieved by increasing Ω. We highlight that the generated beam outside the medium has greater amplitude at positions z/z_R far from 0, for all incident beam amplitudes. In fact, for increasing Ω, this position is shifted towards greater z/z_R, as seen from figures 36b and 37. This would make one expect the position of minimum $r_{\rm rms}(z)$ to be shifted as well. However, from figure 38, we

Figure 37 – Distribution of mode weights. propagation of the generated beam and radial profiles at positions $z = L/2$ (blue), $z = z_R/2$ (magenta) and $z = z_R$ (green) for Gaussian incident beams with different input Rabi frequency amplitudes $\Omega^0_{a,b} = \Omega$.

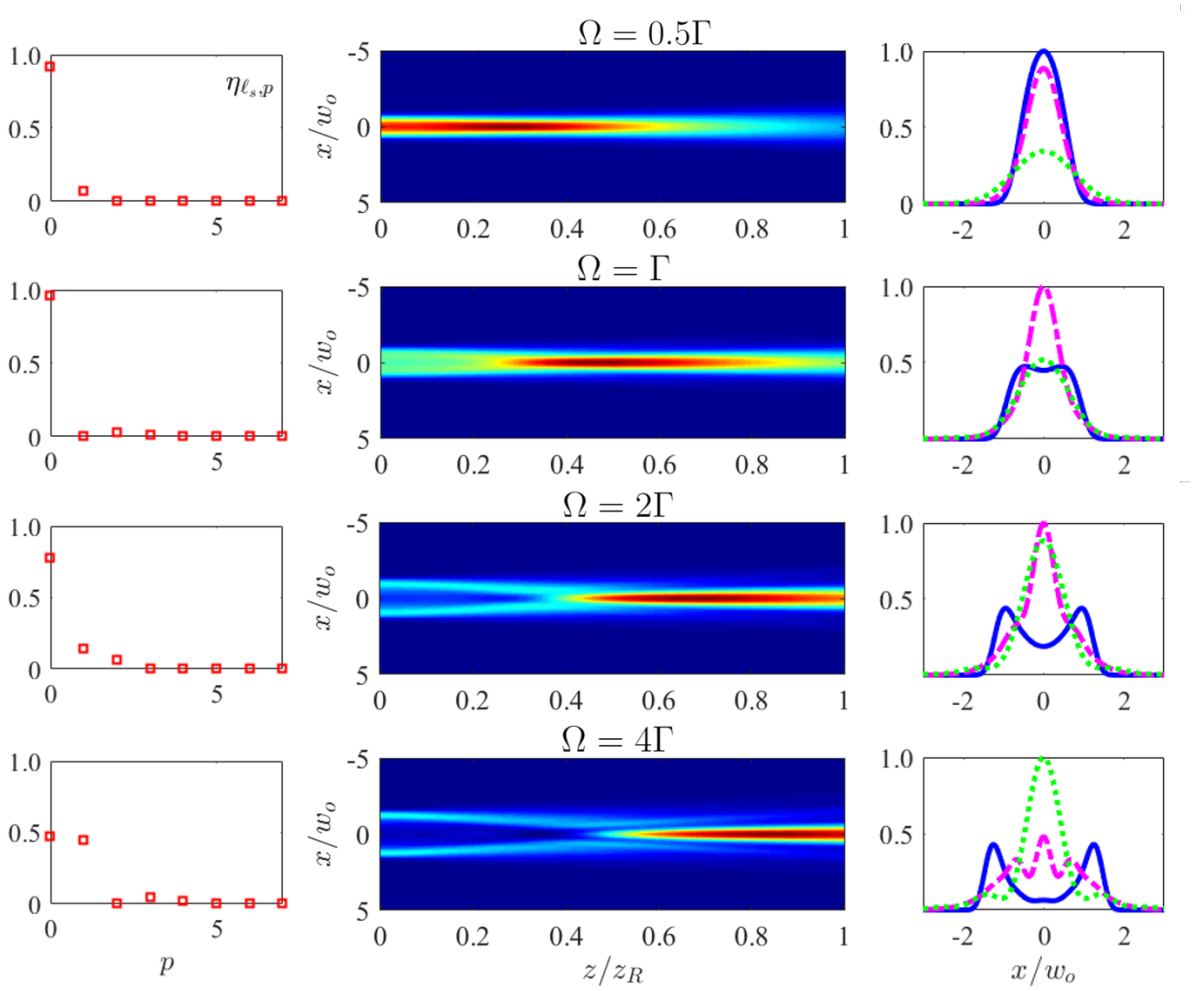

Source: The author (2021).

see that this is not the case. The position where $r_{\text{rms}}(z)$ is minimum, z_m, is practically unchanged by Ω. We conclude that the positions of maximum field amplitude and of minimum rms radius don't necessarily coincide. To explain this, we refer to figure 36d, that shows the radial distribution of the generated field at different z positions. Indeed, the peak field amplitude at $z = z_R/2$, is greater than at $z = L/2$, but the wings are wider, thus balancing the distribution. We note that $r_{\text{rms}}(z)$ does not correspond to the radial position where the field amplitude decreases by a factor of $1/e$ with respect to the amplitude at the center, which is true for Gaussian beams. For smaller Ω, the values for $\eta_{\ell_s p}$ approach those obtained with the analytical expression (4.62), because the influence of the denominator of $\kappa(\vec{r})$ on the overlap integral decreases. Also, for smaller amplitudes, the quality factor M^2 approaches unity, its lower bound [64].

Figure 38 – Behaviour of $r_{\text{rms}}(z)$ and the longitudinal parameters (θ_{rms}, r_m, z_m and M^2) for the symmetric generated beams for different incident Rabi frequency amplitudes $\Omega^0_{a,b} = \Omega$.

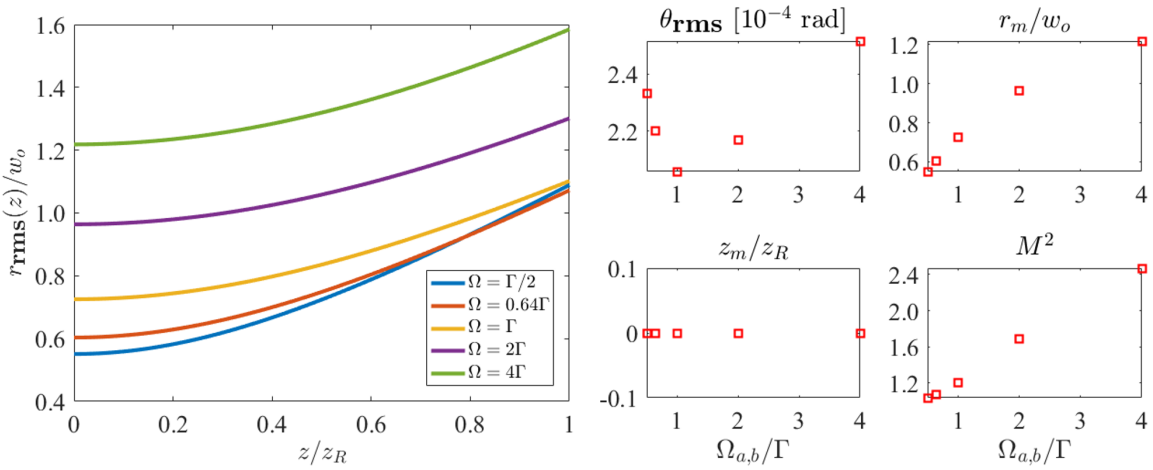

Source: The author (2021).

5.1.2 *Effect of detunings from resonance*

To understand the influence of the medium resonances on the spatial characteristics of the generated beams, we investigate the effect of the detunings from resonance, $\delta_{a,b}$, on the free space propagation of the generated beam. First, we consider a situation where both beams have equal detunings, i.e., come from the same laser source. This represents our experimental setup. We see from Fig. 39 that $\delta_{a,b}$ has an intuitive effect on the FWM beams. On resonance, the beams are generated with the maximum radius and the minimum divergence. As we move away from the resonance, the initial radius decreases, while the divergence angle increases. It is interesting to note that z_m changes considerably for varying incident beam detunings. Above resonance, z_m is shifted to negative values, while below resonance, it is shifted to positive values. The quality factor is maximum at resonance and approaches unity as $\delta_{a,b}$ goes away from resonance. These results suggest that it is possible to translate the position where the minimum waist of the FWM beam occurs by controlling the frequency of the incident beams. This translation comes with not much change on the other beam parameters.

To evidence that the influence of the frequency degrees of freedom depend on the incident beam amplitudes, we show in figure 40 the rms radii of the symmetric generated beams when $\Omega^0_{a,b} = 0.35\Gamma$. We see that all five curves, at each $\delta_{a,b}$ value, are now closer to each other. The longitudinal parameters are not shown, but we can see that r_m varies much less with the detunings and z_m appears to be approximately 0 for all $\delta_{a,b}$. In the limit $\Omega^0_{a,b} \to 0$, all curves in figure 40 would become equal. This is because the coupling κ would factor out of the integral in (4.32) and the frequency degrees of freedom would not affect the overall shape of the generated beam, only its power. Also, in this limit, the overlap integral can be calculated with (4.62).

A common configuration in many experiments uses a strong pump beam frequency locked near resonance and a weak probe beam that has its frequency scanned around resonance. We now turn to a situation where the two incident beams do not have the same detuning, but maintain the Rabi frequency amplitudes equal, $\Omega^0_a = \Omega^0_b$. When the detunings of fields E_a and E_b are not equal, there is no longer a symmetry under the

Figure 39 – Behaviour of $r_{\text{rms}}(z)$ and the longitudinal parameters for the symmetric generated beams with varying $\delta_a = \delta_b$. Incident field Rabi frequency amplitudes are $\Omega^0_{a,b} = \Gamma$.

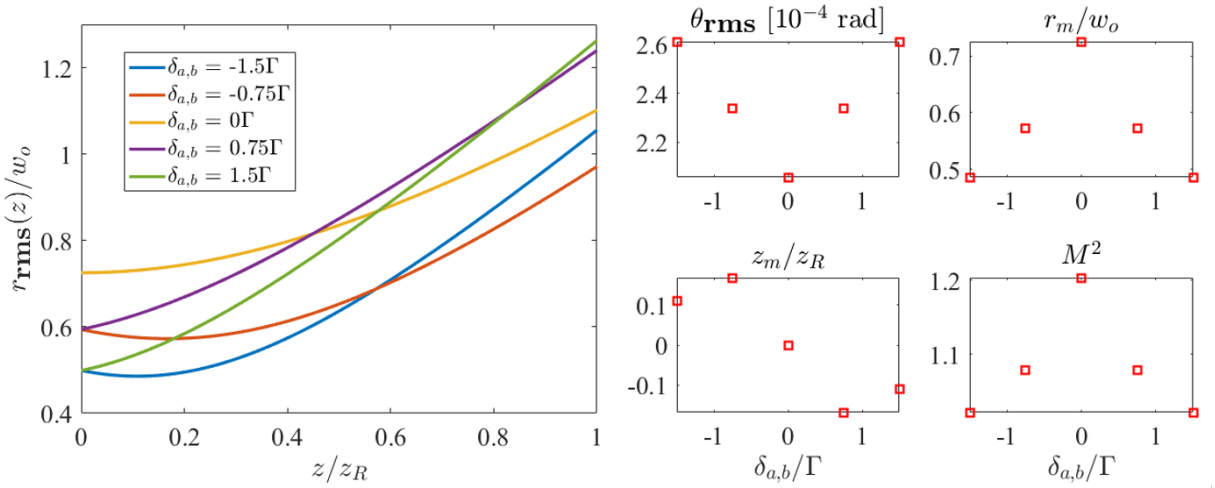

Source: The author (2021).

Figure 40 – Behaviour of $r_{\text{rms}}(z)$ for the symmetric generated beams with varying $\delta_a = \delta_b$. Incident Rabi frequency amplitudes $\Omega^0_{a,b} = 0.35\Gamma$.

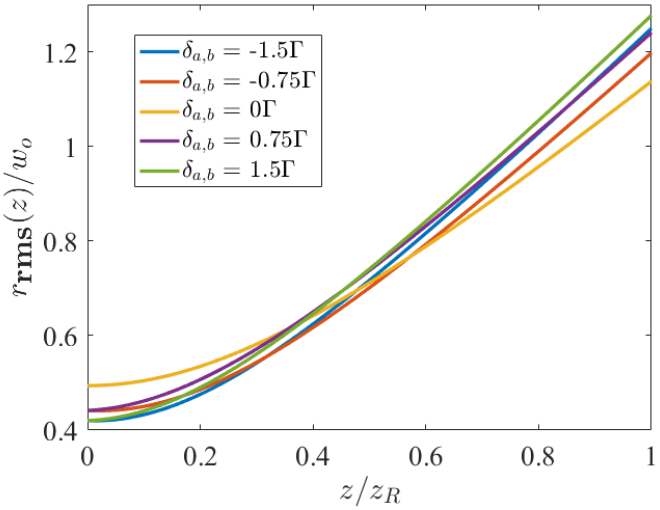

Source: The author (2021).

exchange $a \leftrightarrow b$ in equation (4.13), and the generated signals S_1 and S_2 are shown to differ.

First, we set the frequency of E_a on resonance, $\delta_a = 0$, and make δ_b vary around $\delta_b = 0$. Figure 41a shows the radii of both mixing beams on free space propagation in this situation. We see that the same detuning shifts from resonance only on δ_b also result in changes in the focusing region of both FWM beams. However, the positions of minimum radius, z_m, of the two signals are translated to opposite directions (figure 41b). A more focused beam on direction $(2\vec{k}_a - \vec{k}_b)$ is accompanied by a more spread beam on direction $(2\vec{k}_b - \vec{k}_a)$, and vice versa. The values of the divergence angle θ_{rms}, minimum radius r_m and quality factor M^2, also shown in figure 41b, are very similar for both signals. Further,

their dependence on δ_b is similar that seen in the case with $\delta_a = \delta_b$. In figure 41c we show the longitudinal profile of S_1 and S_2 for $\delta_a = 0$ and $\delta_b = 0.75\Gamma$, corresponding to the purple curves of figure 41a. Referring to the discussion of Section 5.1.1, we see that in this case, the position of minimum $r_{\rm rms}(z)$ seems to be closer to the position of maximum field amplitude outside the nonlinear medium.

Figure 41 – (a) Behaviour of $r_{\rm rms}(z)$ of signals S_1 and S_2 for $\Omega^0_{a,b} = \Gamma$, $\delta_a = 0$, and different values of δ_b. (b) Longitudinal parameters of both generated beams. (c) Propagation of both generated beams outside the interaction medium and mode components $\eta_{\ell_s p}$ and phases $\Phi_{\ell_s p}$ for $\delta_a = 0$ and $\delta_b = 0.75\Gamma$. Red squares refer to S_1 and black x refer to S_2.

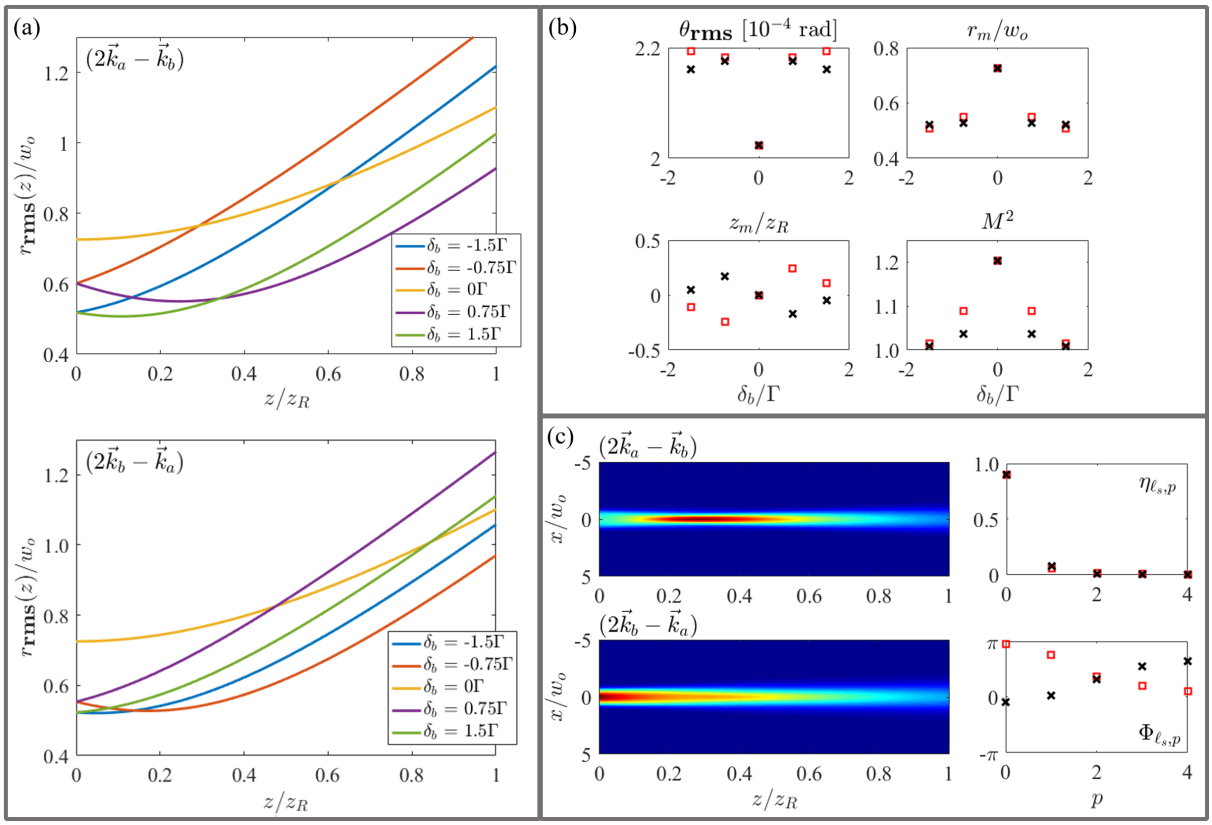

Source: The author (2021).

Also, the distributions of η_{0p} are similar for both signals, with u_{00} having the greatest contribution, as before, and slightly different weights for the modes with $p \neq 0$. However, the relative phases of the modes u_{0p} that are being superimposed are quite different between S_1 and S_2, and this is the dominant factor that leads to the differences in the longitudinal profiles. To confirm this, we show in figure 42 the propagation of the intensity profile of the field expansion obtained with the same distribution of $\eta_{\ell_s,p}$ of figure 43c, but neglecting the phases $\Phi_{\ell_s,p}$. We see that the two fields calculated in this manner have very similar longitudinal behaviors, and no noticeable shift of z_m occurs.

Now, we set the detuning of E_a fixed at $\delta_a = -0.75\Gamma$ and vary δ_b, that takes the same values as before. We see from Fig. 43 that the longitudinal beam parameters of both FWM signals are also affected by δ_b. The distributions of these parameters now become asymmetric with respect to δ_b. Figure 43c shows the propagation of the intensity profiles for $\delta_a = -0.75\Gamma$ and $\delta_b = 0$, corresponding to the yellow curves of figure 43a. Once again, the distribution of weights η_{0p} is very similar for S_1 and S_2, and the differences

Figure 42 – Propagation of the intensity profile and $r_{\mathrm{rms}}(z)$ of both generated signals for $\delta_a = 0$ and $\delta_b = 0.75\Gamma$ calculated considering the same $\eta_{\ell_s,p}$ distributions of figure 41c and neglecting the phases $\Phi_{\ell_s,p}$.

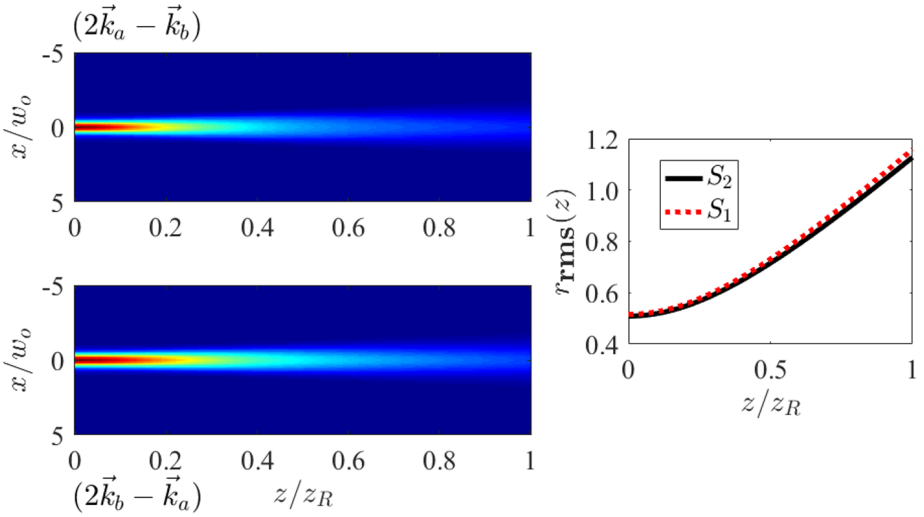

Source: The author (2021).

Figure 43 – Same as figure 41 but with $\delta_a = -0.75\Gamma$

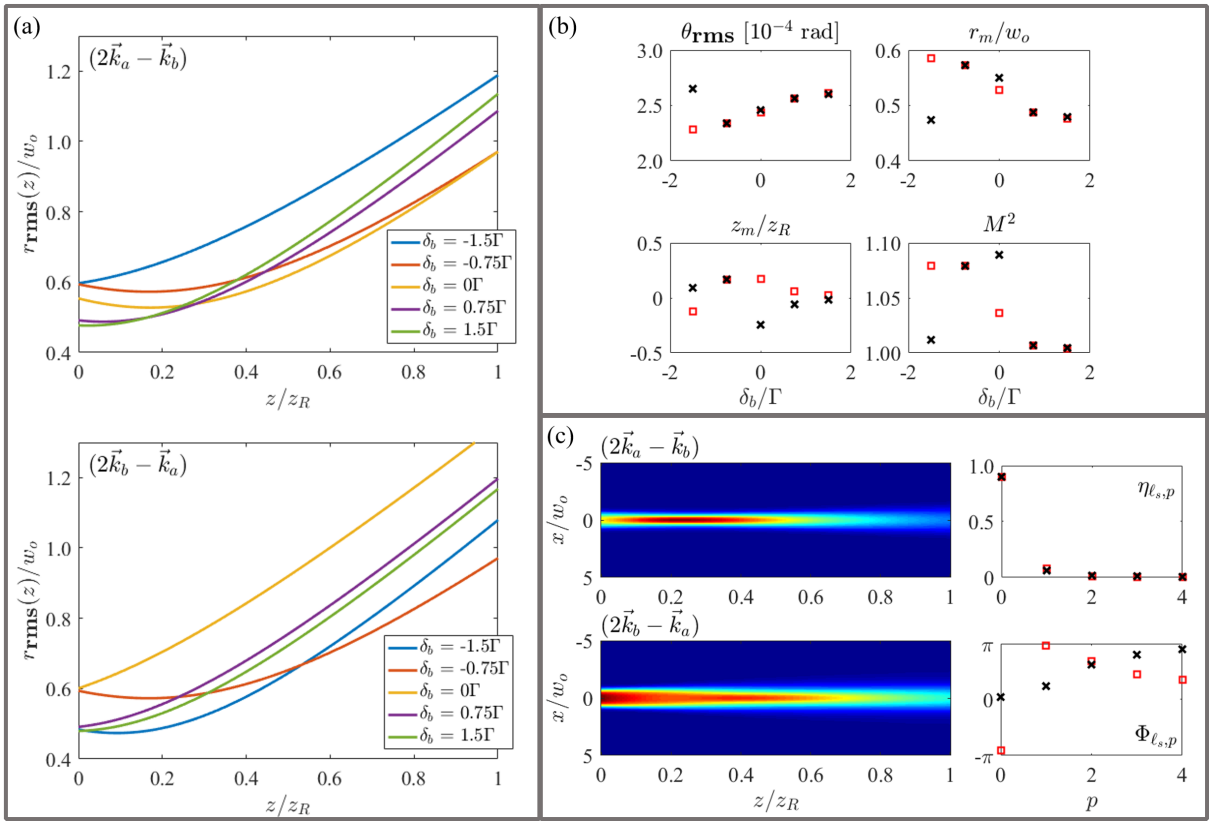

Source: The author (2021).

seen between both beams are due to the distributions of relative phases Φ_{0p}.

The effect our calculations reveal resembles that of Kerr lensing, where the total index

of refraction in the medium can be written as $n = n_0 + n_2 I$, where n_0 and n_2 are the linear and nonlinear refractive indices and I is the beam intensity. The total index of refraction is thus modulated by the spatial distribution of the beam. Evidently, the source term in the wave equation we started with isn't written in this form. However, in the near-field, the product $\Omega_a^2 \Omega_b^*$ is in some cases very much representative of Ω_s. Experimentally, the overlap of input intensities is shown to coincide with the FWM beam intensity distribution [19]. In light of these facts, we write (4.23) as

$$\begin{aligned} \frac{i}{2k_s}\nabla_\perp^2 \Omega_s + \frac{\partial \Omega_s}{\partial z} &= \kappa \Omega_a^2 \Omega_b^*, \\ &\simeq g\kappa\Omega_s. \end{aligned} \tag{5.1}$$

where g is a parameter that can be thought of a conversion efficiency factor. We expect Ω_s to be nearly Gaussian, and for simplicity we consider $|\nabla_\perp^2 \Omega_s / 2k_s| \ll |\partial \Omega_s / \partial z|$. From equation (4.25), we see that κ can be written as $\kappa = -i\kappa_0 \chi_{\text{eff}}^{(3)}$. Because of the thin-medium condition, we neglect the z dependence of $\chi_{\text{eff}}^{(3)}$, and take its value at $z = 0$. The solution to the generated beam at the medium exit is

$$\Omega_s(L/2) = \Omega_s(-L/2) e^{-ig\kappa_0 \chi_{\text{eff}}^{(3)} L}, \tag{5.2}$$

where, in order to avoid a trivial null solution, $\Omega_s(-L/2)$ is taken as a Gaussian seed field. We write the final form

$$\Omega_s(L/2) = \Omega_s(-L/2) e^{g\kappa_0 \text{Im}\chi_{\text{eff}}^{(3)} L} e^{-ig\kappa_0 \text{Re}\chi_{\text{eff}}^{(3)} L}. \tag{5.3}$$

We see that the imaginary part of κ is responsible for modulating the FWM field amplitude, while the real part affects the phase distribution of the FWM field. The modification to the phase distribution is equivalent to a spatially dependent change in the total index of refraction inside the medium,

$$n_{\text{total}} = n_s + n_2' \text{Re}\chi_{\text{eff}}^{(3)}(r; \delta), \tag{5.4}$$

where $n_2' = gc\kappa_0 L/\omega_s$. Now we look at the first situation considered: incident fields with equal detunings, $\delta_a = \delta_b$. We show in figure 44 a plot of the real part of $\chi_{\text{eff}}^{(3)}(r)$ as a function of the radial coordinate for different values of $\delta_{a,b}$. The Rabi frequency amplitudes are $\Omega_{a,b}^0 = \Gamma$. We see that below resonance, $\delta_{a,b} < 0$, the total index of refraction is greater at the center, $r = 0$, and decreases at greater r positions (red curve). Thus, the FWM beam is focused. On resonance, $\delta_{a,b} = 0$, the total index of refraction is unaffected by $\chi_{\text{eff}}^{(3)}$ at all r positions. The FWM beam is neither focused or defocused. Above resonance, $\delta_{a,b} > 0$, n_{total} is smaller at the center, and increases as we move away from this position (green curve). As a result, the FWM beam is defocused. This agrees with the behaviour of z_m shown in figure 39.

The same analysis can be made regarding the second case, where δ_a is fixed at resonance, and δ_b varies. The nonlinear susceptibility related to S_2 has a radial dependence similar to that shown in figure 44 for $\delta_b > 0$ and $\delta_b < 0$, while for S_1, the curves corresponding to $\delta_b < 0$ and $\delta_b > 0$ are switched. Thus, the changes in the total index of refraction for S_2 are the same for the case with $\delta_a = \delta_b$, and for S_1 these changes are opposite. This agrees with the behaviour of z_m shown in figure 41 for both generated beams.

Figure 44 – Radial distribution of $\mathrm{Re}\chi^{(3)}_{\mathrm{eff}}(r;\delta)$ for different values of $\delta_{a,b}$ considering Gaussian incident beams with amplitudes $\Omega^0_{a,b} = \Gamma$.

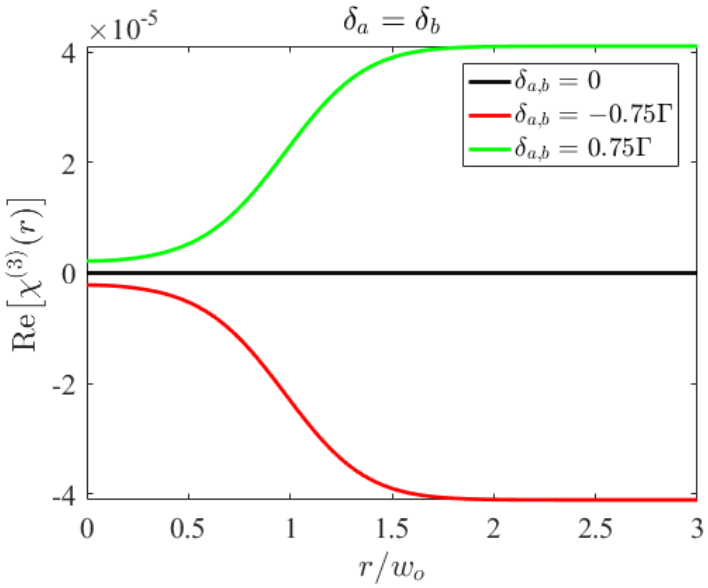

Source: The author (2021).

5.2 LG beams

First, we consider a configuration where input beams possess different topological charges, $\ell_a \neq \ell_b$. In this case, the coherences responsible for the generation of S_1 and S_2 are not symmetrical, regardless of the frequency degrees of freedom. The transverse shapes of the FWM beams are dictated by the OAM conservation condition. For signal $(2a-b)$, we have

$$\begin{aligned}\Omega_1 &= \sum_p A_{\ell_1 p} u_{\ell_1 p}(\vec{r}_\perp, z) \\ &= g_1(r,z)e^{-i\ell_1\phi}\end{aligned} \tag{5.5}$$

where $\ell_1 = 2\ell_a - \ell_b$ is the only topological charge that emerges due to the OAM conservation selection rule in the azimuthal integral of (4.32). Assuming $\ell_1 \neq 0$, Ω_1 will show a phase singularity and null intensity at $r = 0$. Since all azimuthal dependence is contained in the exponential $e^{-i\ell_1\phi}$, the intensity profile $|\Omega_1|^2 = |g_1(r,z)|^2$ will be ring-shaped, but differ in some degree from a pure LG mode with TC ℓ_1 since there are multiple p orders contributing to $g_1(r,z)$. It is possible, however, to have $\ell_1 = 0$, and in this case the output beam will show no phase singularity and its intensity profile will be Gaussian shaped, but differ from a pure Gaussian beam because there will also be multiple p orders contributing to the signal. Similarly, for S_2, $\Omega_2 = g_2(r,z)e^{-i\ell_2\phi}$, where $\ell_2 = 2\ell_b - \ell_a$. The same points can be made about Ω_2.

The free space propagation properties of both signals also depend on the medium quantities in a manner similar to what has been shown for Gaussian inputs. This suggests that beams with OAM don't change qualitatively the effect of $\chi^{(3)}_{\mathrm{eff}}(r,z;\delta)$ on $r_{\mathrm{rms}}(z)$. As an example, if incident fields have equal topological charges $\ell_a = \ell_b$ and detunings $\delta_a = \delta_b$, the full symmetry between coherences σ_{12}^{2a-b} and σ_{12}^{2b-a} is recovered, and we get a behaviour

very similar to that of Fig. 39. The difference is that the values of $r_{\rm rms}(z)$ at the medium exit and the divergences are greater due to the fact that the output beams possess $\ell \neq 0$ (figure 45).

Figure 45 – Behaviour of $r_{\rm rms}(z)$ and of the longitudinal parameters for different values of $\delta_{a,b}/\Gamma$. Input Rabi frequency amplitudes are $\Omega^0_{a,b} = \Gamma$ and $\ell_a = \ell_b = 1$.

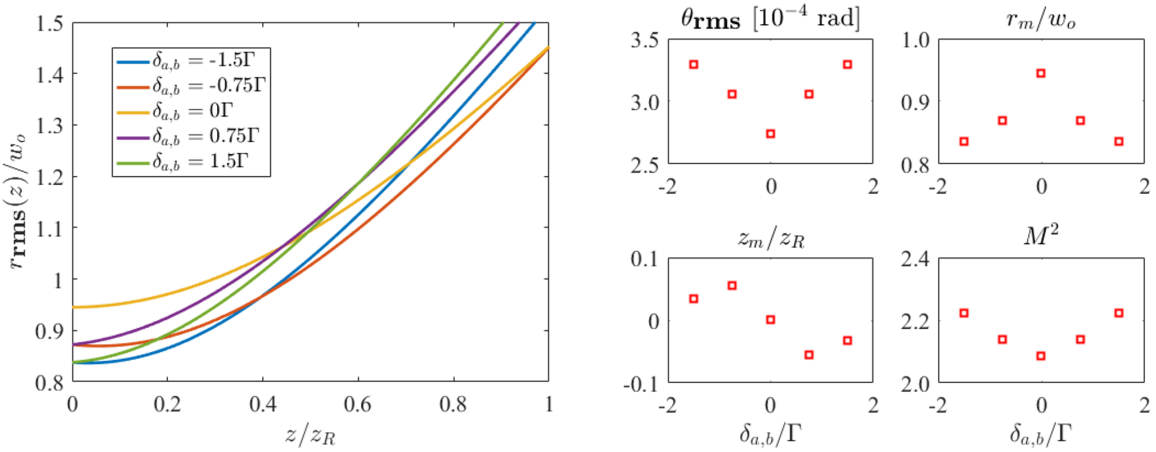

Source: The author (2021).

The phase discontinuities inherent to beams with OAM can help one understand how $\chi^{(3)}_{\rm eff}(r, z; \delta)$ affects the superposition coefficients $A_{\ell p}$. Figure 46 shows the phase distribution of $\sigma_{12}^{2a-b} \propto e^{-i(2\ell_a - \ell_b)\phi}$ for $\ell_a = 2$, $\ell_b = 0$, $\delta_a = 0$ and varying δ_b and different values of $\Omega^0_{a,b}$. In this case, $\ell_1 = 4$. Off resonance, we see that the phase distribution suffers a global rotation and a distortion near the origin, relative to $\delta_b = 0$ (center). The rotation direction is opposite to the distortion direction and the orientation of both effects change with the sign of δ_b. Further, the distortion is larger for increasing incident Rabi frequency amplitude. We chose to show these effects on the phase distribution of the coherence, and not of the FWM field, because the latter presents discontinuity rings that result from higher p order modes with negligible contribution. Similar results have been reported in refs. [29, 30], where more complicated atomic systems are considered. In ref. [29], it is shown that the phase mismatch also distorts the phase distribution of the FWM field. In these works, however, connection is established between this effect and other spatial properties of the FWM signal. In the case of Gaussian beams, the detunings also affect the phases of $\sigma_{\rm NL}$, but since the phase distributions are always circularly symmetric, these effects can't be seen.

We now turn to a situation where $\ell_a = l$ and $\ell_b = nl$, where n is an integer. The topological charge selection rule leads to

$$(\ell_1, \ell_2) = (2 - n, 2n - 1)l. \tag{5.6}$$

A few cases are of special interest:

- For $n = 1$, both outputs possess the same OAM as the inputs, $(\ell_1, \ell_2) = (l, l)$.
- For $n = -1$, we get two outputs with a three-fold increase in OAM magnitude and opposite handedness, $(\ell_1, \ell_2) = 3(l, -l)$.

Figure 46 – Phase distribution of σ_{12}^{2a-b} at $z = L/2$ for $\ell_a = 2$, $\ell_b = 0$, $\delta_a = 0$ and $\delta_b/\Gamma = -0.75; 0; 0.75$ (from left to right), for different field amplitudes $\Omega_{a,b}^0 = \Gamma; 4\Gamma$ (from top to bottom). Red and black arrows indicate the orientation of the rotation and distortion effects, respectively.

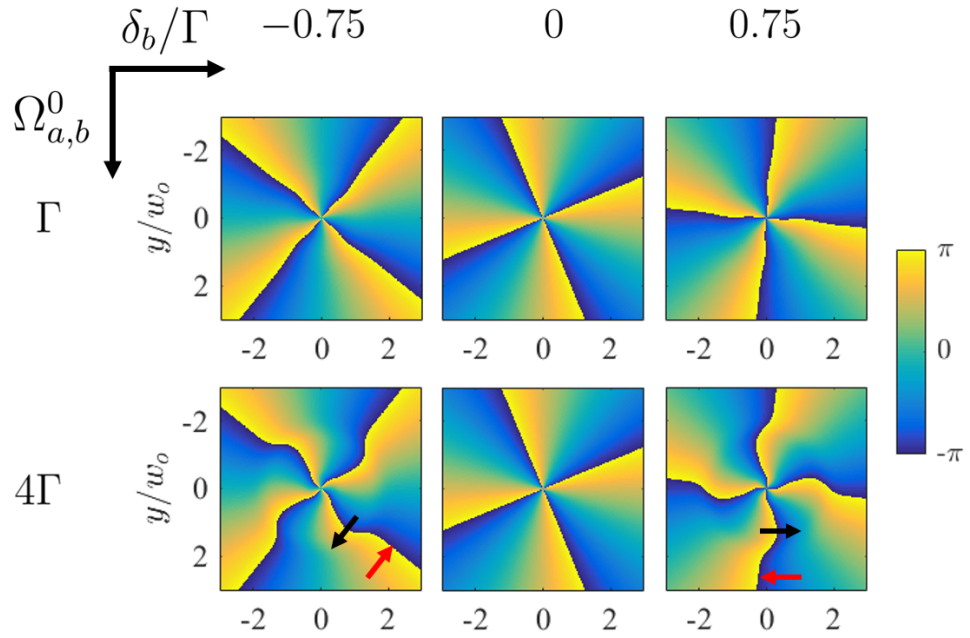

Source: The author (2021).

- For $n = 2$, we'll have one output beam with the sum of input OAM, while the other will possess no topological charge, $(\ell_1, \ell_2) = (0, 3l)$.

Considering $l = 1$, in the first case, $n = 1$, both generated beams are completely symmetrical, and we see in figure 47a all of their spatial properties and the distributions of mode weights and phases. They are very close to pure u_{10} LG beams. The OAM is evident from the number of radial discontinuities on the phase distribution. The twisting of the phase distribution as the beams propagate is due to their helicity, and has no relation with the frequency degrees of freedom.

When $n = -1$ the spatial properties and expansion coefficients are shown in figure 47b. The relative phases are all equal, and thus become a global phase that does not affect the expansion of LG modes of the generated fields. Further, we note that the distribution of $\eta_{\ell_s p}$ is exactly the same for both S_1 and S_2. The intensity distributions of the two beams are thus equal throughout all propagation from the medium exit to $z = z_R$. The only difference is the helicity of the beams, which can be verified by looking at the phase distributions at $z = 0$ and $z = z/z_R$. This can be understood by inspecting the integrand of equation (4.32) and the LG mode expression, given by (2.78). Mathematically, the only role of the handedness of the incident topological charges is to determine the OAM, ℓ_s, via the azimuthal integral. For the radial integral, only the absolute values of ℓ_a and ℓ_b are relevant. Once again, the twisting of the phases upon propagation – in opposite directions for S_1 and S_2 – is due solely to the helicities of the beams.

Finally, for $n = 2$, we get two beams with that are asymmetric with respect to intensity and phase distributions. Figure 47c shows the spatial properties of the generated FWM beams. In this case, S_1 and S_2 present very different behaviors. S_1 is generated with a ring shape, but has no phase singularity, and transitions to a Gaussian shaped beam upon propagation. S_2, on the other hand, maintains its initial shape, propagating

Figure 47 – Intensity and phase distributions, mode weights $\eta_{\ell_s p}$ and relative phases $\Phi_{\ell_s p}$ and radial profiles at positions $z = L/2, z_R/2$ and z_R for the two generated signals for the cases (a) $n = 1$, (b) $n = -1$ and (c) $n = 2$. Where no distinction is made between S_1 and S_2, it is applicable to both. In all cases, $\Omega^0_{a,b} = \Gamma$, $\delta_a = \delta_b = 0$ and $l = 1$.

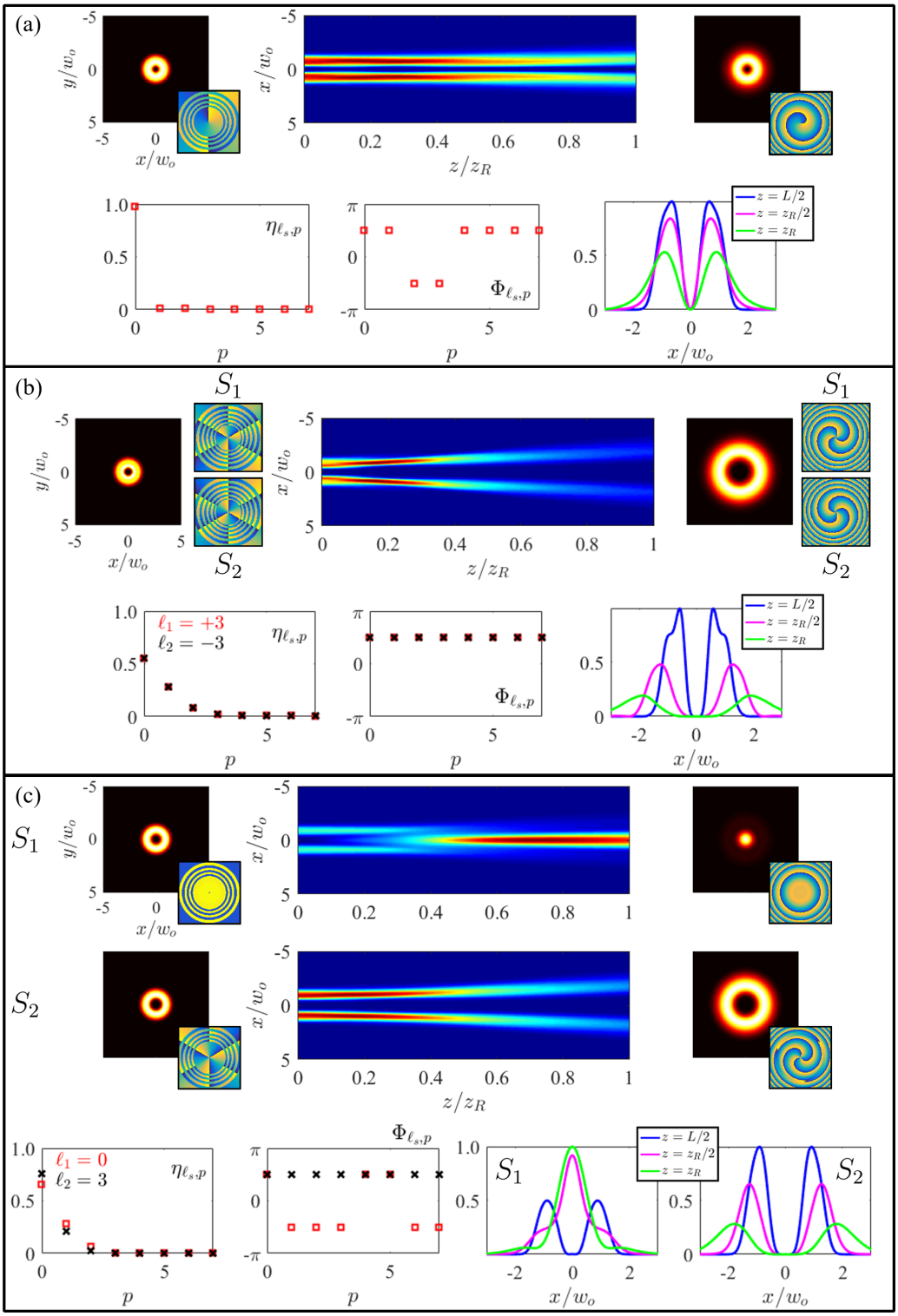

Source: The author (2021).

Figure 48 – Behavior of $r_{\text{rms}}(z)$ for S_1 and S_2 of cases $n = \pm 1, 2$. Detunings are fixed at resonance, $\delta_a = \delta_b = 0$, and Rabi frequency amplitudes are $\Omega^0_{a,b} = \Gamma$.

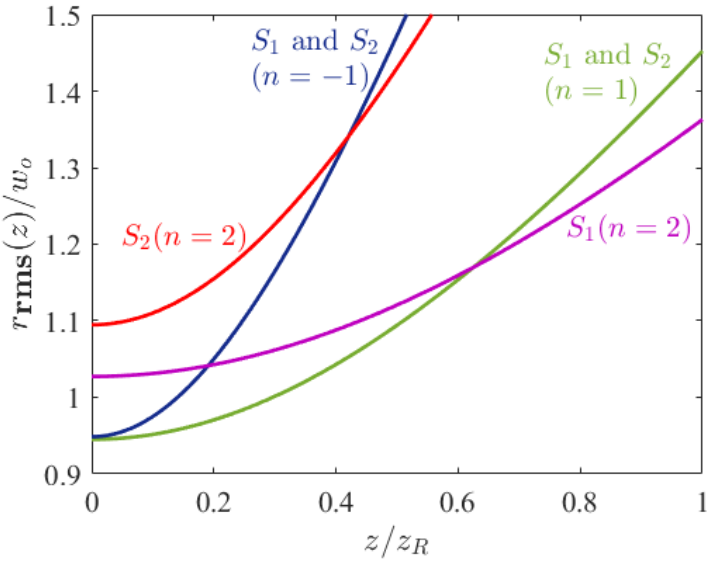

Source: The author (2021).

approximately as one would expect from an LG beam with nonzero topological charge.

The far-field intensity distributions in all cases correspond to the OAM content of the FWM beams. In the near-field, the situation is a little more subtle, and an intuitive explanation is the following. The near-field beam profiles are dictated by the nonlinear coherences, σ_{12}^{2a-b} and σ_{12}^{2b-a}. The denominator in equation (4.13) has little influence here, and thus the FWM beam shape leaving the interaction medium is mainly determined by the product of incident fields. For $n = \pm 1$, the coherences that generate both FWM signals contain products of LG modes with $|\ell| = 1$ only. For both of these cases, S_1 and S_2 will possess ring shaped intensity profiles close to that of an LG mode with $|\ell| = 1$, leaving the interaction medium. For $n = -1$, the generated beams have three times the topological charge, and a stronger diffraction occurs upon propagation. The ring size increases considerably as compared to $n = 1$. On the other hand, when $n = 2$, the coherences that generate S_1 and S_2 are products of LG modes with $\ell = 1, 2$. Both generated beams thus leave the medium with larger intensity rings, in comparison with $n = \pm 1$. Because of the topological charge difference, S_2 ($\ell_2 = 3$) diffracts much more than S_1 ($\ell_1 = 0$). All of this can be confirmed by looking at $r_{\text{rms}}(z)$ for the three cases, shown in figure 48.

A statement that summarizes the previous paragraph is that the near-field intensity distributions are dictated by the product of incident fields, but upon free-space propagation, they are not necessarily stable. This is because the FWM fields must satisfy the nonhomogeneous PWE inside the nonlinear medium, where the source term that drives the signal generation is nonzero; but in the region $z > L/2$, they must satisfy the homogeneous PWE. As an example, signal S_2 for $n = 2$ possesses a dark valley at $z = L/2$ because the source term has this shape at $z \leq L/2$. Outside the medium, where the field propagates freely, this shape is not stable for beams with no topological charge, and this is the reason for the transition to the final Gaussian shape at $z = z_R$.

5.3 Suppression in a thick medium

As mentioned, when $L/z_R \to \infty$, the modes in the expansion for Ω_s must satisfy the mode number selection rule. In Chapter 4 we showed how this requirement arises and how it results in the suppression of one of the generated signals. Here we briefly discuss two cases. We'll take $\kappa(r, z; \delta) \simeq \overline{\kappa}(\delta)$, such that equation (4.62) can be used to calculate the FWM expansion coefficients.

First, consider resonant input fields with $(\ell_a,\ell_b) = (1, 0)$. From the OAM conservation, the output topological charges will be $(\ell_1, \ell_2) = (2, -1)$. The generated fields are written as

$$\begin{aligned} \Omega_1 &= \sum_p \Lambda_{000p}^{1102}(0) I_p(L) u_{2p}, \\ \Omega_2 &= \sum_p \Lambda_{000p}^{001-1}(0) I_{p+1}(L) u_{-1p}. \end{aligned} \tag{5.7}$$

We see that when $L/z_R \to \infty$, S_1 will possess only $p = 0$ and S_2 will be suppressed. Thus, the simultaneous transfer of OAM to both FWM is not achievable in a thick medium.

Next, for pumps $\Omega_a = \Phi_m$, where $\Phi_m = (u_{10} - u_{m0})/\sqrt{2}$, and $\Omega_b = u_{00}$, the expansion coefficients are given by equations (4.72) and (4.73). Figure 49 shows the beam power of both FWM signals as a function of L/z_R when $\Omega_a = \Phi_4$. For $L \approx z_R$, the output power of S_1 and S_2 are comparable. As L increases, however, P_2 reaches a maximum and begins to decrease, until it is negligible in comparison to P_1. In this manner, the simultaneous transfer of arbitrary shape to both FWM beams is not possible in a thick medium.

In general, the suppression occurs to the signal that is a result of the interaction with two contributions from u_{00}, and one from the higher order field.

Figure 49 – Beam power of S_1 and S_2 as a function of L/z_R for incident fields given by $\Omega_a = \Phi_4$ and $\Omega_b = u_{00}$.

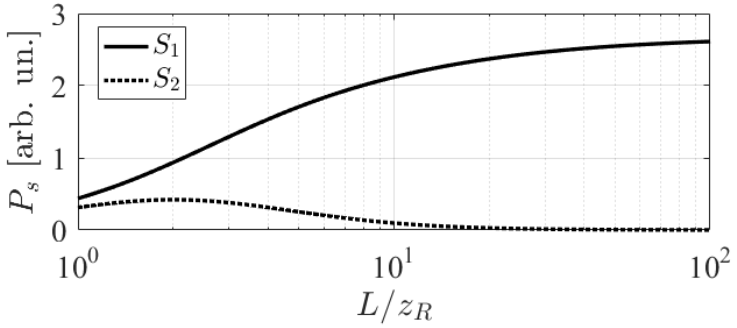

Source: The author (2021).

6 CONCLUSIONS

In this work we conducted a detailed theoretical analysis of the spatial shape of two FWM signals (S_1 and S_2) generated in a sample of cold two-level atoms. The FWM field was found in terms of a superposition of LG modes, where the coefficients are given by the projection of the nonlinear polarization onto the LG function space. A thin-medium regime was considered. For equal incident beams, the two signals are completely symmetric. This symmetry is lost when the spatial distributions or the detunings from resonance of incident beams E_a and E_b are different.

Considering only Gaussian incident beams, we showed that the combined spatial and spectral degrees of freedom of the nonlinear susceptibility $\chi^{(3)}_{\text{eff}}$ lead to modifications on the expansion coefficients. These modifications resulted in intuitive effects on the free space propagation of the generated beam when the frequencies of incident beams are set off resonance. The most notable of these effects is the focusing or defocusing of the FWM beam upon free space propagation, outside the interaction medium. This was seen as a translation of the position of minimum beam waist, z_m to positive or negative z values, depending on the signal of the detuning shift. When the frequency of one of the incident fields is set on resonance, the generated signals are non symmetric, and the translation of z_m for S_1 and S_2 occurs in opposite directions.

With a modification to the original wave equation for the FWM field, a solution is found that explains these results in terms of a change in the total index of refraction inside the interaction medium. The behaviour of this modified solution resembles that of the Kerr effect, where the index of refraction is modulated by the intensity distribution of the incident beam.

When incident beams posses Laguerre-Gaussian distributions, our calculations reveal a rotation and bending of the phase distribution of the FWM field that occurs when we vary the frequency degrees of freedom. This effect is similar to what is reported in references [29, 30]. However, in these works no connection is established with the longitudinal profile of the FWM beam outside the medium.

Finally, in the thick-medium regime, we considered incident fields given by pure LG modes or a superposition of two LG modes. This regime can be more easily reproduced in a cell of Rb vapor, a system that has been widely explored with numerous objectives. In this scenario, using the overlap integral of four LG modes only, we showed that the requirement of the Gouy phase-matching can result in the suppression of one of the two generated signals.

We also described our experimental apparatus and presented preliminary experimental results of FWM in our magneto-optical trap. The narrowing of the FWM lineshapes (of S_1 and S_2) due to the non trivial intensity distribution of incident LG beams was evidenced in our measurements and the origin of this effect was discussed. By calculating an effective lineshape, that takes into account the full spatial dependence of the incident fields participating in the nonlinear process, we obtained FWM spectra that become narrower for increasing topological charge of one of the incident beams. This makes us believe that both detected FWM signals carried OAM when the experiments were performed introducing a topological charge onto beam E_b. However, we do not have additional data to support this hypothesis.

The intensity profile of the FWM signal generated in our MOT was obtained using incident Gaussian beams. A procedure was employed to eliminate unwanted scattered light and the revealed FWM beam seems to be approximately Gaussian shaped with some ellipticity. In future projects, we seek to capture the intensity profile of the generated beam when incident beams possess LG distributions as well. The characteristic shape of beams with OAM or an interferometric measurement to reveal information about the phase structure will be important to confirm the presence of OAM in both generated signals.

BIBLIOGRAPHY

[1] L. Allen, M. W. Beijersbergen, R. J. C. Spreeuw, and J. P. Woerdman. *Phys. Rev. A*, vol. 45, p. 8185, 1992.

[2] M. J. Padgett *Opt. Express*, vol. 25, no. 10, pp. 11265–11274, 2017.

[3] S. Chu, L. Hollberg, J. E. Bjorkholm, A. Cable, and A. Ashkin *Phys. Rev. Lett.*, vol. 55, no. 1, p. 48, 1985.

[4] R. A. Beth *Phys. Rev.*, vol. 50, no. 2, p. 115, 1936.

[5] H. He, M. Friese, N. Heckenberg, and H. Rubinsztein-Dunlop *Phys. Rev. Lett.*, vol. 75, no. 5, p. 826, 1995.

[6] M. Friese, J. Enger, H. Rubinsztein-Dunlop, and N. R. Heckenberg *Phys. Rev. A*, vol. 54, no. 2, p. 1593, 1996.

[7] J. Leach, M. J. Padgett, S. M. Barnett, S. Franke-Arnold, and J. Courtial *Phys. Rev. Lett.*, vol. 88, p. 257901, Jun 2002.

[8] M. Andersen, C. Ryu, P. Cladé, V. Natarajan, A. Vaziri, K. Helmerson, and W. D. Phillips *Phys. Rev. Lett.*, vol. 97, no. 17, p. 170406, 2006.

[9] X. Pan, S. Yu, Y. Zhou, K. Zhang, K. Zhang, S. Lv, S. Li, W. Wang, and J. Jing *Phys. Rev. Lett.*, vol. 123, no. 7, p. 070506, 2019.

[10] R. W. Boyd, M. G. Raymer, P. Narum, and D. J. Harter. *Phys. Rev. A*, vol. 24, p. 411, 1981.

[11] D. Harter and R. Boyd *IEEE J. Quantum Electron.*, vol. 16, no. 10, pp. 1126–1131, 1980.

[12] A. Yariv and D. M. Pepper *Opt. Lett.*, vol. 1, no. 1, pp. 16–18, 1977.

[13] R. L. Abrams and R. C. Lind *Opt. Lett.*, vol. 2, no. 4, pp. 94–96, 1978.

[14] K. J. Boller, A. Imamoğlu, and S. E. Harris *Phys. Rev. Lett.*, vol. 66, no. 20, p. 2593, 1991.

[15] S. E. Harris, G. Yin, A. Kasapi, M. Jain, and Z. Luo in *Coherence and Quantum Optics VII*, pp. 295–304, Springer, 1996.

[16] K. Dholakia, N. Simpson, M. Padgett, and L. Allen *Phys. Rev. A*, vol. 54, no. 5, p. R3742, 1996.

[17] J. Courtial, K. Dholakia, L. Allen, and M. Padgett *Phys. Rev. A*, vol. 56, no. 5, p. 4193, 1997.

[18] G. Walker, A. Arnold, and S. Franke-Arnold *Phys. Rev. Lett.*, vol. 108, no. 24, p. 243601, 2012.

[19] A. Chopinaud, M. Jacquey, B. V. de Lesegno, and L. Pruvost *Phys. Rev. A*, vol. 97, no. 6, p. 063806, 2018.

[20] A. M. Akulshin, R. J. McLean, E. E. Mikhailov, and I. Novikova *Opt. Lett.*, vol. 40, no. 6, pp. 1109–1112, 2015.

[21] R. F. Offer, D. Stulga, E. Riis, S. Franke-Arnold, and A. S. Arnold *Commun. Phys.*, vol. 1, no. 1, pp. 1–8, 2018.

[22] R. F. Offer, A. Daffurn, E. Riis, P. F. Griffin, A. S. Arnold, and S. Franke-Arnold *Phys. Rev. A*, vol. 103, no. 2, p. L021502, 2021.

[23] J. W. R. Tabosa and D. Petrov *Phys. Rev. Lett.*, vol. 83, no. 24, p. 4967, 1999.

[24] S. Barreiro and J. W. R. Tabosa *Phys. Rev. Lett.*, vol. 90, p. 133001, 05 2003.

[25] S. Barreiro, J. W. R. Tabosa, J. P. Torres, Y. Deyanova, and L. Torner *Opt. Lett.*, vol. 29, no. 13, pp. 1515–1517, 2004.

[26] D. Moretti, D. Felinto, and J. W. R. Tabosa *Phys. Rev. A*, vol. 79, no. 2, p. 023825, 2009.

[27] R. N. Lanning, Z. Xiao, M. Zhang, I. Novikova, E. E. Mikhailov, and J. P. Dowling. *Phys. Rev. A*, vol. 96, 2017.

[28] N. S. Mallick and T. N. Dey. *J. Opt. Soc. Am. B*, vol. 37, pp. 1857–1864, 2020.

[29] H. R. Hamedi, J. Ruseckas, and G. Juzeliūnas *Phys. Rev. A*, vol. 98, no. 1, p. 013840, 2018.

[30] C. Yu and Z. Wang *Phys. Rev. A*, vol. 103, no. 1, p. 013518, 2021.

[31] A. Yariv, *Quantum electronics*. Wiley, 1989.

[32] D. A. Steck, "Rubidium 87 d line data." `https://steck.us/alkalidata/rubidium87numbers.pdf`, 2001. Accessed: 05 April 2021.

[33] C. J. Foot, *Atomic physics*. Oxford University Press, 2005.

[34] B. H. Bransden and C. J. Joachain, *Physics of atoms and molecules*. Pearson Education India, 2003.

[35] H. J. Metcalf and P. Van der Straten, *Laser cooling and trapping*. Springer-Verlag, 1999.

[36] A. Ashkin, J. M. Dziedzic, J. E. Bjorkholm, and S. Chu *Opt. Lett.*, vol. 11, no. 5, pp. 288–290, 1986.

[37] J. Arlt and M. Padgett *Opt. Lett.*, vol. 25, no. 4, pp. 191–193, 2000.

[38] E. Raab, M. Prentiss, A. Cable, S. Chu, and D. E. Pritchard *Phys. Rev. Lett.*, vol. 59, no. 23, p. 2631, 1987.

[39] D. L. Andrews and M. Babiker, *The angular momentum of light*. Cambridge University Press, 2012.

[40] S. M. Barnett and L. Allen *Opt. Commun.*, vol. 110, no. 5-6, pp. 670–678, 1994.

[41] A. M. Yao and M. J. Padgett *Adv. Opt. Photonics*, vol. 3, no. 2, pp. 161–204, 2011.

[42] J. D. Jackson, *Classical electrodynamics*. Wiley, 1999.

[43] M. R. Teague *J. Opt. Soc. Am.*, vol. 73, no. 11, pp. 1434–1441, 1983.

[44] G. Molina-Terriza, J. P. Torres, and L. Torner *Nat. Phys.*, vol. 3, no. 5, pp. 305–310, 2007.

[45] E. Karimi, R. Boyd, P. De La Hoz, H. De Guise, J. Řeháček, Z. Hradil, A. Aiello, G. Leuchs, and L. L. Sánchez-Soto *Phys. Rev. A*, vol. 89, no. 6, p. 063813, 2014.

[46] W. N. Plick and M. Krenn *Phys. Rev. A*, vol. 92, no. 6, p. 063841, 2015.

[47] M. W. Beijersbergen, L. Allen, H. Van der Veen, and J. Woerdman *Opt. Commun.*, vol. 96, no. 1-3, pp. 123–132, 1993.

[48] M. Beijersbergen, R. Coerwinkel, M. Kristensen, and J. Woerdman *Opt. Commun.*, vol. 112, no. 5-6, pp. 321–327, 1994.

[49] N. Heckenberg, R. McDuff, C. Smith, and A. White *Opt. Lett.*, vol. 17, no. 3, pp. 221–223, 1992.

[50] J. Arlt, K. Dholakia, L. Allen, and M. Padgett *J. Mod. Opt.*, vol. 45, no. 6, pp. 1231–1237, 1998.

[51] G. Ruffato, M. Massari, and F. Romanato *Opt. Lett.*, vol. 39, no. 17, pp. 5094–5097, 2014.

[52] P. A. Franken, A. E. Hill, C. Peters, and G. Weinreich *Phys. Rev. Lett.*, vol. 7, no. 4, p. 118, 1961.

[53] *LCOS-SLM X10468/X13267/X13138 series manual.* Hamamatsu Photonics, `https://www.hamamatsu.com/resources/pdf/ssd/x10468_series_etc_kacc1172e.pdf`, Accessed: 05 April 2021.

[54] A. J. A. Carvalho. PhD thesis, UFPE, 2020.

[55] A. A. C. de Almeida. Master's dissertation, UFPE, 2019.

[56] J. Anupriya, N. Ram, and M. Pattabiraman *Phys. Rev. A*, vol. 81, no. 4, p. 043804, 2010.

[57] C. Schwob, P. F. Cohadon, C. Fabre, M. Marte, H. Ritsch, A. Gatti, and L. Lugiato *Appl. Phys. B*, vol. 66, no. 6, pp. 685–699, 1998.

[58] L. Pereira, W. Buono, D. Tasca, K. Dechoum, and A. Khoury. *Phys. Rev A*, vol. 96, p. 053856, 2017.

[59] G. Alves, R. Barros, D. Tasca, C. Souza, and A. Khoury *Phys. Rev. A*, vol. 98, no. 6, p. 063825, 2018.

[60] W. Buono, A. Santos, M. Maia, L. Pereira, D. Tasca, K. Dechoum, T. Ruchon, and A. Khoury *Phys. Rev. A*, vol. 101, no. 4, p. 043821, 2020.

[61] H. J. Wu, L. W. Mao, Y. J. Yang, C. Rosales Guzmán, W. Gao, B. S. Shi, and Z. H. Zhu *Phys. Rev. A*, vol. 101, p. 063805, 2020.

[62] T. Akin, S. Krzyzewski, A. Marino, and E. Abraham *Opt. Commun.*, vol. 339, pp. 209–215, 2015.

[63] R. L. Phillips and L. C. Andrews. *Appl. Opt.*, vol. 22, pp. 643–644, 1983.

[64] G. Vallone, G. Parisi, F. Spinello, E. Mari, F. Tamburini, and P. Villoresi *Phys. Rev. A*, vol. 94, no. 2, p. 023802, 2016.

This volume has been typeset in LaTeXwith the UFPEThesis class (www.cin.ufpe.br/~paguso/ufpethesis).